TÉCNICO LISBOA

Closed Dynamic Soaring Trajectories for Surveillance Missions of Aerial Vehicles

David Emanuel de Castro Ventura Alexandre

Thesis to obtain the Master of Science Degree in

Aerospace Engineering

Supervisors: Prof. Luca Marino
Prof. André Calado Marta

Examination Committee

Chairperson: Prof. Filipe Szolnoky Ramos Pinto Cunha
Supervisor: Prof. André Calado Marta
Member of the Committee: Prof. Aurélio Lima Araújo

December 2019

Closed Dynamic Soaring Trajectories for Surveillance Missions of Aerial Vehicles

David Emanuel de Castro Ventura Alexandre

Thesis to obtain the Master of Science Degree in

Aerospace Engineering

Supervisors: Prof. Luca Marino
Prof. André Calado Marta

Examination Committee

Chairperson: Prof. Filipe Szolnoky Ramos Pinto Cunha
Supervisor: Prof. André Calado Marta
Member of the Committee: Prof. Aurélio Lima Araújo

December 2019

To my mum and dad, thank you for all the love and care.

Acknowledgments

Participating in a masters double-degree program was an exceptionally remarkable experience and constituted a challenge that I am glad I accepted.

I want to start by expressing my gratitude to Instituto Superior Técnico and Università di Roma “La Sapienza” for having made this experience possible by establishing this new exchange program. The present thesis is the first to establish the link between these two institutions together.

The development of this thesis would not have been possible without the constant support and dedication of professors Luca Marino, Giorgio Graziani and Renzo Piva, who welcomed me into their department and helped me through all the steps of the thesis development. I would also like to thank professor André Marta for the readiness with which accepted to co-tutor this endeavour.

I also want to express my gratitude to my friends Diogo Ferreira, João Rodrigues, João Santos, Rafael Duarte, Ricardo Farracho, Rúben Cardoso and Tomás Oliveira who throughout countless dinners and heated discussions over the most varied themes have made all this process easier and enjoyable. To all my other friends and colleagues, thank you for all the good times.

To my family, a very special thank you for all the love and care. To my mum, dad and sister thank you for constant support, care and dedication in every step of the way that led to this moment. It would not have been possible without you.

Finally, I am very grateful for having had by my side a very special person, who was always ready to listen to my concerns, give me thoughtful opinions and to read this document time and time again, thank you Débora for always being there.

Resumo

Dynamic soaring é uma técnica de voo usada pelos albatrozes para cobrir grandes distâncias sem dispêndio de energia, a qual é obtida através do vento presente. Trajetórias fechadas de *dynamic soaring* utilizam variações espaciais da velocidade do vento e possibilitam, em teoria, que o veículo paire indefinidamente sobre uma determinada área. Este tipo de trajetórias, se aplicada a missões de veículos aéreos não tripulados, poderá permitir obter ganhos ao nível da sua autonomia. A principal limitação do dyanamic soaring é a sua dependência das condições de vento existentes, o que implica que as manobras de voo tenham de ser adaptadas em função do perfil de vento presente. A presente tese estuda a viabilidade de trajetórias de *dynamic soaring* fechadas e energeticamente neutras, para uma variedade de cenários. Através do uso de técnicas de otimização de trajetória, foi possível o estudo de como o perfil de vento, as condições iniciais e as limitações do veículo influenciam a força de vento necessária para realizar as manobras e consequentemente a sua viabilidade. Foi possível concluir que existem valores ótimos para as condições iniciais que minimizam a força de vento necessária para realizar as trajetórias. Em adição, foi verificado que as limitações estruturais e aerodinâmicas do veículo também afetam as trajetórias de *dynamic soaring* a altas e baixas velocidades, respetivamente. A tese conclui propondo novas trajetórias energeticamente neutras que, em condições favoráveis de vento, maximizam o tempo de voo e comprimento das mesmas, tornando-as especialmente úteis nas missões de monitorização desempenhadas por veículos aéreos.

Palavras-chave: Otimização de Trajetória, Dinâmica de Voo Não Linear, Aproveitamento Energético, Autonomia, Condições de Viabilidade

Abstract

Dynamic soaring is a flight technique used by albatrosses to cover large distances without the expenditure of energy, which is extracted from the available wind conditions. Closed dynamic soaring trajectories use spatial variations of wind speed to hover, in principle, indefinitely over a prescribed area. Applying the concept of closed dynamic soaring trajectories to aerial vehicles, in particular, UAVs may provide a solution to improve the endurance of these vehicles in certain particular missions. The main limitation of dynamic soaring is its dependence on the wind. The present thesis studies the feasibility of closed, single-loop, energy-neutral trajectories for a broad set of conditions. Through the use of trajectory optimization methods, it was possible to see how the wind profile, initial flight conditions and vehicle constraints influence the required wind strength to perform dynamic soaring and consequently the trajectories' viability. It was possible to conclude from the study that there are optimal values for the initial airspeed and initial height of the vehicle, that minimise the required wind strength to perform the trajectories. In addition, it was seen that the structural and aerodynamic constraints of the vehicle affect dynamic soaring trajectories at high and low airspeeds respectively. The thesis ends by proposing some new trajectories that can be performed in conditions of excess wind to maximize the time spent on the air and the trajectory length while maintaining the concept of single-loop, energy-neutral trajectories, making them especially useful for aerial vehicles surveillance applications.

Keywords: Trajectory Optimization, Non-Linear Flight Dynamics, Energy-Harvesting, Endurance, Feasibility Conditions

Contents

List of Tables

List of Figures

Nomenclature

Greek symbols

β	Linear wind gradient slope.
γ	Flight path angle.
ΔW_r	Real wind speed delta.
η_h	Comparison parameter based on the trajectory height.
η_l	Comparison parameter based on the trajectory length.
ρ	Density.
ϕ	Bank angle.
ψ	Heading angle.
$\boldsymbol{\omega}$	Angular velocity vector.

Roman symbols

A	Maximum wind strength of a step-wind profile.
b	Transition height of a step-wind profile.
C_D	Coefficient of drag.
C_L	Coefficient of lift.
C_{D_0}	Zero lift drag coefficient.
D	Drag.
$\boldsymbol{e}$	Unit Vector.
$\boldsymbol{F_A}$	Aerodynamic forces vector.
$\boldsymbol{F_G}$	Gravitational forces vector.
h	Height.
K	Induced drag coefficient.

k Steepness of a step-wind profile.

L Lift.

N Number of collocation points.

n Load factor.

S Wing area.

$\boldsymbol{T}$ Transformation matrix.

$\boldsymbol{V_A}$ Air velocity vector.

$\boldsymbol{V_G}$ Ground velocity vector.

V_A Airspeed.

V_G Ground speed.

$\boldsymbol{u}$ Control vector.

$\boldsymbol{x}$ State vector.

x, y, z Vehicle position.

Subscripts

0 Initial conditions.

f Final conditions.

max Maximum Value.

min Minimum Value.

ref Reference condition.

x, y, z Cartesian components.

Superscripts

E Earth frame.

E' NED frame.

F Flight path frame.

T Transpose.

W Wind frame.

Glossary

EoM	Equations of Motion.
HALE	High Altitude Long Endurance.
ICLOCS	Imperial College London Optimal Control Software.
IPOPT	Interior Point Optimizer.
LGR	Legendre-Gauss-Radau collocation method.
MALE	Medium Altitude Long Endurance.
MUAV	Mini Unmanned Aerial Vehicle.
NCF	Non-Conservative Forces.
NED	North-East-Down frame.
NLP	Non Linear Programming.
SUAV	Small Unmanned Aerial Vehicle.
TUAV	Tatical Unmanned Aerial Vehicle.
UAV	Unmanned Aerial Vehicle.

Chapter 1

Introduction

1.1 Motivation

1.1.1 UAV Categories and Limitations

Unmanned Aerial Vehicles (UAVs) are autonomous flying vehicles, capable of communicating their primary state information, such as position, velocity and heading, and mission-oriented information, such as captured images, videos, directly to their controller in real-time. The autonomy of these vehicles is what distinguishes them from radio-controlled models and the commonly named drones, that may be able to track pre-determined courses but are not able to make autonomous decisions [1] .

UAVs are commonly used in situations in which using a human on-board pilot may be hazardous or dull. Examples of UAV applications are military reconnaissance, signal relay, search and rescue, cargo transportation, infrastructure inspection and even crop-spraying [1].

The variety of scenarios and applications these vehicles can be used in led to an explosion on the development of mission-oriented UAVs, adapted to serve specific functions. Surveys conducted accounted for more than 600 different UAV models in phase of development or deployment [2]. Despite the large variety of UAVs, there is not a universally accepted classification system, meaning that each regulatory body adopts the categorization they see fit. A typical categorization for UAVs is presented in Table 1.1.

High Altitude Long Endurance (HALE) and Medium Altitude Long Endurance (MALE) UAV categories comprise large vehicles, with long endurance times. An example of a HALE UAV is Boeing's Phantom Eye that is equipped with two combustion engines and is capable of flying for a maximum of 4 days uninterrupted. The main disadvantage of these types of UAVs is the difficulty in deployment due to their size. The Phantom Eye has a gross takeoff weight of 4.5 tons and a span of 46 meters [3]. These vehicles also have a high operational costs since their logistic is comparable to that of a conventional aeroplane.

On the other side of the spectrum, there are the mini (MUAVs) and micro (μUAVs) UAVs, which are small, lightweight and relatively inexpensive when compared with their larger counterparts but suffer from limited endurance times. For instance, Tekever's AR4 only weighs 5 kilograms and has a span of

Category	Weight	Endurance Time	Operating Altitude	Typical Missions	Examples
High Altitude Long Endurance (HALE)	$>$600Kg	$>$12h	Up to 19812m (65000ft)	Surveillance, data gathering, signal relay.	Phantom Eye [3]
Medium Altitude Long Endurance (MALE)	$>$600Kg	$>$12h	Up to 13716m (45000ft)	Surveillance, data gathering, cargo transport.	Hermes-900 [4]
Tactical UAV (TUAV)	150-600Kg	Up to 12h	Up to 5486m (18000ft)	Surveillance, data gathering.	Falco [5]
Small UAV (SUAV)	15-150 Kg	Up to 12h	Up to 1524m (5000ft)	Surveillance, data gathering.	AR3 [6]
Mini UAV (MUAV)	2-15Kg	1-3h	Up to 914m (3000ft)	Surveillance, data gathering.	AR4 [7]
Micro UAV (μUAV)	$<$2Kg	Up to 1h	Up to 61m (200ft)	Surveillance, data gathering.	Black Widow [8]

Table 1.1: Summary of the different categories of UAVs, adapted from [1, 9, 10].

1.8 meters but it is limited to 2 hours of flight [7].

Figure 1.1 presents the relationship between overall UAV weight and the respective endurance time, for the different UAV categories. It is possible to conclude from from it that as the weight (and consequently, the overall size) increases the endurance time also increases, this is in part because larger UAVs use turboprop engines instead of electrical motors for propulsion, meaning that their range does not depend on battery capacity. Furthermore, the lightweight nature of MUAVs and mUAVs limits the number and size of the on-board batteries, limiting even-further the endurance of these vehicles.

The possibility of increasing the operational endurance time of MUAVs would allow them to compete with their larger counterparts while maintaining low operational costs and increased deployment flexibility. Since the use of higher capacity batteries would impair the overall lightness of these vehicles, other approaches to increase the endurance time must be employed.

Different approaches have been proposed to increase the range of MUAV's. These include the harvest of solar energy using photovoltaic panels that charge the batteries during the UAV's flight [11, 12], the use of fuel cells [13], or even battery dumping to increase lightness [14]. Another possibility to boost MUAVs' and μUAVs' range is dynamic soaring.

1.1.2 Dynamic Soaring to improve UAV's Endurance

In general, soaring consists in taking advantage of existing wind conditions to maintain or even gain altitude without spending energy. Soaring differs from gliding since in the latter there is a loss of altitude throughout the flight [15].

Soaring can be divided into static and dynamic. In static soaring, the vehicle harvests energy from

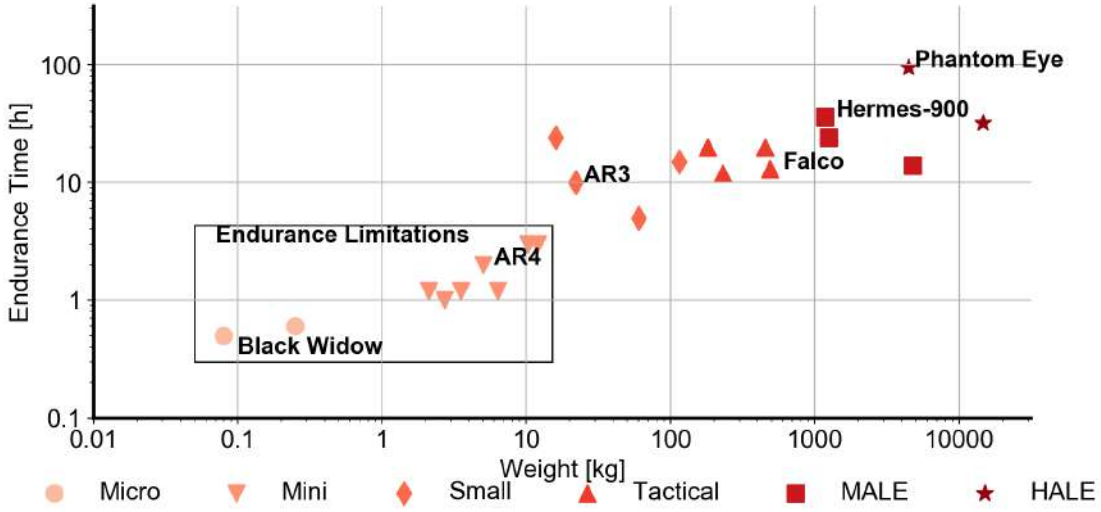

Figure 1.1: Comparison between UAV categories, showing the evolution of the endurance time as a function of weight. Table A.1, in appendix, presents the full list of UAVs considered.

raising air currents that form when specific environment characteristics are met [15]. On the contrary, in dynamic soaring, the vehicle takes advantage of the spatial wind variations, to maintain itself aloft. For dynamic soaring to occur, there must be an increase in wind speed with altitude. In these conditions, the vehicle can perform a dynamic soaring manoeuvre, such as the one of figure 1.2, consisting of a climb into the increasing wind, an upper turn, a descent with the wind and a lower turn to return to the original heading.

By performing dynamic soaring manoeuvres, the vehicle can take advantage of the strong winds at high altitudes to gain energy during the climb, upper turn, and descent phases, while using the comparatively weak winds at lower altitudes, to minimise the losses that occur in the lower turn [16].

There are various types of dynamic soaring manoeuvres. There are; open trajectories, in which for each time the manoeuvre is performed the vehicle advances in a determined direction; and closed manoeuvres where the vehicle flies over a region indefinitely, always returning to the initial point.

Dynamic soaring manoeuvres are, in nature, used by the wandering albatross as a technique to cover vast distances without expenditure of energy. It was observed that the albatross could lock its wings in a fully open position, and travel many kilometres, without flapping its wings, or in other words, with very little expenditure of energy [16]. In aerial vehicles, dynamic soaring has been used to break speed records of RC models with great success [18].

The main drawback of dynamic soaring is the dependence on the environmental conditions around the vehicle. The specificity of the wind conditions required for dynamic soaring limits its applicability since the manoeuvres can only be used in regions where the ideal wind conditions are present.

Although it is not possible to remove the wind dependence from dynamic soaring manoeuvres, it might be possible to reduce the wind requirements for its applicability. By doing so, it would be possible to increase the conditions in which dynamic soaring can be applied.

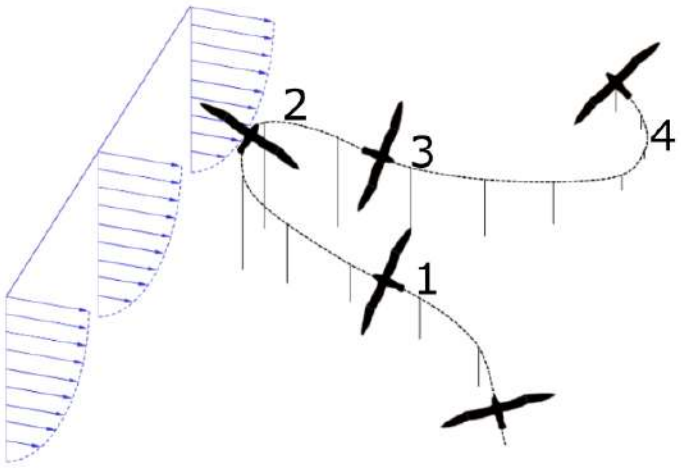

Figure 1.2: Dynamic Soaring's phases of flight : 1 - Climb; 2 - Upper Turn; 3 - Descent; 4 - Lower Turn [17].

Dynamic soaring as a technique for increasing UAV endurance is very promising. To perform dynamic soaring manoeuvres, it is not necessary to extensively modify the vehicle, it is only necessary to follow a pre-defined trajectory that, in the future, may be calculated by the UAVs onboard computers. Besides that, dynamic soaring closed-loop trajectories have an excellent potential for surveillance UAV applications, since the execution of the trajectories would mean that the UAV would be able to patrol a determined area indefinitely, while wind is present.

The promise of dynamic soaring to improve the endurance of UAVs motivates the present research to dive deep in the questions that revolve around this phenomenon.

1.2 Topic Overview

The concept of dynamic soaring was first introduced by Lord Rayleigh in 1883 [19]. Observing the flight of pelicans Rayleigh realized that they could perform large closed circular trajectories, without flapping their wings (without the expenditure of energy). Rayleigh was the first to propose a description for the dynamic soaring mechanism used by the pelican.

After Rayleigh's first description of the phenomenon, many other authors continued the study of the mechanism, based on the observation of the flight of other birds, Idrac [20] and Walkden [21], both presented their proposals based on the flight of the albatross, which was able to soar in the presence of horizontal winds that increased in strength with altitude, unlike many other birds that were only able to take advantage of ascending winds to perform soaring flight (static soaring). The flight of the albatross became the reference for the study of dynamic soaring. Observations found that it was able to travel for days and cover large distances with minimum loss of energy.

The study and quantification of the aerodynamic characteristics and trajectories of soaring birds were first made by Pennycuick [22, 23] and Parrot and Tucker [24]. While one of the first full mathematical analysis of the dynamic soaring phenomenon was performed by Cone [25]. Later appeared the first

computational simulations, performed by Wood [26] and Wilson [27]. In these simulations, the equations of motion were programmed and then different possible trajectories were performed and, looking for the best trajectories and conditions for dynamic soaring.

With the appearance of new non-linear optimization methods, new results were obtained. Sachs [16, 28] presented a full deduction of the equations of motion in the Earth frame and calculated optimal dynamic soaring trajectories. Sachs also introduced the concept of minimum wind strength required for dynamic soaring trajectories,that for a given UAV model and initial conditions indicated the minimum value of the wind strength necessary to perform energy-neutral dynamic soaring manoeuvres. The minimum wind strength parameter is, currently, a well-established parameter, used to determine the feasibility of dynamic soaring manoeuvres.

Simultaneously, Zhao [29, 30] also performed a series of optimizations, using normalized equations of motion in the flight path frame. In addition, he also considered scenarios in which thrust is available, since it reflected what should be expected for a UAV application.

Lissaman [31], in addition to providing his explanation of how the dynamic soaring mechanism works, also considered the effect of different wind profiles, such as the linear and logarithmic wind profiles, in the overall performance of dynamic soaring.

Using tracking technology, Sachs [32, 33] presented a series of comparisons between the optimized results and measured results of the flight of the albatross, concluding that the obtained optimizations follow what happens in nature.

With the rapid growth in the development of commercial available MUAVs, a renewed interest in dynamic soaring appeared. Following the work developed by Sachs and Zhao, different papers explore different scenarios for UAV operation using dynamic soaring. Bower [34] presented results regarding the maximization of the the net speed for the trajectory, the control problem for a UAV and even proposed a UAV design that optimized the performance for dynamic soaring, the Mariner UAV. Bonin [35] performed UAV performance comparison studies also based on results from optimization methods. Gao [15] in his studies considered, in addition to dynamic soaring, static soaring comparing both phenomena and their applicability.

Very recently, in 2019 new papers have appeared, Sachs [18, 36, 37] presented new optimizations where he focuses on maximizing the net travel speed for different wind strengths, presented the case for how dynamic soaring is used for achieving record-breaking speeds for UAVs, and provided an in-depth description of the energy-harvesting mechanism of dynamic soaring. Kai [38] took a new approach to the modeling and simulation of dynamic soaring, estimating analytically the expressions for different variables associated with dynamic soaring, such as the minimum wind strength required.

Also in 2019, new proposals on how to maximize the extraction of energy from dynamic soaring, have also been made. Mir [39] studied how wing morphing capabilities can be used to maximize extraction, while Bonnin [40] presented studies on how electrical generators can harvest energy during the dynamic soaring manoeuvre and store it in on board batteries. As demonstrated, the study of dynamic soaring is currently a very active field with new insights appearing almost every year.

1.3 Objectives and Deliverables

It is in the context of the limitations of the dynamic soaring mechanism that the present research will be conducted. The main goals of this thesis are to understand how the applicability of dynamic soaring manoeuvres is affected by different factors and propose trajectories optimised for surveillance missions.

To achieve the proposed goals, research will be conducted using optimisation techniques. By converting the dynamic soaring problem into an optimal trajectory problem, it is possible to find trajectories for the UAV that minimise the energy spent.

The development of a robust computational tool allows the obtention of dynamic soaring trajectories for a variety of wind conditions and UAV models and initial conditions. The study of different trajectories is, first of all, useful for the study of the energy-harvesting mechanism in which dynamic soaring manoeuvres are based. In addition, results for different wind conditions will allow the study of the impact of the wind profile on dynamic soaring, and how to minimise the restriction it imposes. By studying the effect of initial conditions and vehicle constraints on dynamic soaring, it will allow the proposal of solutions to increase the performance of dynamic soaring manoeuvres.

To achieve the main goal proposed and study all the different aspects of dynamic soaring, the research has five main objectives:

- Establish a mathematical model for UAV motion;
- Develop a robust optimal trajectory formulation for the study of the different characteristics of dynamic soaring, and establish the solving techniques required for its resolution;
- Understand the energy-harvesting mechanism of dynamic soaring and how the wind is present in the mechanism;
- Study how different wind profiles, initial conditions and vehicle constraints influence the dynamic soaring mechanism;
- Propose possible trajectories specially designed for surveillance missions, that take into account the results of the previous study.

Understanding how the wind profile changes the behaviour of dynamic soaring trajectories may allow for the future development of dynamic soaring controllers that are better suited to deal with changing winds and with non-ideal wind conditions. Besides that, knowing how the initial conditions affect energy-extraction may allow for the development of trajectories that maximise the energy that can be harvested from the wind.

If the objectives proposed are achieved, the new results will provide:

- An analysis of the numerical methods used to study dynamic soaring and an optimization tool that may be used in further dynamic soaring studies;
- Insights on how the wind, initial conditions and vehicle constraints influence dynamic soaring trajectories.

- New solutions to maximise the applicability of dynamic soaring for extending the range of UAVs.

1.4 Thesis Outline

The outline of the present document was selected in such a way it reflects the various phases of the performed work.

Chapter 2 presents the full deduction of the mathematical model necessary for the study of dynamic soaring. It starts with the initial assumptions for the development of the UAV model and goes on describing the various steps performed to arrive at the two most commonly used models. The chapter ends with a discussion regarding the advantages and disadvantages of each model.

Chapter 3 is concerned with the definition of the optimal trajectory problem and the description of how an optimization problem can be used to study dynamic soaring. It also gives insights on how the computational methods can solve this kind of problems, presenting the most relevant points to take into account when analysing the results. The verification of the computational method ends this chapter.

Chapter 4 details how the energy-harvesting mechanism of dynamic soaring works, through the presentation of initial results obtained with the computational tools previously described. The chapter describes a close, energy-neutral trajectory, detailing how the dynamic soaring phenomenon allows for net-zero expenditure of energy.

Chapter 5 presents the first set of results obtained. The chapter starts by presenting and discussing the set of metric necessary for the comparison of the trajectories obtained. Afterwards, the influence of different wind profiles on the dynamic soaring trajectories is studied. The chapter also studies the influence of the UAV initial conditions on the feasibility of the trajectories. It ends with considerations related to how structural and aerodynamic limitations of the vehicles affect dynamic soaring.

Chapter 6 is concerned with finding possible trajectories for surveillance missions that take advantage of the existing wind conditions to maximize the time and length of a closed dynamic soaring trajectory. The chapter ends with an overview of other possible applications of the dynamic soaring energy-mechanism.

In the end, chapter 7 presents a summary of the conclusions drawn throughout the developed work and proposes new areas of research that may be conducted in the future.

Chapter 2

Equations of Motion for a UAV

This chapter presents the groundwork for the study of dynamic soaring. It starts by describing the preliminary assumptions necessary to establish a solid model of the UAV flight dynamics. Afterwards, the forces acting on the UAV are defined, as well as the wind models that will be utilized. Then, the equations of motion are defined in two different frames, and the advantages and disadvantages of each set are discussed. The chapter ends with the derivation of expressions for the power contributions of the lift and drag.

2.1 UAV Model

2.1.1 Preliminary Assumptions

The equations of motion (EoM) for a UAV will be developed based on two preliminary assumptions. Firstly, the Earth is considered as flat and non-rotating, since the scale of distances being considered is small enough when compared to the scale of the Earth. Secondly, the UAV is characterized by its centre of mass, which means that all inertia terms related with the UAV's rotation should be neglected. These assumptions are equal to those used by previous authors [41].

To obtain the full picture of a UAV's motion it is necessary to consider four different frames: the Earth frame, the North-East-Down (NED) frame, the flight path frame and the wind frame. Figure 2.1 presents the relationship between the various frames.

The Earth frame ($O(\boldsymbol{e}_x^E, \boldsymbol{e}_y^E, \boldsymbol{e}_z^E)$) has its origin in the Earth with its x-axis pointing north, y-axis pointing east and z-axis pointing down. It is important to point out that this frame is fixed and inertial but not right-handed.

The North-East-Down (NED) frame ($U(\boldsymbol{e}_x^{E'}, \boldsymbol{e}_y^{E'}, \boldsymbol{e}_z^{E'})$) is parallel to the Earth frame but has its origin in the UAV center of mass.

The flight path frame ($U(\boldsymbol{e}_x^F, \boldsymbol{e}_y^F, \boldsymbol{e}_z^F)$) also has its origin in the centre of mass of the UAV, but its x-axis points in the direction of the airspeed vector, and it is obtained by rotating of the NED frame according with the heading (ψ) and flight path angles (γ).

Finally, the wind frame ($U(\boldsymbol{e}_x^W, \boldsymbol{e}_y^W, \boldsymbol{e}_z^W)$) also has its origin in the UAV's centre of mass and its x-axis pointing in the direction of the airspeed vector, but in this case there is also a rotation according to the bank angle (ϕ), resulting in its z-axis being in the plane of symmetry of the vehicle.

It is possible to transform a vector in one of the frames to another through successive rotations about the three axes. The angles of rotation are the bank angle, ϕ, the flight path angle , γ, and the heading angle, ψ, which correspond respectively to the rotations around the x-axis, y-axis and z-axis.

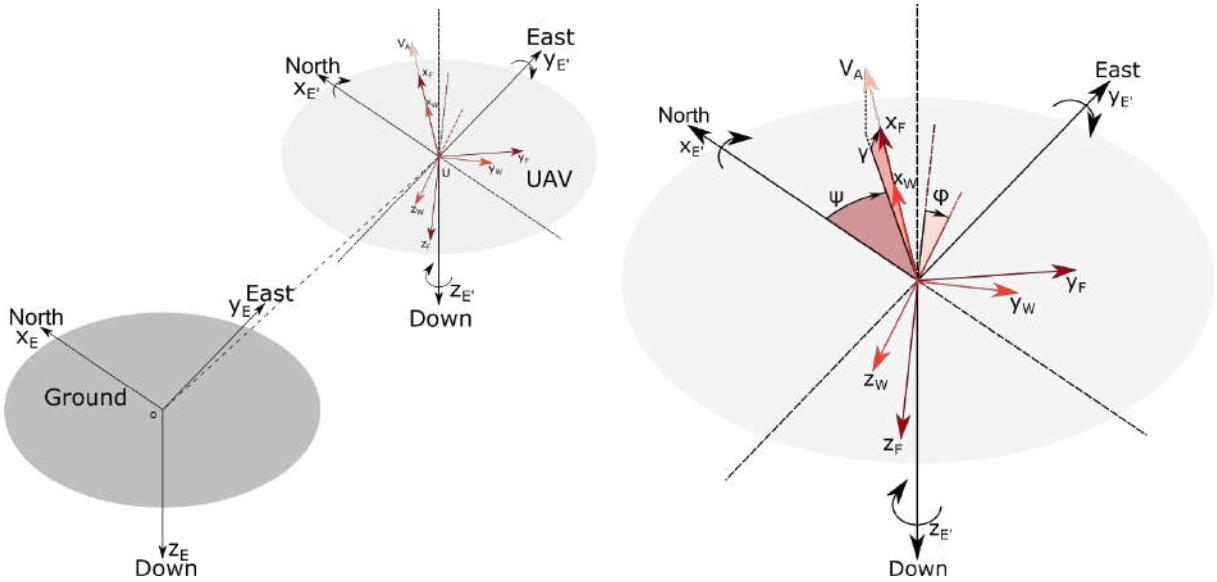

(a) Relation between the Earth and NED frames.

(b) Close up on the NED, Flight Path and Wind Frames.

Figure 2.1: Relationship between the Earth, NED, Flight Path(in red) and Wind (in orange) frames. Adapted from [35].

The transformation matrix from the NED frame to the wind frame is

$$\boldsymbol{T_{WE'}} = \boldsymbol{T_x}(\phi)\boldsymbol{T_y}(\gamma)\boldsymbol{T_z}(\psi), \tag{2.1}$$

where

$$\boldsymbol{T_x}(\phi) = \begin{bmatrix} 1 & 0 & 0 \\ 0 & \cos\phi & \sin\phi \\ 0 & -\sin\phi & \cos\phi \end{bmatrix}, \tag{2.2}$$

$$\boldsymbol{T_y}(\gamma) = \begin{bmatrix} \cos\gamma & 0 & -\sin\gamma \\ 0 & 1 & 0 \\ \sin\gamma & 0 & \cos\gamma \end{bmatrix} \tag{2.3}$$

and

$$\boldsymbol{T_z}(\psi) = \begin{bmatrix} \cos\psi & \sin\psi & 0 \\ -\sin\psi & \cos\psi & 0 \\ 0 & 0 & 1 \end{bmatrix}, \tag{2.4}$$

which results in

$$\boldsymbol{T_{WE'}} = \begin{bmatrix} \cos\gamma\cos\psi & \cos\gamma\sin\psi & -\sin\gamma \\ (\sin\phi\sin\gamma\cos\psi - \cos\phi\sin\psi) & (\sin\phi\sin\gamma\sin\psi + \cos\phi\cos\psi) & \sin\phi\cos\gamma \\ \cos\phi\sin\gamma\cos\psi + \sin\phi\sin\psi) & (\cos\phi\sin\gamma\sin\psi - \sin\phi\cos\psi) & \cos\phi\cos\gamma \end{bmatrix} \tag{2.5}$$

Since the Earth frame and NED frame are parallel to each other, the matrices of transformation to and from the Earth frame are equal to those of the NED frame,

$$\boldsymbol{T_{WE'}} = \boldsymbol{T_{WE}}. \tag{2.6}$$

It is also possible to obtain the transformation matrices between any of the remaining frames. Between the Earth and flight path frames, the transformation matrix is given by

$$\boldsymbol{T_{FE}} = \boldsymbol{T_y}(\gamma)\boldsymbol{T_z}(\psi), \tag{2.7}$$

and between the flight path and wind frames by

$$\boldsymbol{T_{WF}} = \boldsymbol{T_x}(\phi). \tag{2.8}$$

In addition, also note that for any two generic frames A and B,

$$\boldsymbol{T_{AB}} = \boldsymbol{T_{BA}}^T. \tag{2.9}$$

2.1.2 Forces Acting on the UAV

For the present UAV model, there are two types of forces that should be considered: the gravitational forces and the aerodynamic forces. Thrust forces will not be considered since the desired trajectories should be performed without the use of a propulsion system. Figure 2.2 presents schematically the forces acting on the UAV.

The direction and intensity of gravitational force can be easily defined in the Earth frame,

$$\boldsymbol{F_G}^E = mg\boldsymbol{e}_z^E, \tag{2.10}$$

where m is the UAV mass and g is the modulus of the gravitational acceleration.

Defining the aerodynamic forces in the wind frame is the most straightforward approach since, by definition, the lift is orthogonal to the airspeed vector pointing in the opposite direction of the z-axis, while the drag is opposed to the airspeed vector. Also, since the UAV will be considered by its centre of mass, there are not side forces acting in the UAV. It is then possible to write

$$\boldsymbol{F_A}^W = -D\boldsymbol{e}_x^W - L\boldsymbol{e}_z^W, \tag{2.11}$$

with the intensity of the lift and drag forces, neglecting compressibility effects, calculated based on

$$L = \frac{1}{2}\rho S V_A^2 C_L, \tag{2.12}$$

$$D = \frac{1}{2}\rho S V_A^2 C_D \tag{2.13}$$

and

$$C_D = C_{D_0} + K C_L^2, \tag{2.14}$$

where V_A is the vehicle's airspeed, ρ is the air density, S is the wing area, C_L is the lift coefficient, C_D is the drag coefficient, C_{D_0} is the viscous zero lift drag coefficient and K the induced drag coefficient.

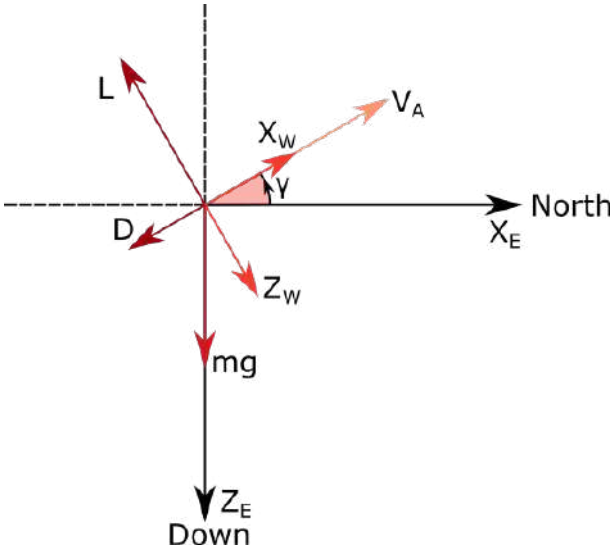

Figure 2.2: Longitudinal forces acting on the UAV. (See [35]).

2.1.3 Environment and UAV Characteristics

There are some vehicle characteristics that can be established *a priori*: the mass and the aerodynamic characteristics. Table 2.1 summarizes these characteristics for two different aerial vehicles.

UAV Model	Mass (m)	Wing Area (S)	Zero Lift Drag Coefficient(C_{D_0})	Induced Drag Coefficient(K)
Albatross [16]	$8.5kg$	$0.65m^2$	0.033	0.019
Mariner [34]	$1.99kg$	$0.485m^2$	0.0173	0.0629

Table 2.1: List of UAV models and respective characteristics.

The albatross model presented was introduced by Sachs [16], and for the purposes of the present study, it will be the one considered. The model of UAV Mariner is here shown for comparison, it was developed by Bower [34] as a UAV optimized for dynamic soaring.

Regarding the environment variables, the gravitational acceleration, g, will be considered as $9.81ms^2$ and the air density, ρ as $1.225kg/m^3$, corresponding to standard sea-level conditions.

2.2 Wind Models

Different wind models can be applied in order to study the dynamic soaring phenomenon. The most common models are the linear wind model, the logarithmic wind model and the step wind model. Each model has its advantages and disadvantages which will be discussed in the following paragraphs.

Independently of the wind model used, it is considered that, without loss of generality, the wind blows to the North and that it remains constant in time, as expressed by

$$W_y^E = W_z^E = 0, \tag{2.15a}$$

$$\frac{dW_y^E}{dt} = \frac{dW_z^E}{dt} = \frac{d\boldsymbol{W}^E}{dx} = \frac{d\boldsymbol{W}^E}{dy} = 0, \tag{2.15b}$$

and

$$\frac{dW_x^E}{dt} = \frac{dW_x^E}{dz}\dot{z}, \tag{2.15c}$$

where $\boldsymbol{W}$ is the wind velocity vector, the superscript E refers to the Earth reference frame and the subscripts x, y, z to the Cartesian component of the wind vector.

2.2.1 Linear Wind Model

The linear model is the simplest wind model that can be applied [30]. In this model the wind velocity is given by

$$\boldsymbol{W}^E = \beta h \boldsymbol{e}_x^E, \tag{2.16}$$

where h is the height of the UAV, being equivalent to the symmetric of the z coordinate of the Earth frame ($h = -z^E$), and β is the wind gradient slope. Figure 2.3(a) presents an example of a linear wind profile.

The main advantage of this wind model is its simplicity which allows for an easy calculation of its gradient, and composes an important aspect from the computational point of view. However, its greatest disadvantage is the fact that linear wind profiles are not common in nature.

2.2.2 Logarithmic Wind Model

The logarithmic wind model is the most widely used wind model for dynamic soaring studies[16, 35, 42]. In this model, the wind profile is given by

$$\boldsymbol{W}^E = W_{ref}\frac{ln(h/h_0)}{ln(h_{ref}/h_0)}\boldsymbol{e}_x^E, \tag{2.17}$$

where h_{ref} its a reference altitude, h_0 is the wind profile starting altitude and W_{ref} is the wind speed at the reference altitude. Figure 2.3(b) presents an example of a logarithmic wind profile.

The main advantage of this type of wind profile is that it represents, with a considerable degree of accuracy, the wind conditions that are expected at low altitudes over the sea, where boundary layer

conditions are present [16]. Its primary disadvantage resides in the fact that it is difficult to manipulate the shape of the logarithmic profile, making the study of the influence of the wind on dynamic soaring harder.

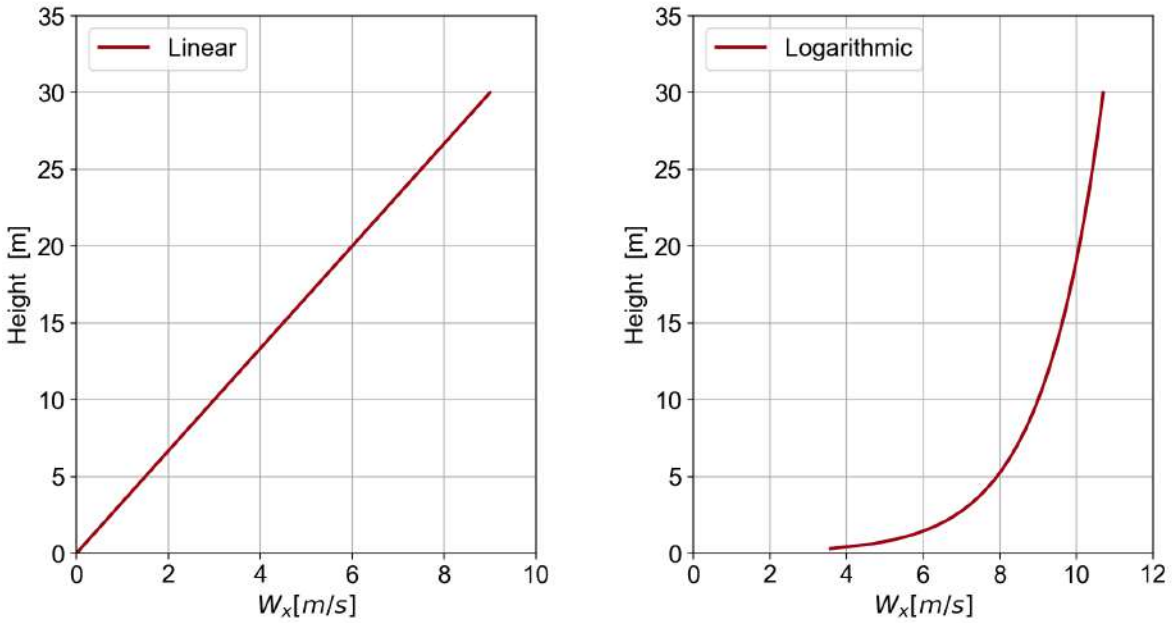

(a) Linear wind profile with $\beta = 0.3$.

(b) Logarithmic wind profile with, $W_{ref} = 10$, $h_0 = 0.03$ and $h_{ref} = 10$.

Figure 2.3: Linear and logarithmic wind profiles.

2.2.3 Step Wind Model

The step wind profile can be described mathematically with two different approaches. The first approach uses a Heaviside function to control the wind profile [34]. The second approach is to use a hyperbolic tangent function to describe the wind profile. Using the latter approach, the wind can be defined as

$$\boldsymbol{W}^E = \frac{A}{2}(\tanh(k(h-b))+1)\boldsymbol{e}_x^E, \tag{2.18}$$

where A is the maximum wind speed, k controls the steepness of the gradient and b is the transition height, at which half of the step is reached. Figure 2.4 presents different step wind profiles obtained by varying the b and k parameters.

The hyperbolic function approach will be the one used since it allows for the control of the gradient with which the wind speed increases and, being a continuous function, holds an added advantage for the implementation of the computational method.

Step wind profiles occur in nature only in particular conditions such as in ridges. The great advantage of this wind model is that it allows for a clear understanding of how the wind impacts the motion of the UAV since in the same flight the vehicle will have phases where it is subjected to wind and others where

it is not.

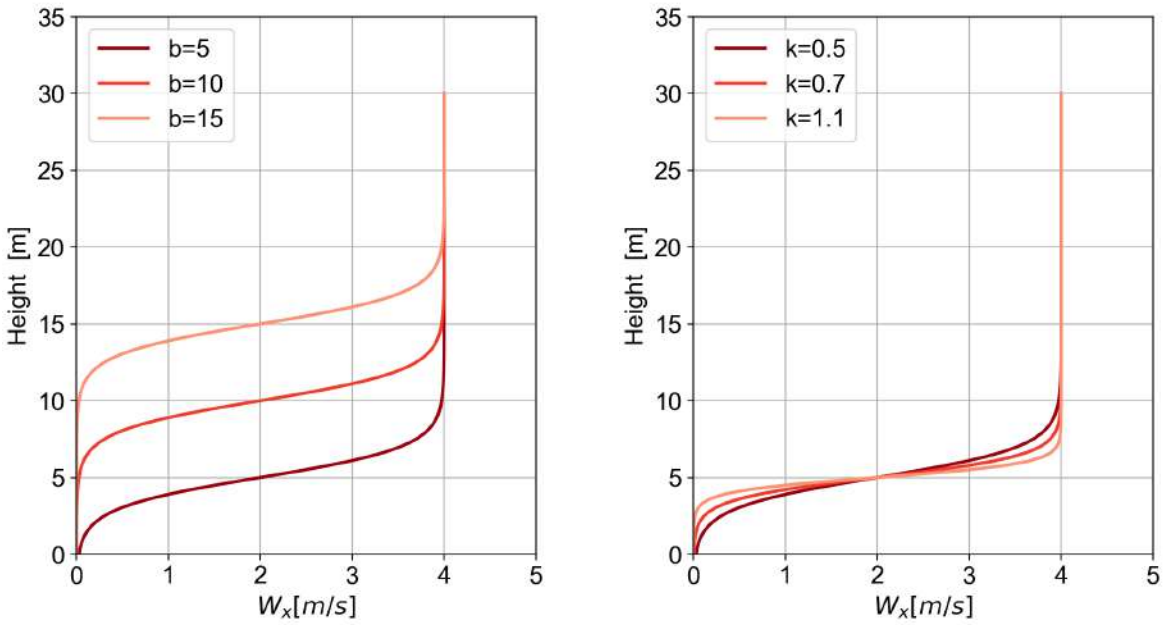

(a) Step wind profiles with A=4, b=10 and changing k.

(b) Step wind profiles with A=4, k=0.5 and changing b.

Figure 2.4: Effect of changing parameters b and k in the final shape of the step wind profile.

2.3 Equations of Motion in the Earth Frame

The starting point for the development of the set of equations of motion (EoM) of the vehicle is Newton's second law of motion written in the Earth Frame [16, 35],

$$m\boldsymbol{a}^E = \sum \boldsymbol{F}^E, \tag{2.19}$$

where m is the vehicle's mass and $\boldsymbol{a}^E$ is the acceleration vector defined in the earth frame. The sum of all external forces applied to the UAV is

$$\sum \boldsymbol{F}^E = \boldsymbol{F_A}^E + \boldsymbol{F_G}^E = \boldsymbol{T_{EW}}\boldsymbol{F_A}^W + \boldsymbol{F_G}^E, \tag{2.20}$$

which in turn is equal to

$$\sum \boldsymbol{F}^E = \begin{bmatrix} -D\cos\gamma\cos\psi - L(\cos\phi\sin\gamma\cos\psi + \sin\phi\sin\psi) \\ -D\cos\gamma\sin\psi - L(\cos\phi\sin\gamma\sin\psi - \sin\phi\cos\psi) \\ D\sin\gamma - L\cos\phi\cos\gamma + mg \end{bmatrix}, \tag{2.21}$$

according to equations (2.5), (2.6), (2.10) and (2.11). Applying this result, the final set of equations is obtained,

$$\begin{cases} m\ddot{x} = -D\cos\gamma\cos\psi - L(\cos\phi\sin\gamma\cos\psi + \sin\phi\sin\psi), \\ m\ddot{y} = -D\cos\gamma\sin\psi - L(\cos\phi\sin\gamma\sin\psi - \sin\phi\cos\psi), \\ m\ddot{z} = D\sin\gamma - L\cos\phi\cos\gamma + mg. \end{cases} \tag{2.22a}$$

From the double integration of this set of equations, it is possible to calculate the position of the UAV at each instant. It is also possible to compute the air and ground speeds, respectively, as

$$V_A = \sqrt{((\dot{x} - W_x)^2 + (\dot{y})^2 + (\dot{z})^2)} \tag{2.23}$$

and

$$V_G = \sqrt{(\dot{x}^2 + \dot{y}^2 + \dot{z}^2)}. \tag{2.24}$$

The fight path and heading angles can be computed using, the respectively,

$$\gamma = \arctan\Big(-\frac{\dot{z}}{\sqrt{((\dot{x} - W_x)^2 + \dot{y}}}\Big) \tag{2.25}$$

and

$$\psi = \arctan\Big(\frac{\dot{y}}{\dot{x} - W_x}\Big). \tag{2.26}$$

The fact that the z-axis is pointing down results in the altitude of the vehicle to be a negative value. Thus, to make the set of equations more intuitive, the height will be represented by h, which is symmetric to the z coordinate, as previously mentioned.

The main advantage of this set of equations, as used by Sachs [16, 28], resides in the relative simplicity of the set differential equations and the fact that the wind profile does not appear directly in the system dynamics. The main disadvantage of this representation is the fact that it is not very intuitive since the standard flight variables (airspeed V_A, heading angle ψ and flight path angle γ) are calculated only after solving the UAV's EoM [34].

2.4 Equations of Motion in the Flight Path Frame

Another way of obtaining the EoM of the UAV is to use the flight path frame instead of the earth frame. This approach is used by Zhao and other authors [29, 41]. To write the new set of EoM, the starting point is, once again, equation (2.19). This equation can be re-written in the flight path frame,

$$m(\dot{\boldsymbol{V_A}}^F + \boldsymbol{\omega}^F \times \boldsymbol{V_A}^F) + m\dot{\boldsymbol{W}}^F = \sum \boldsymbol{F}^F, \tag{2.27}$$

where $\boldsymbol{\omega_F}$ is vector of the angular velocities of the flight path frame with respect to the earth frame, and $\dot{\boldsymbol{W}}_{\boldsymbol{F}}$ is the time derivative of the wind velocity. The full deduction of equation (2.27) can be found in

appendix B.1.

The sum of the forces applied to the UAV in the flight path frame is

$$\sum \boldsymbol{F}^F = \boldsymbol{F_A}^F + \boldsymbol{F_G}^F = \boldsymbol{T_{FW}}\boldsymbol{F_A}^W + \boldsymbol{T_{FE}}\boldsymbol{F_G}^E, \tag{2.28}$$

resulting in

$$\sum \boldsymbol{F}^F = \begin{bmatrix} -D - mg\sin\gamma \\ L\sin\phi \\ -L\cos\phi + mg\cos\gamma \end{bmatrix}, \tag{2.29}$$

where equations (2.7), (2.8), (2.10) and (2.11) have been used.

The angular velocity of the flight path frame can be calculated from the derivative of the transformation matrix from the flight path frame to the earth frame (see appendix B.1), resulting in

$$\boldsymbol{\omega}^F = \begin{bmatrix} -\dot{\psi}\sin\gamma & \dot{\gamma} & \dot{\psi}\cos\gamma \end{bmatrix}. \tag{2.30}$$

Finally, the time derivative of the wind velocity in the flight path frame can also be readily obtained, yielding

$$\dot{\boldsymbol{W}}^F = \boldsymbol{T_{FE}}\dot{\boldsymbol{W}}^E = \begin{bmatrix} \cos\gamma\cos\psi\dot{W}_x^E \\ -\sin\psi\dot{W}_x^E \\ \sin\gamma\cos\psi\dot{W}_x^E \end{bmatrix}. \tag{2.31}$$

By replacing the previous results in equation (2.27), the following set of equations is obtained,

$$m\dot{V_A} = -D - mg\sin\gamma - m\cos\gamma\cos\psi\dot{W}_x^E, \tag{2.32a}$$

$$mV_A\cos\gamma\dot{\psi} = L\sin\phi + m\sin\psi\dot{W}_x^E, \tag{2.32b}$$

$$-mV_A\dot{\gamma} = -L\cos\phi + mg\cos\gamma - m\sin\gamma\cos\psi\dot{W}_x^E, \tag{2.32c}$$

$$\dot{x} = V_A\cos\gamma\cos\psi + W_x^E, \tag{2.32d}$$

$$\dot{y} = V_A\cos\gamma\sin\psi, \tag{2.32e}$$

$$\dot{z} = -V_A\sin\gamma. \tag{2.32f}$$

The expressions for the position of the UAV (eqs. (2.32d), (2.32e) and (2.32f)) are a direct consequence of the relationship between the air and ground relative velocity vectors,

$$\boldsymbol{V_G}^E = \boldsymbol{V_A}^E + \boldsymbol{W}^E = \boldsymbol{T_{EF}}\boldsymbol{V_A}^F + \boldsymbol{W}^E. \tag{2.33}$$

The representation of the UAV's EoM in the flight frame allows for a clearer understanding of how the main flight variables (airspeed V_A, heading angle ψ and flight path angle γ) are affected. The main drawback is the increased complexity of the system of differential equations and the need for inclusion of the time derivatives of the wind velocity vector [34].

Both sets of equations yield equivalent results. Due to its intuitiveness, the EoM represented in the flight path frame will be used for the numerical method. The Earth frame will be used mainly for the energy considerations since using a fixed, inertial frame yields more intuitive results.

2.5 Energy Considerations

The study of the motion of the UAV needs to be accompanied by a study of the energy exchanges that occur during its motion. To perform this, it is easier to use an inertial frame of reference, such as the Earth frame.

The rate of change of mechanical energy through the UAV motion is a quantity of great interest in the analysis of the energy harvesting mechanism of dynamic soaring. There are two approaches to the calculation of this quantity, through the direct differentiation of the mechanical energy or by the power of the non-conservative forces. Both approaches are shown in this section.

For the first approach, it is known that, by definition, mechanical energy is given by

$$E_m = E_p + E_k \Leftrightarrow E_m = mgh + \frac{1}{2}mV_G^2, \tag{2.34}$$

which means that by direct differentiation,

$$\frac{dE_m}{dt} = \frac{dE_p}{dt} + \frac{dE_k}{dt} = mg\dot{h} + m\dot{x}\ddot{x} + m\dot{y}\ddot{y} + m\dot{z}\ddot{z}. \tag{2.35}$$

The second approach uses the fact that, by definition, the rate of change of mechanical energy is equal to the power of non-conservative forces (NCF), such that it is possible to write

$$\frac{dE_m}{dt} = \sum(\boldsymbol{F_{NCF}}^E \cdot \boldsymbol{V_G}^E). \tag{2.36}$$

Since the only non-conservative forces present in this model are the lift and drag of the UAV, it is possible to divide the rate of change of mechanical energy into a contribution due to the lift, and one due to the drag. Here only the final result is presented, being the full deduction included in appendix B.2,

$$\frac{dE_m}{dt} = -LW_x^E(\cos\phi\sin\gamma\cos\psi + \sin\phi\sin\psi) - DV_A - DW_x^E\cos\gamma\cos\psi. \tag{2.37}$$

Looking at equation (2.37), it is possible to verify that the contribution of the lift to the variation of mechanical energy depends directly on the wind. Thus, in no wind condition there can only be energy loss, since there is only the negative contribution of the drag.

It would also be possible to conduct the same analysis utilizing the flight path frame and by defining the kinetic energy with the airspeed. Sachs [37] presents the full deduction of both methods and proves that they yield identical results. The difference lays in how energy gains are interpreted. Utilizing the Earth frame, as presented in this section, the energy gains result from a component of the lift force, while for the case when the flight path frame is utilized, the energy-gains are included in a fictitious force

term that appears when computing the total energy of the system.

2.6 Overview of the UAV Model

In short, for the analysis of the dynamic soaring phenomenon, the equations of motion in flight path frame will be used for the modelling the flight of the vehicle and the earth frame will be used for the analysis of the contributions of the lift and drag for the energy variation.

The development of the equations presented in this chapter represents the groundwork for the definition of the trajectory optimization problem that will be presented in the next chapter.

Chapter 3

Trajectory Optimization

Trajectory optimization is a set of techniques that try to find the best trajectory given an objective function and a set of constraints. These techniques are very useful for the study of dynamic soaring. This chapter starts by presenting an overview of the available optimization methods, followed by a complete description of the trajectory optimization problem for the case of dynamic soaring. Afterwards, the solving process of the optimization problem is presented. In the end, the verification of the numerical method to use in the remainder of the thesis is performed.

3.1 Overview of Optimization Techniques

3.1.1 Optimization Problems

A generic optimization problem can be stated in the form

$$\begin{aligned} \text{minimise} \quad & f(\boldsymbol{z}) \\ \text{by varying} \quad & \boldsymbol{z} \in \mathbb{R}^N, \\ \text{subject to} \quad & h_p(\boldsymbol{z}) = 0, p = 1, 2, ..., N_h, \\ & g_m(\boldsymbol{z}) \geq 0, m = 1, 2, ..., N_g, \end{aligned} \tag{3.1}$$

where f is the objective function to minimise, $\boldsymbol{z}$ are the design variables of the system, h and g are the equality and inequality constraints of the system respectively, that may be non-linear functions of the design variables [43].

Optimization problems can be constrained or unconstrained, single-variable or multi-variable and linear or non-linear. So depending on their nature, different solving methods can be used. Optimization techniques are, in general, divided into two main groups, deterministic and stochastic.

Deterministic methods have well-established rules, consisting of algorithms that are used to find the optimal solution to the problem. A simple example of a deterministic optimization method is the gradient

descent algorithm, which follows the direction of decreasing gradient to search the optimal solution, no matter the characteristics of the problem [44].

In contrast, stochastic methods have a degree of randomness associated with them; each time, the optimization method is run the path taken by the algorithm to reach the optimal solution varies. Genetic algorithms are a perfect example, each time the optimization procedure is used the genetic characteristics of the population vary, meaning that the optimization path taken to reach the optimal solution is not constant [45].

3.1.2 Deterministic Optimization Methods

There are different deterministic optimization methods designed with the intent of solving optimization problems of different natures. The first distinction that can be made between deterministic algorithms is if they are gradient-based or gradient-free.

Gradient-based deterministic optimization procedures utilize the information of the first and sometimes second-derivatives of the optimization problem to find the search direction that will be used to find the solutions. This type of methods are efficient in finding local optimum solutions for large dimensionality, nonlinearly constrained, convex search space problems [43].

Depending on the characteristics of the problem, gradient-based methods can be further divided into unconstrained and constrained optimization. Unconstrained optimization methods are used in cases without constraints on the problem, meaning that the design variables can be changed freely to minimise the objective function. An example of gradient-based, unconstrained optimization methods are the Newton methods. In contrast, constrained optimization methods are designed to solve problems with equality and inequality constraints. A typical set of constrained optimization methods are the penalty and barrier methods.

There are situations in which it is not convenient, or possible, to use the information of the derivatives of the problem, which might happen because the problem is discrete, has discontinuities or non-differentiable functions. For these cases, there are the gradient-free methods, which do not require the information of the derivatives. Examples of gradient-free methods are the simplex and Hooke-Jeeves algorithms [43].

Unconstrained Optimization - Newton Methods

Unconstrained problems are designed, as their name suggests, to solve problems where the design variables can vary freely. Unconstrained problems are usually stated in the form

$$\begin{aligned} \text{minimise} \quad & f(\boldsymbol{z}) \\ \text{by varying} \quad & \boldsymbol{z} \in \mathbb{R}^N. \end{aligned} \tag{3.2}$$

The main interest on solving unconstrained problems arises from the fact that constrained problems can be converted into unconstrained problems, as it will be seen. So by understanding how to solve a uncon-

strained optimization problem it is also possible to understand how to solve a constrained optimization problem.

In general, unconstrained optimization algorithms can be summarized in the as follows: the algorithm starts with an initialization step, at the start of the algorithm an initial guess must be provided so it can be used as a starting point. Afterwards, the algorithm enters a loop, at the begin of each iteration, there is a convergence test. On the one hand, if the convergence conditions are verified, it means the solution was obtained, and the optimization procedure ends. On the other hand, if the conditions are not met, then it is necessary to keep searching, so a new search direction (p_k) and step length (α_k) are computed, ensuring that the condition $f(z_k + p_k\alpha_k) < f(z_k)$ is respected. The search direction and step length are, finally, used to determine the new value of the design variables, $z_{k+1} = z_k + p_k\alpha_k$. At the end of this step, the loop restarts.

Note that this set of methods will only be able to find the local minimum nearest to the starting point in non-convex problems with multiple local minima, meaning that global optimal solutions cannot be insured.

The main difference between unconstrained optimization methods is how the search direction and step length are computed. For instance, the Newton method utilizes information of the gradient and Hessian of the problem. This method approximates the objective function of the problem by second-order Taylor series expansion,

$$f(z_k + d_k) \approx f_k + g_k^T d_k + \frac{1}{2} d_k^T H_k d_k, \tag{3.3}$$

where d_k is the step to the minimum, g_k and H_k are, respectively, the gradient and Hessian of the objective function. If this expression is differentiated in respect to d_k and its derivative is set to zero, it is possible to obtain an expression for the step that minimises the approximated objective function,

$$H_k d_k = -g_k. \tag{3.4}$$

This method provides a search direction p_k equal to d_k and a step length of $\alpha_k = 1$, since by definition $p_k\alpha_k = d_k$.

The newton method has some limitations, since for nonlinear functions there may be situations in which $f(z_k + p_k\alpha_k) > f(z_k)$, meaning that the convergence of the problem cannot be guaranteed [43]. In addition, cases in which a quadratic approximation of the objective function is a poor choice may result in failure of the algorithm. There are modified versions of the Newton method that try to tackle some of these limitations.

Constrained Optimization - Interior Point Methods

Constrained optimization methods work by converting the constrained problem into a set of unconstrained problems that can be solved using the algorithms presented in section 3.1.2 [43].

There are many types of constrained optimization methods, such as the penalty and barrier methods,

sequential quadratic programming methods, reduce gradient methods and feasible direction methods [43]. In the context of the work developed, the attention will be focused on penalty and barrier algorithms.

Penalty and barrier methods convert the system constraints into a penalty function, which is then added to the objective function. This way, the infeasibility of the constraints is minimised together with the objective function. Depending on the nature of the penalty function, the method can be classified as penalty or barrier methods.

Penalty methods use functions that penalize only when the design point is outside feasible region. A typical penalty function for these cases is [43]

$$\begin{cases} \phi(\boldsymbol{z}) = 0, & \text{if } \boldsymbol{z} \text{ feasible} \\ \phi(\boldsymbol{z}) > 0, & \text{otherwise.} \end{cases} \tag{3.5}$$

Barrier methods or Interior-point methods impose penalty functions that penalize the objective function as it approaches the boundary of the feasible region. This methodology has the advantage that the intermediate solutions are always feasible. To better understand how interior methods work consider the generic inequality constrained problem,

$$\begin{aligned} \text{minimise} \quad & f(\boldsymbol{z}) \\ \text{by varying} \quad & \boldsymbol{z} \in \mathbb{R}^N, \\ \text{subject to} \quad & g_m(\boldsymbol{z}) \geq 0, m = 1, 2, ..., N_g, \end{aligned} \tag{3.6}$$

the inequality constraint, can be replaced, for instance, by a logarithmic barrier function in the objective function of the problem. The previous problem statement then becomes an unconstrained problem,

$$\begin{aligned} \text{minimise} \quad & f(\boldsymbol{z}) - \mu \sum_{i=1}^{m} \log(g_i(\boldsymbol{z})), \\ \text{by varying} \quad & \boldsymbol{z} \in \mathbb{R}^N. \end{aligned} \tag{3.7}$$

Looking at this new formulation, it is possible to see how the problem becomes an unconstrained problem. In the new penalty function the term $\mu \sum_{i=1}^{m} \log(g_i(\boldsymbol{z}))$ becomes more negative as the solution approximates the constraint limit, resulting in a higher value for the objective function. The quantity μ is called barrier parameter that defines how strongly the optimization is penalized for approaching the limit, as μ increases the penalty also increases.

The new unconstrained problem can now be solved, for example, using the Newton method technique presented in section 3.1.2.

3.1.3 Stochastic Optimization Methods

Stochastic optimization methods include randomness in their implementation. Some stochastic algorithms combine a randomness component with a deterministic methods. A simple example of such algorithm is the hill climb algorithm with random restart. It uses a deterministic method of following the

path of highest gradient but includes a stochastic element corresponding to a restart into a random point when the algorithm gets stuck [44].

Algorithms of this kind are designed not to find the optimal solution but to find quality solutions in reasonable time for problems to which is not possible to perform a complete search of possible solutions. They are designed to be practical algorithms to obtain quality solutions [45]. Examples of stochastic algorithms include genetic algorithms and particle swarm algorithms.

3.2 Trajectory Optimization Problems

3.2.1 Formulating A Trajectory Optimization Problem

Optimal control or trajectory optimization is a set of techniques that tries to find the trajectory that optimizes a given objective function, by changing the available inputs, while respecting the set of constraints of the problem [46]. Trajectory optimization procedures include in their core an optimization algorithm, such as the ones presented in section 3.1.

An optimal trajectory problem is a particular type of optimization problem. It is defined, first of all, by its state and control variables. The state variables $\boldsymbol{x}$ represent, as the name suggests, the state of the system, while the control variables $\boldsymbol{u}$ represent the inputs that can be given to the system in order to change its state. An objective function of the type,

$$\min_{t_0, t_f, \boldsymbol{x}(t), \boldsymbol{u}(t)} J(t_0, t_f, \boldsymbol{x}(t_0), \boldsymbol{x}(t_f)) + \int_{t_0}^{t_f} w(\tau, \boldsymbol{x}(\tau), \boldsymbol{u}(\tau)) d\tau \tag{3.8a}$$

is a fundamental part of the definition of an optimization problem. This function can be divided into an objective in the boundary represented by the J function, and a path objective represented by the w integrand. The optimization will try to minimise this function with respect to the initial time t_0, final time t_f, the state variables $x(t)$ and control variables $u(t)$ while respecting a series of constraints of the system.

The first set of constraints that must be respected by the optimization technique are the system dynamics,

$$\dot{\boldsymbol{x}} = f(t, \boldsymbol{x}(t), \boldsymbol{u}(t)), \tag{3.8b}$$

which are, in general, constitude by a set of differential equations similar to the ones presented in chapter 2. In addition to the system dynamics there are also path constraints, which are functions of the state and control variables that limit the dynamics of the system during its trajectory,

$$h(t, \boldsymbol{x}(t), \boldsymbol{u}(t)) \leq 0. \tag{3.8c}$$

In a similar way, there can also be constraints to the dynamics as function of the values of state and control variables on the boundaries of the trajectory,

$$g(t_0, t_f, \boldsymbol{x}(t_0), \boldsymbol{x}(t_F)) \leq 0. \tag{3.8d}$$

The upper and lower limits for the state and control variables must also be defined,

$$\boldsymbol{x}_{low} \leq \boldsymbol{x}(t) \leq \boldsymbol{x}_{upp}, \tag{3.8e}$$

$$\boldsymbol{u}_{low} \leq \boldsymbol{u}(t) \leq \boldsymbol{u}_{upp}. \tag{3.8f}$$

Finally, it is necessary to establish the bounds on time, the initial state and final state of the system, respectively,

$$t_{low} \leq t_0 \leq t_f \leq t_{upp}, \tag{3.8g}$$

$$\boldsymbol{x}_{0,low} \leq \boldsymbol{x}_0 \leq \boldsymbol{x}_{0,upp}, \tag{3.8h}$$

$$\boldsymbol{x}_{f,low} \leq \boldsymbol{x}_f \leq \boldsymbol{x}_{f,upp}. \tag{3.8i}$$

Note that if $\boldsymbol{x}_{0,upp} = \boldsymbol{x}_{0,low}$ then it means that initial state of the trajectory is fixed. The same can be said in relation to the final state and control variables.

3.2.2 Trajectory Optimization for a UAV

The problem of optimizing a UAV trajectory can be written using the concepts presented in section 3.2.1.

As referenced in chapter 2, the system dynamics that will govern the UAV's behaviour are given by the set of equations (2.32), the EoM in the flight path frame. Thus, the state variables of the problem chosen are

$$\boldsymbol{x} = \begin{bmatrix} x & y & z & V_A & \psi & \gamma \end{bmatrix}, \tag{3.9}$$

with the control variables

$$\boldsymbol{u} = \begin{bmatrix} C_L & \phi \end{bmatrix}. \tag{3.10}$$

This choice of state and control variables is natural for the dynamics of the system since the UAV's position and direction are completely defined by the state variables, and the control variables are able to change its motion according with the EoM.

Trajectory Constraints

In addition to the system dynamics, the UAV trajectory is subjected to other sets of constraints. The first set of constraints that must be defined are the bounds to the state and control variables (equations (3.8e) and (3.8f)). Table (3.1) presents the lower and upper limits of these variables.

Table 3.1: Bounds on the state and control variables.

Variable	x	y	h	V_A	ψ	γ	C_L	ϕ
Lower limit	$-100m$	$-100m$	$1.5m$	$0m/s$	$-\inf$	$\frac{-\pi}{3}$	0	$\frac{-\pi}{3}$
Upper limit	$100m$	$100m$	$100m$	$50m/s$	$\inf$	$\frac{\pi}{3}$	1.5	$\frac{\pi}{3}$

The limit values for the vehicle coordinates were chosen in such a way that the available region is large enough to perform the trajectory, but small enough that the assumption of constant wind is valid. The bounds in the airspeed, heading angle, flight path angle and control variables were chosen considering a conservative approach on what are the capabilities of the aerial vehicle. The values chosen are similar to those usually used in this type of research [16, 35, 41].

The vehicle is subjected, also, to a path constraint, of the type of equation (3.8c), during all its motion the UAV must be subjected to a load factor smaller than 3, resulting in the constraint

$$n = \frac{L}{W} = \frac{0.5\rho S V_A^2 C_L}{mg} \leq 3. \tag{3.11}$$

The load factor represents a structural constraint of the vehicle. The value of the load factor represents the number of times the structure must support its own weight. A load factor of 3 constitutes a conservative number for a UAV.

Finally, the bounds on time, the initial state and the final state must be defined. Time is bounded between 0 seconds and a higher limit that is adapted depending on the optimization being performed, usually 30 seconds. Since the initial state is fixed, the lower and upper bounds for the initial state are equal and have the values of table 3.2.

Table 3.2: Initial conditions for the UAV trajectory.

	x	y	h	V_A	ψ	γ
Initial state	$0m$	$0m$	$1.5m$	$20m/s$	$\frac{\pi}{2}rad$	$0rad$

The initial conditions were chosen in such a way that the vehicle has small potential energy and large kinetic energy. For these initial conditions, it is possible to analyse all phases of dynamic soaring, since they correspond to the conditions expected to find at the end of the lower turn.

The final state bounds may vary depending on the type of trajectory desired. For energy neutral trajectories, table 3.3 presents the bounds for the final state both for open and closed trajectories.

Table 3.3: Bounds on the final state for energy-neutral trajectories.

Trajectory type		x	y	h	V_A	ψ	γ
Open trajectory	Lower limit	x_{min}	y_{min}	z_{min}	V_{A_0}	ψ_0	γ_0
	Upper limit	x_{max}	y_{max}	z_{max}	V_{A_0}	ψ_0	γ_0
Closed trajectory	Lower limit	x_0	y_0	z_0	V_{A_0}	$\psi_0 + 2\pi n$	γ_0
	Upper limit	x_0	y_0	z_0	V_{A_0}	$\psi_0 + 2\pi n$	γ_0

Note that open trajectory final conditions will only be used for the validation of the numerical method. For closed trajectories note that the value of the heading angle should also be a multiple of 2π, the constant n will determine the number of loops performed by the trajectory. Besides that, the final airspeed and flight path angles are chosen to be always equal to the initial conditions in order to ensure repeatability.

Objective Functions

The objective function (3.8a) defines the result obtained from the optimizer since it will try to minimise the value of this function while respecting all previously defined constraints. Depending on the study being performed, different objective functions can be used.

One useful objective function can be to minimise the wind strength required for obtaining an energy-neutral trajectory,

$$\min W_{ref}. \tag{3.12}$$

This objective function is used by Sachs [16, 28] and serves as a good starting point for the study of dynamic soaring.

Depending on the wind profile being considered, different parameters are used. While for the logarithmic wind profile it is desired to minimise the wind speed at the reference height, W_{ref} (eq. (2.17)), for the linear wind profile the parameter to minimise is the wind slope β (eq. (2.16)), and for step wind profiles is the maximum wind speed, A (eq. (2.18)).

When the objective is to study how to maximize the time aloft, a possible function is to maximize the final time,

$$\max t_f. \tag{3.13}$$

This function works as an alternative when it is desired to totally prescribe the wind profile.

3.2.3 Solving a Trajectory Optimization Problem

The trajectory optimization problem posed in section 3.2.2 is a multi-variable, constrained and non-linear problem, meaning they require numerical techniques to be solved.

The numerical methods used to solve trajectory optimization problems can be divided into two categories, direct and indirect methods. Direct methods discretize the optimization problem into a finite-dimension problem and then try to solve the discretized version using an Non-Linear Programming (NLP) solver. On the contrary, an indirect method makes the optimization first, using information from the gradients of the problems and then finishes with the discretization. Indirect methods are more accurate but much more complex than direct methods [41, 46].

Following the work of several authors [29, 34–36] the present work will focus in direct methods. These type of methods have, essentially, two phases: a transcription phase that converts the problem into a NLP, of the type of equation (3.7); a solving phase where a NLP solver applies one of the algorithms described in section 3.1 to find the solution.

Transcription

The first step to solve the problem stated in section 3.2.2 is to pose it in such a way that it can be solved by a NLP solver. In general, the problem is converted so that it respects the form given by equation (3.7).

The transformation procedure involves the use of a collocation method that discretizes the continuous problem into a discrete problem. There are many different techniques to transcribe the problem into NLP form. Mir presents an extensive list of available transcription methods [41]. Here only global and local direct collocation methods will be mentioned.

Local collocation methods start by converting the continuous trajectory into a set of points in time, called collocation points, each one with a specific value for the state and control variables. So if the UAV trajectory is discretized into N points, in a time interval $[0, t_f]$, there are N time unknowns,

$$\boldsymbol{t} = t_0, ..., t_k, ..., t_N, \tag{3.14}$$

6N state unknowns,

$$\boldsymbol{x} = x_0^i, ..., x_k^i, ..., x_N^i, i = 1, 2, 3, 4, 5, 6, \tag{3.15}$$

and 2N control unknowns,

$$\boldsymbol{u} = u_0^j, ..., u_k^j, ..., u_N^j, j = 1, 2, \tag{3.16}$$

resulting in a total of 9N unknowns. This set of unknowns represents the set of variables that comprise the design vector z. Note that after determining the initial and final time of the trajectory, all time unknowns can be calculated using the spacing between the collocation points.

With the trajectory discretized, it is also necessary to discretize the continuous system dynamics, represented by the differential equations. To discretize them, an integration rule is used, such as the trapezoidal rule. The numerical integration of the differential equations between two collocation points establishes a relationship between them.

For a generic differential equation,

$$\dot{x^i} = f^i(\boldsymbol{x}(t), \boldsymbol{u}(t)), \tag{3.17}$$

the use of the trapezoidal rule establishes a relationship between two consecutive collocation points [36],

$$(x_{k+1}^i - x_k^i) - \frac{1}{2}(f_k^i + f_{k+1}^i)(t_{k+1} - t_k) = 0, \tag{3.18}$$

so for the 6 differential equations that comprise the UAV dynamics, there are a total of 6(N-1) equality constraints related to the system dynamics.

The path constraints are applied independently to each collocation point, since at each point the trajectory must respect that constraint. So for a single path constraint, there will be N constraints in the NLP. The bounds on state and control variables are also defined for each collocation point, resulting in more 16N inequality constraints for the case of the NLP of the UAV problem (each collocation point must respect 8 upper and lower bounds of the state and control variables).

Instead of using the trapezoidal rule to discretize the system dynamics, other numerical rules can be used. Another possibility is to use Hermite-Simpson integration rule. Applying the new integration rule on the generic system dynamics defined by equation (3.17), results in the following constraint between

collocation points,

$$(x_k^i + x_{k+1}^i) = \frac{1}{6}(t_{k+1} - t_k)(f_k^i + 4f_{k+\frac{1}{2}}^i + f_{k+1}^i), \tag{3.19a}$$

where the midpoint $x_{k+\frac{1}{2}}^i$ necessary to compute $f_{k+\frac{1}{2}}^i$ is obtained by interpolation as

$$x_{k+\frac{1}{2}}^i = \frac{1}{2}(x_k^i + x_{k+1}^i) - \frac{1}{8}(f_{k+1} - f_k)(t_{k+1} - t_k). \tag{3.19b}$$

This rule provides a solution that is higher-order accurate than the one obtained by the trapezoidal rule, since it approximates the objective function and system dynamics as quadratic functions, while the trapezoidal rule does the same approximation using linear functions. An additional benefit for the Hermite-Simpson rule is the fact that the state trajectory obtained is a cubic Hermite spline, which has continuous first derivative [46].

The main drawback of using the Hermite-Simpson integration rule over the trapezoidal rule, is the increased complexity and consequently increased computational time. Following the procedure presented by Sachs [18, 36] and due to its simplicity and quick computation time, the trapezoidal rule will be the only local collocation method considered from this moment onward. Any potential losses in accuracy can be compensated using a higher number of collocation points.

A different approach is used by global collocation methods for the transcription of the problem. For instance, the Legendre-Gauss-Radau (LGR) global collocation method starts by dividing the continuous trajectory into a set of N_s intervals. In each interval, the trajectory is approximated by a Legendre polynomial of degree N_p, resulting in N_p collocation points per interval [47]. The position of the collocation points in each interval is given through the roots of the polynomial or by another rule. In the case of the Legendre-Gauss-Radau collocation, the collocation points are the roots of the polynomial,

$$P_{N_p}(t) + P_{N_p-1}(t), \tag{3.20}$$

where P_N is the Legendre polynomial of order N_p and P_{N_p-1} is the Legendre polynomial of order $N_p - 1$ order. This approach has the particularity that the first collocation point of each interval matches the start of the interval. Note that because the method uses Legendre polynomials the spacing between collocation points is not uniform [46].

The main advantage of LGR collocation method is the high accuracy from the use of high-order polynomial functions. The main drawback is the high computational load they create. At the end of this chapter it will be possible to compare the results obtained using the trapezoidal local collocation method and the LGR global collocation method.

Figure 3.1 presents a comparison between the three collocation methods here described. Notice how the hermite-simpson approximates the function between collocation points using second-order polynomials. The LGR collocation here presented uses one interval and a Legendre polynomial of fourth-order, notice how the collocation points are not equally spaced.

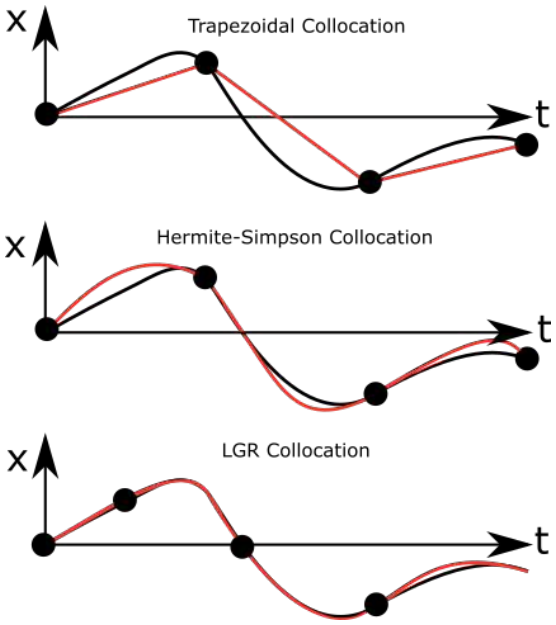

Figure 3.1: Comparison between the three transcription methods mentioned.

Solving the NLP

The NLP obtained from the transcription can be solved using one of the algorithms presented in section 3.1. The transcribed problem is multi-variable, constrained, deterministic and non-linear, meaning that from the presented algorithms, the best candidates are the interior point methods.

Interior point methods are specially designed to tackle this kind of problems, being robust and well documented methods. Their great drawback is that the solutions obtained are only guaranteed to be a local optimal solution. Thus, to make sure the obtained result is the global optimal solution, different initial guesses must be used. Although it is an important limitation, it is one shared for almost all gradient-based optimization methods.

Another approach to try to ensure a global optimal solution is obtained is to use a stochastic optimization algorithm. Although nothing guarantees that the obtained solution is a global optimum, the random nature of the algorithms provides a greater chance of finding it.

For the present case, an interior point method will be used because of their great applicability for trajectory optimization problems. Section 3.3 presents a detailed explanation of the computational procedure utilized.

3.2.4 Initialization and Solution

The general solving methodology, just presented, requires a good initial guess to begin the optimization. Bad guesses may lead the NLP solver not to solve an otherwise correctly posed optimization problem [46].

Different approaches can be taken to obtain good initial guesses, such as using for the first optimization a guess that assumes the trajectory as a straight line or solve a simpler version of the problem and then use the solution obtained as a guess for the full problem [46].

Another characteristic of the procedure, that should be considered with care, is the transcription phase. Associated with the discretization of the trajectory there should be a convergence study that allows for the choice of the most appropriate number of collocation points.

Finally, it is also important to verify that the solution obtained is the global best solution, since the interior point method only guarantees a local optimum solution. The only way of assuring that the solution obtained is the global best solution is by using different initial guesses and checking if the same solution is always obtained.

3.3 Computational Implementation

In the developed work the transcription was made using the Imperial College London Optimal Control Software (ICLOCS2) that provides tools to transcribe the UAV trajectory optimization problem into an NLP using the collocation techniques mentioned previously. In addition, ICLOCS2 also provides an interface for direct communication with the NLP solver. ICLOCS2 runs in the MATLAB® environment [48].

ICLOCS2 transcription is passed to the Interior Point Optimizer (IPOPT), the NLP solver choosen for the present work. IPOPT uses an interior point method [49] of the type presented in section 3.1.2. The fact that IPOPT uses a deterministic gradient-based algorithm makes it appropriate for rapidly solving the multi-variable, constrained trajectory optimization problems of interest. In addition ICLOCS2 can interface directly with IPOPT, creating a stable and robust environment to solve trajectory optimization problems.

The trajectory obtained from IPOPT is, finally, post-processed to plot the trajectory graphs and to obtain the evolution of the system's energy through time. Figure 3.2 presents a schematic representation of the work flow of the computational method.

3.3.1 Verification

The optimization procedure just described can be verified by comparing the results obtained with the results obtained by Sachs [16], in which a open dynamic soaring trajectory that minimises the required wind strength in logarithmic wind conditions was presented. The minimum wind strength obtained was 8.6 m/s. This verification step has three purposes: first, it assures the results obtained are accurate; second it allows for the comparison of the different transcription methods presented; and finally, it can be used to make the necessary convergence studies.

Figure 3.3 presents the convergence study for the optimization procedure, when using the trapezoidal integration rule to make the problem's transcription. Looking at the data, it is possible to verify that the value has already converged to 8.77 m/s with N equal to 200, corresponding to an error of 2 % when compared with values obtained by Sachs. The small discrepancy is due to the fact that the exact conditions used by Sachs could not be recreated since not all required information is available regarding the optimization procedure. Nevertheless, it is safe to conclude that the results obtained using the

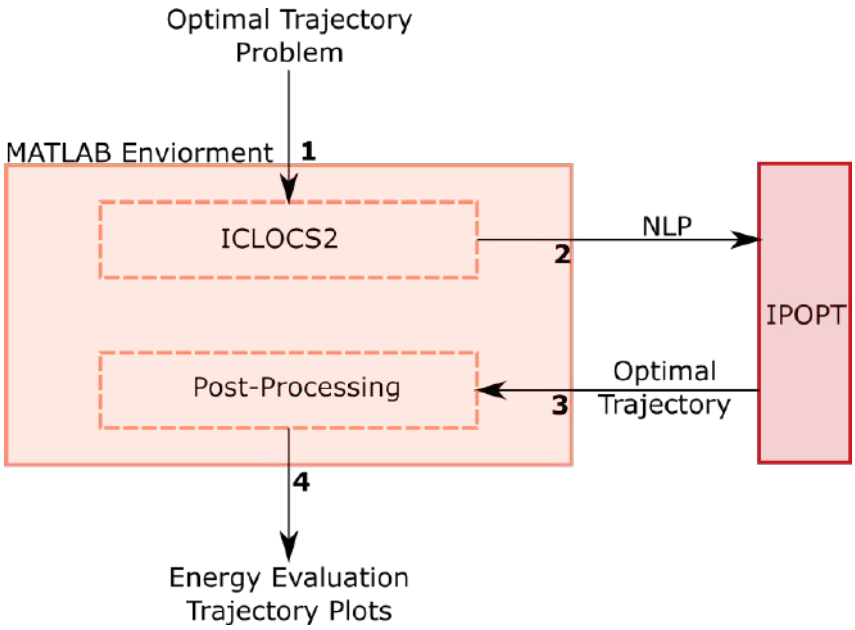

Figure 3.2: Schematic representation of the various steps of the numerical procedure used. 1 - Optimal trajectory problem is passed to ICLOCS2 for transcription; 2 - The resulting NLP is passed to IPOPT for solving; 3 - The optimized trajectory is returned to MATLAB for post-processing; 4 - The final results are saved in the machine for further analysis.

trapezoidal rule are accurate when N is equal or higher to 200.

N	Time Elapsed (s)	Minimum Wind Strength (m/s)
20	4.79	9.061
60	5.02	8.807
100	5.72	8.783
200	6.27	8.773
300	9.19	8.770
400	9.23	8.768
500	10.05	8.766

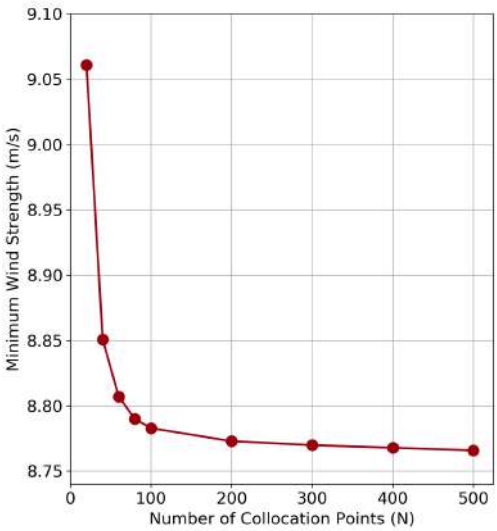

Figure 3.3: Accuracy and convergence study of optimization procedure using the trapezoidal rule as collocation method.

A similar study can be made for the case of the LGR global collocation method. Figure 3.4 presents the convergence study for the LGR method using polynomials of the fourth degree. For this method, the convergence occurs just after using 15 intervals (60 collocation points), the converged result is 8.77 m/s corresponding to an error of 2% relative to Sach's results. Although only 60 collocation points are needed to converge the result, the computational time associated with this method is much larger than

the one associated with the trapezoidal method.

N_s	N	Time Elapsed (s)	Minimum Wind Strength (m/s)
5	20	7.883	8.748
10	40	11.795	8.756
15	60	17.897	8.770
20	80	21.056	8.770
25	100	28.092	8.770
50	200	60.969	8.770
75	300	111.701	8.770
100	400	191.391	8.769
125	500	244.913	8.769

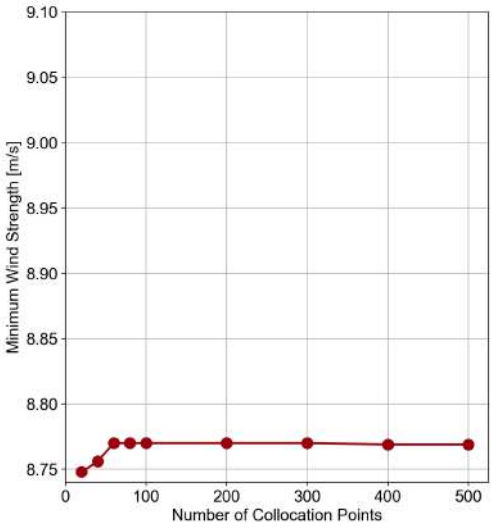

Figure 3.4: Accuracy and convergence study of the optimization procedure using the LGR collocation method with fourth degree Legendre polynomials ($N_p = 4$).

Therefore, if the same final converged value is obtained for both methods, then the choice of the computational method should be based in its computational load. For this reason, the results presented in the following chapters were obtained using the trapezoidal method as transcription method, with N equal to 300, since it ensures an accurate result even for optimizations in which the final time is larger than the reference case here used.

Finally, it is necessary to verify whether the obtained results are the global optimal solution or just a local optimal solution. As previously stated the only way to try to check if the obtained solution is the global best one is to initialize the problem with different guesses and compare the obtained. Using this technique it was possible to verify that the solutions obtained were always the same, meaning that the results obtained should be the global optimal solution.

3.4 Summary of the Computational Method

From the previous analysis, it was possible to see that a trajectory optimization procedure using trapezoidal collocation for transcription and an interior-point method for solving the resulting NLP, yields accurate results that seem to be the global optimal solutions to the problem.

The methodology described will be the foundation of the results presented in the next chapters. All the trajectories presented will have been obtained using this computational procedure.

Chapter 4

Energy-Harvesting Mechanism

An in-depth analysis of the energy-harvesting mechanism associated with dynamic soaring must be done before presenting any other results since the discussion of any optimal trajectory requires an understanding of the underlying mechanism that allows for dynamic soaring to happen. At the start of this chapter, a brief presentation of the optimisation problem is made. Afterwards, each section will analyse a different flight phase of dynamic soaring. In the end, all phases are linked together and an overview of the full trajectory is made.

4.1 Problem Description

The aim is to understand how the different phases of the dynamic soaring trajectory contribute to the maintenance energy-neutral condition. Thus, since dynamic soaring may be of particular interest for applications of surveillance, the analysis of the energy-harvesting mechanism will be made considering a closed trajectory, obtained using the previously presented computational method. Moreover, it will be a closed trajectory that minimises the wind strength required for an energy-neutral loop, meaning that at the end of the trajectory, the vehicle will have maintained its initial potential and kinetic energy. During its motion, the vehicle will be subjected to a linear wind profile, chosen for its simplicity. More realistic and complex wind profiles will be considered in the subsequent chapters.

To obtain such a trajectory the objective function used was

$$\min \beta, \tag{4.1}$$

and the constraints and bounds to the system utilized are the ones presented in tables 3.1, 3.2 and 3.3 of section 3.2.2.

4.2 Energy-Neutral Loop in Linear Wind Conditions

Figures 4.1 and 4.2 present the optimal trajectory obtained from the numerical procedure. The minimised slope obtained for the linear wind profile (β of eq. (2.16)), was $0.3s^{-1}$, which corresponds to a wind velocity of 6m/s at an altitude of 20m.

The solution was obtained using 300 collocation points and a IPOPT tolerance for convergence of 10^{-7}. The open trajectory from the verification step was used as the initial guess. The numerical tool required 217 iterations to obtain the final solution which corresponded to a computational time of 186s in a computer with a Intel® Core™ i7-8750H @ 2.20Hz processor. The vector of collocation points outputted from the numerical method can be found in appendix C.

As previously mentioned, any dynamic soaring trajectory can be divided into essentially four phases. A climb into the wind, an upper turn, a descent with the wind, and finally a lower turn. For the present case the following approximate division can be made:

- Climb: from 1s to 3.5s;
- Upper Turn: from 3.5s to 5.5s;
- Descent: from 5.5s to 7s;
- Lower Turn: from 0s to 1s and from 7s to 8s.

For a better understanding of the dynamic soaring mechanism, each phase will be analysed separately.

4.2.1 Climb Phase

During the climbing phase, altitude is gained in exchange for a loss in airspeed. Because the UAV is going into the wind, during this phase the ground speed is always lower than the airspeed, figure 4.2 shows just that. In addition, while climbing, the flight path angle is positive ($\gamma > 0$), the heading angle is between $\frac{\pi}{2}$ and $\frac{3\pi}{2}$ since the UAV it is pointing in the southward direction (against the wind blowing north) and, because it is a closed-loop trajectory, the UAV banks right ($\phi > 0$).

Looking at the power contributions, also presented in figure 4.2, it is possible to verify that while climbing the lift contribution is positive and increases over time, a result of the increasing wind speed. This positive contribution can be explained looking at equation (2.37),

$$\frac{dE_m}{dt} = -LW_x^E(\cos\phi\sin\gamma\cos\psi + \sin\phi\sin\psi) - DV_A - DW_x^E\cos\gamma\cos\psi. \tag{2.37}$$

For the flight conditions mentioned, the lift contributes positively to the variation of energy and its contribution is proportional to the wind strength. In contrast, and as expected, the drag contributes negatively to the variation of energy, 4.2 supports this analysis. Nevertheless, a closer look at equation (2.37) reveals that, during the climb, the term $DW_x^E\cos\gamma\cos\psi$ is positive, meaning that part of the drag seems to be attenuating the overall negative contribution of the drag very slightly. The mentioned term might be

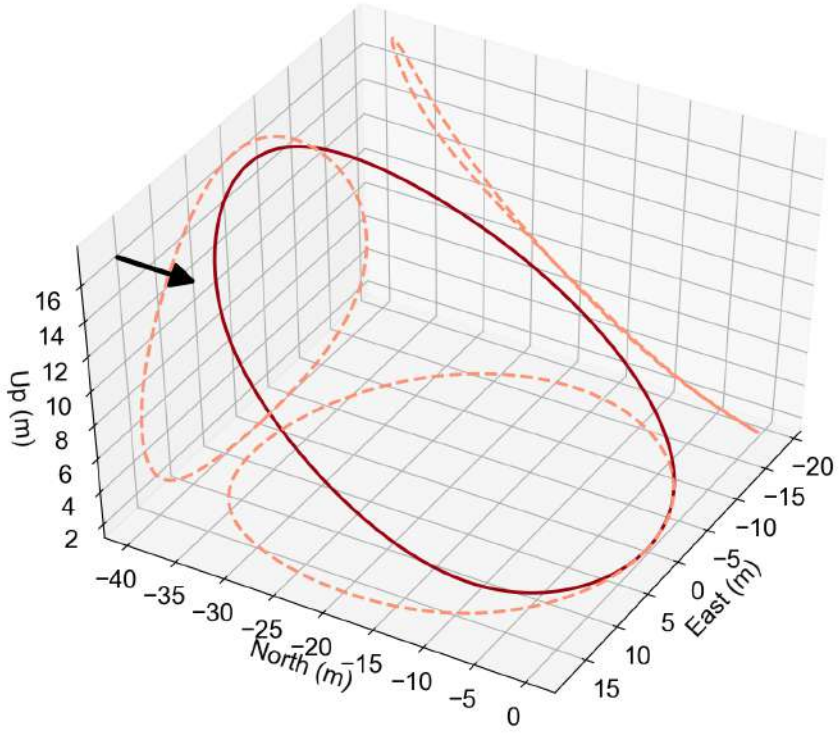

Figure 4.1: Optimal single-loop, energy-neutral trajectory that minimises the wind strength required in a linear wind profile. Arrow indicates the wind direction. The dashed lines represent the trajectory projections, on each of the three planes. The vehicle travels in the clock-wise direction.

positive but the total contribution, $-DV_A - DW_x^E \cos\gamma \cos\psi$, is always negative. In figure 4.2, only the overall drag contribution is presented, which is always negative.

To better understand how the lift can contribute positively to the overall energy of the system, it is helpful to consider a simplified case in which the climb occurs with wings levelled ($\phi = 0$) and with the UAV pointing directly southward ($\psi = \pi$). These assumptions can be made without loss of generality. For the simplified case, equation (2.37) becomes

$$\frac{dE_m}{dt} = LW_x^E \sin\gamma + DW_x^E \cos\gamma - DV_A, \tag{4.2}$$

and for a positive variation of the mechanical energy,

$$\frac{L}{D}\frac{W_x^E}{V_A}\sin\gamma + \frac{W_x^E}{V_A}\cos\gamma - 1 > 0, \tag{4.3}$$

which means that during the climb, the energy gains depend essentially on the wind strength and on the L/D ratio. Figure 4.3 presents a schematic of the forces acting of the UAV during the climb, where it is possible to see how a component of the lift vector acts in the direction of the ground speed, acting as

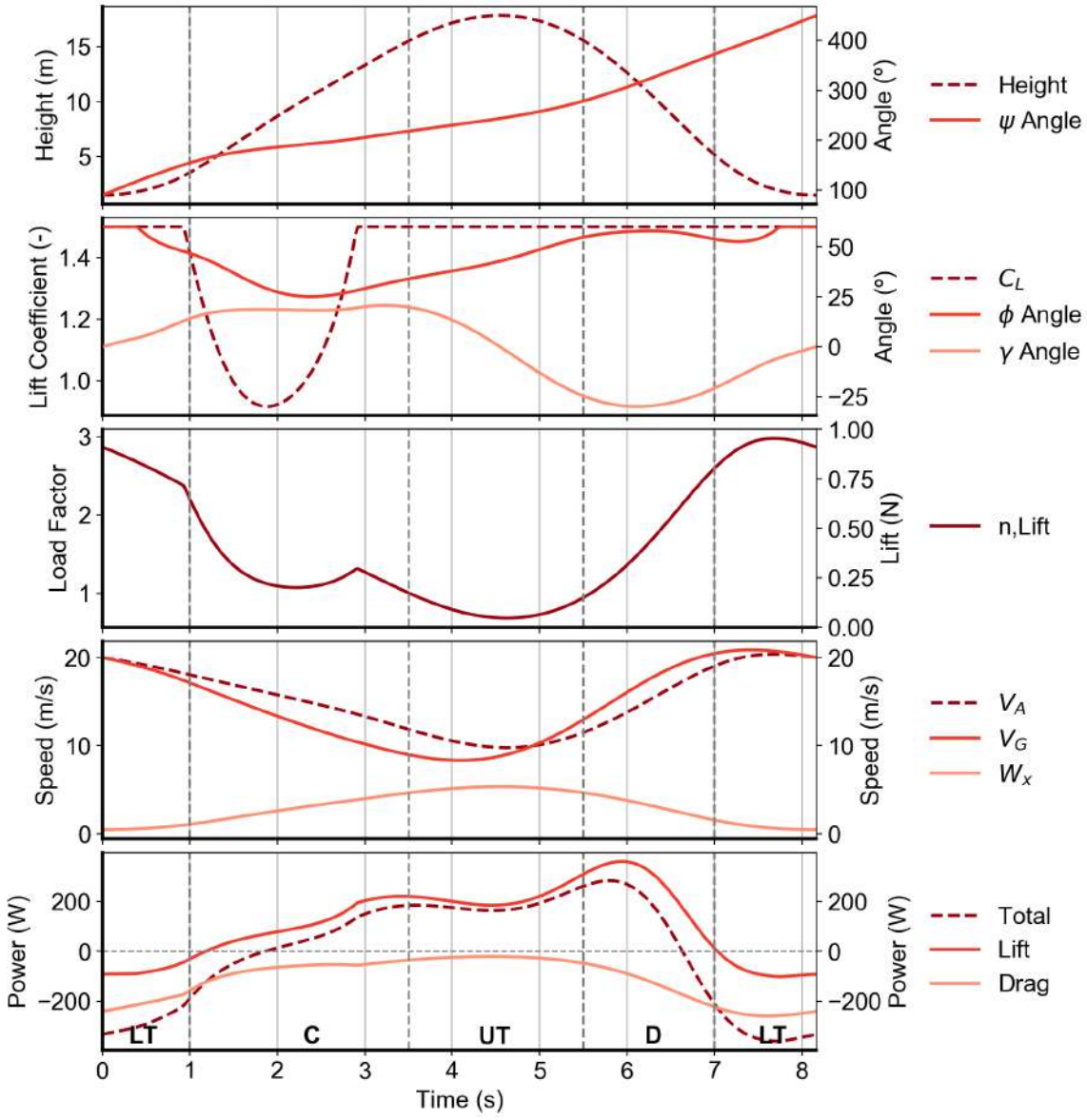

Figure 4.2: Detailed evolution of the principal parameters of the optimal trajectory that minimises the wind strength required for a linear wind profile. The first panel presents the evolution of the altitude and heading angle with time. The second panel presents the evolution of the control variables and the flight path angle. The third panel presents the evolution of the lift and load factor with time (the lines are coincident). The fourth panel presents the evolution of the ground speed, airspeed and wind speed throughout the trajectory. Finally, the last panel presents the evolution of the lift and drag contributions for the variation of the mechanical energy, as well as the overall variation of the energy (LT - Lower Turn, C - Climb, UT - Upper Turn, D - Descent).

a pseudo thrust force, providing energy to the vehicle. The term pseudo comes from the fact that the component acts in the direction of the ground speed and not the airspeed.

The pseudo thrust force only exists as a result of the existent wind velocity vector. When the wind strength is zero, the air velocity vector and ground velocity vector are the same and the lift is orthogonal to both, not providing energy to the system.

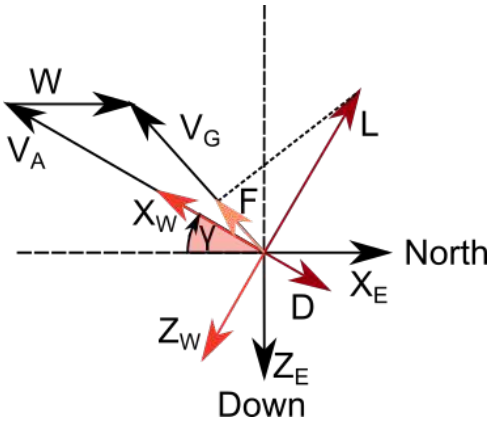

Figure 4.3: Diagram of forces, in the vertical plane, during the climb phase, for wing levelled conditions ($\phi = 0$) and pointing south ($\psi = \pi$). F represents the component of the lift acting as a pseudo thrust.(See [37]).

4.2.2 Upper-Turn Phase

The next phase of the flight is the upper turn. During this phase, the UAV continues the turn to the right ($\phi > 0$) and goes from facing southward to facing northward, so that it may, eventually, descend with the wind. In addition, the flight path angle goes from positive to negative in preparation for the descent. Also, in this phase, the UAV reaches its maximum altitude and minimum airspeed.

For the described conditions, and looking again at equation (2.37) and figure 4.2, it is possible to verify that the lift continues to provide energy to the UAV. The drag also continues to contribute to the energy variation negatively. The small drag contribution $-DW_x^E \cos\gamma \cos\psi$ goes from attenuating the drag losses to also contribute negatively to the energy of the system, since the signal of $\cos\psi$ changes.

Figure 4.4 presents the schematic of the forces acting on the UAV in the upper turn, for the simplified case where it is assumed the turn occurs in leveled flight ($\gamma = 0$). In this conditions, equation (2.37) becomes

$$\frac{dE_m}{dt} = -LW_x^E \sin\phi \sin\psi - DV_A - DW_x^E \cos\psi. \tag{4.4}$$

During a turn from $\psi = \pi$ to $\psi = 2\pi$, $\sin\psi < 0$ and $\sin\phi > 0$, resulting in a positive contribution from the lift throughout the turn.

4.2.3 Descent Phase

The descent phase is characterized by an altitude loss in exchange for an airspeed gain. During this phase, the ground speed is always higher than the airspeed because the UAV is descending with the wind.

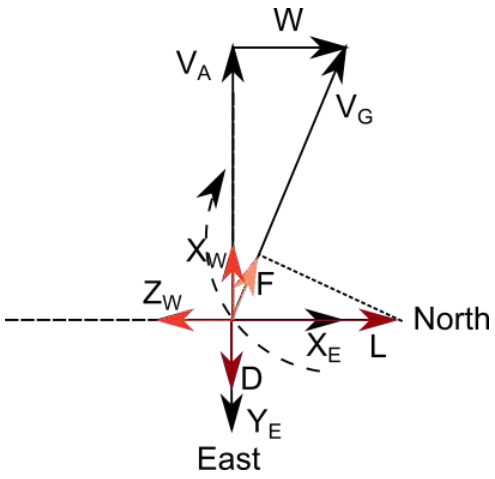

Figure 4.4: Diagram of forces, in the horizontal plane, for the middle of the upper turn ($\psi = 3\pi/2$) and for leveled flight ($\gamma = 0$). F represents the component of the lift acting as a pseudo thrust (See [37]).

For the case of the loop presented, during the descent, the UAV continues to bank right ($\phi > 0$), while the flight path angle is negative ($\gamma < 0$), and the vehicle is pointing northward ($3\frac{\pi}{2} < \psi < 5\frac{\pi}{2}$).

Looking at the evolution of the energy contributions present in figure 4.2, it is possible to verify that the lift keeps providing a positive contribution to the energy of the system. Comparing the schematic representation of the climb and descent, it is possible to understand the difference in drag contribution between these two phases. This difference is due to the fact that the projection of the drag in the ground speed direction is larger for the case of the descent than for the climb. The term $-DW_x^E \cos\gamma \cos\psi$ represents this difference.

If the simplified case of descent without banking ($\phi = 0$) and facing directly north ($\psi = 0$) is considered, then equation (2.37) becomes

$$\frac{dE_m}{dt} = -LW_x^E \sin\gamma - DV_A - DW_x^E \cos\gamma, \tag{4.5}$$

and, to insure a positive rate for the mechanical energy, the following condition must be respected,

$$-\frac{L}{D}\frac{W_x^E}{V_A}\sin\gamma - \frac{W_x^E}{V_A}\cos\gamma - 1 > 0. \tag{4.6}$$

It is then clear that the lift contribution is still positive and, just as in the climb, depends on the wind-strength and L/D ratio. Figure 4.5 presents the schematic representation of the simplified case of the descent.

If a close analysis of the evolution of the lift contribution during the first three phases of flight is made, it is possible to find that there are two maximums to the lift contribution. The first maximum occurs at around 3.5 seconds, and corresponds to the point where the lift coefficient reaches its maximum value near the maximum altitude. From that point onward the lift coefficient remains constant, since it cannot increase more due to system constraints, but the airspeed keeps decreasing, and the wind strength cannot make the difference, resulting in a local minimum of the lift contribution, around 4.5 seconds. With the start of the descent, the airspeed increases again, and as a consequence, so does the lift

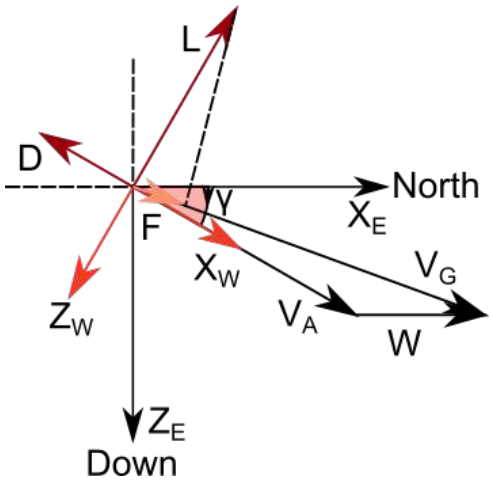

Figure 4.5: Diagram of forces, in the vertical plane of the UAV, during the descent phase without banking ($\phi = 0$) and pointing north ($\psi = 2\pi$). F represents the component of the lift acting as a pseudo thrust. (See [37])

contribution, reaching a new maximum at 6 seconds. During the rest of the descent, the wind speed starts to decrease, and so does the lift contribution.

4.2.4 Lower-Turn Phase

Finally, the last phase of the flight is the lower turn, that will bring the UAV to its initial conditions. This phase is characterized by being part of the flight where the energy losses of the system occur. Looking at figure 4.2, it is possible to verify that during this phase the rate of mechanical energy of the system is negative and both the lift and drag contributions are negative.

During this phase, the UAV continues to bank right ($\phi > 0$), the flight path angle goes from negative to positive, and the UAV goes from pointing northward to southward in preparation for another loop.

Equation (2.37) allows for the understanding of why the lift contributes negatively during this phase. This negative contribution is better understood when considering the simplified case in which it is assumed that the turn occurs with flight path angle equal to zero ($\gamma = 0$), simplifying equation (2.37) to

$$\frac{dE_m}{dt} = -LW_x^E \sin\phi \sin\psi - DV_A - DW_x^E \cos\psi. \tag{4.7}$$

Looking at the simplified equation, it is possible to verify that, when wind is present, the lift contributes negatively, since $\sin\psi > 0$ in a turn from 2π to 3π. Figure 4.6 presents the schematization of this simplified flight phase.

4.3 Summary of the Energy-Harvesting Mechanism

From the present analysis of a dynamic soaring trajectory, it is possible to determine in which phases of the trajectory the UAV gains or loses energy. The gains are made during the climb, upper turn and descent, and the loses happen during the lower turn, resulting in a net-zero loss of energy. Looking

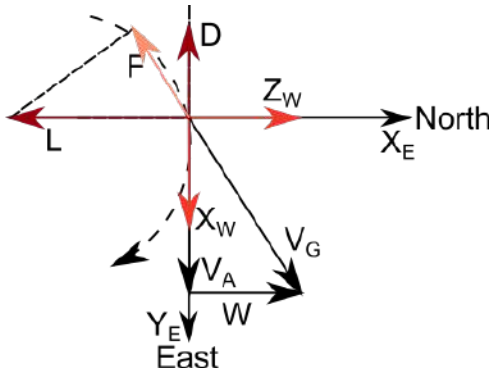

Figure 4.6: Diagram of forces, in the horizontal plane of the UAV, during the lower turn for $\gamma = 0$ and ($\psi = 5\pi/2$). F represents the component of the lift that now acts as an additional drag contribution. (See [37])

at figure 4.7, it is possible to verify that only during the lower turn does the pseudo-thrust act as an additional drag component, while in the other phases it acts as a thrust force.

It becomes evident that the two main factors determining the quantity of energy gained and lost during the trajectory are the wind speed and L/D ratio of the UAV.

Concerning the wind speed, it is its difference between the lower and higher part of the trajectory that allows dynamic soaring to occur since the higher wind speed at the top of trajectory maximise the energy gains, while the lower wind speeds at the bottom of the trajectory minimise the losses.

The L/D ratio is a characteristic of the vehicle, which is harder to modify. It is responsible for the ratio between what is extracted from the lift and what is lost from the drag for the same wind strength. Thus, ideally it would be better to maximise the lift while minimizing the drag during the climb, upper turn, and descent, and minimise both during the lower turn.

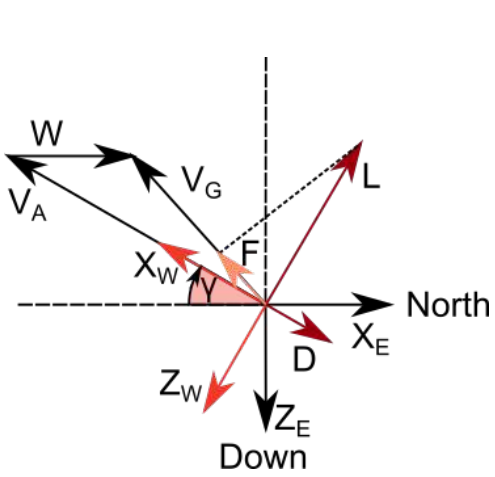

(a) Climb phase.

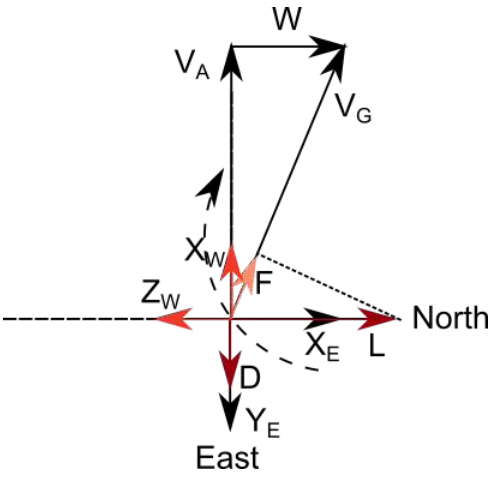

(b) Upper-Turn phase

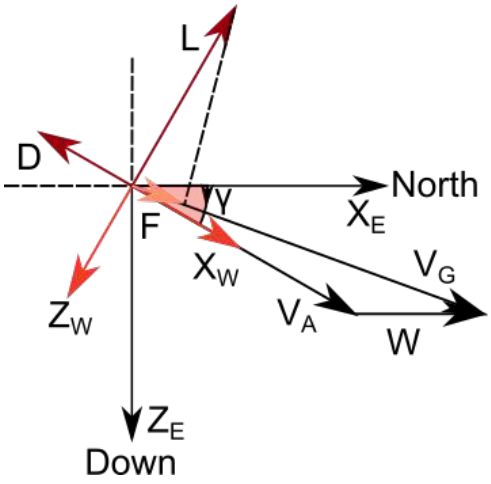

(c) Descent phase.

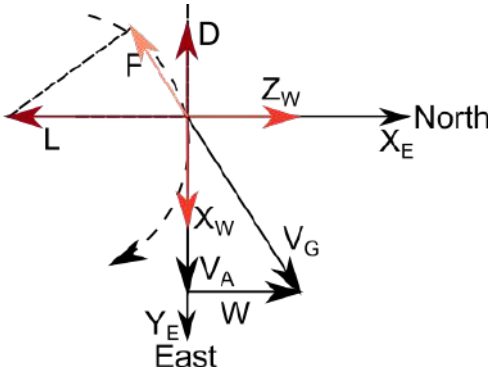

(d) Lower turn phase.

Figure 4.7: Overview of the four phases of dynamic soaring.

Chapter 5

Feasibility of Dynamic Soaring Trajectories

In chapter 4, the attention was focused on how the energy harvesting process of dynamic soaring works. In this chapter, the emphasis will be on how different factors influence the feasibility of dynamic soaring trajectories.

In the first part of this chapter, the metrics used for comparing the different results are presented. Afterwards, the first comparison between trajectories is made. The chapter continues with sets of results obtained by varying the initial airspeed and initial altitude. Finally, the chapter ends with an analysis of the impact of the limit in load factor and lift coefficient on the feasibility of dynamic soaring trajectories.

5.1 Problem Description

The objective now is to find how the wind profile, the initial conditions and vehicle constraints affect dynamic soaring trajectories and the viability of their execution in the real world. To perform this study, only closed, single-loop, energy-neutral dynamic soaring trajectories will be considered, since they represent manoeuvres that an aerial vehicle is expected to perform in a surveillance mission.

The first step is to understand how different wind models change the dynamic soaring manoeuvre. For that, it is necessary to calculate, for the different wind models, the trajectories that minimise the required wind strength. This kind of analysis allows for the comparison of the trajectories' feasibility. Trajectories that require less restrictive wind conditions have higher viability in the real world and can be applied in a broader set of scenarios.

The initial conditions also play a role in defining how viable a manoeuvre is for the existent wind conditions. So, it is also necessary to establish the relation between the initial conditions and the required wind strength. This additional step allows the study of how the initial conditions must be selected in order to make the trajectory feasible.

5.2 Comparison Metrics

To draw comparisons between the trajectories and to understand how the various factors mentioned in section 5.1 affect their feasibility and performance, it is necessary to establish a set of metrics that can be used to compare them.

The various trajectories obtained vary in total time, maximum height attained, overall length, and on the wind strength to which they are subjected. Because of this variety, it is necessary to define different comparison quantities.

Since the focus of the research is to study the feasibility of dynamic soaring trajectories, it is useful to define metrics that consider trajectories that require high wind strengths as inefficient. Trajectories that require higher wind conditions are inefficient since they have a higher dependence on the wind for energy extraction. In addition, trajectories that require higher wind strengths are considered to be less viable, since they need conditions that are more difficult to encounter in the real world. Efficiency and viability are closely related since trajectories that are less efficient are also less viable.

With the previous considerations in mind, the first quantity that can be used to perform comparisons is the difference between the wind speed velocity at the highest point and the lowest point of the trajectory,

$$\Delta W_r = W(h_{max}) - W(h_{min}), \tag{5.1}$$

where h_{max} and h_{min} are the highest and lowest altitudes attained by the UAV during the trajectory respectively. Since the wind gradient with altitude is always positive, it means that the metric compares the maximum and minimum wind speeds to which the vehicle is subjected. This metric indicates how strong the wind needs to be to perform the dynamic soaring manoeuvre. It is then expected that as the value of this parameter increases, the feasibility of the trajectory decreases since it requires higher wind strengths to be performed.

As mentioned, the trajectories vary in space and time depending on the wind they are subjected to, so it is important to define metrics that normalize these variations, making possible the comparison of very different trajectories. Using the concept of real wind speed delta, two new quantities can be defined, a parameter based on the maximum height,

$$\eta_h = \frac{h_{max}}{\Delta W_r t_s}, \tag{5.2}$$

and a parameter based on the trajectory's length,

$$\eta_l = \frac{l}{\Delta W_r t_s}, \tag{5.3}$$

where, t_s is the time spent to perform the full trajectory and l is the total distance travelled. These two new non dimensional quantities relate how fast the UAV has climbed or travelled, respectively, with the strength of the wind required to do so. In other words, they establish a relation between the wind speed required and the net speed of the trajectory, with the net speed being given by $\frac{h_{max}}{t_s}$ or by $\frac{l}{t_s}$.

The set of metrics presented will power the comparison of the various trajectories considered.

5.3 Effect of Different Wind Profiles

It is now of interest to determine, for a given set of initial conditions, how the different wind models presented in section 2.2 affect the efficiency and feasibility of the dynamic soaring trajectories according to the metrics just defined. Seven different profiles are considered, a linear profile, a logarithmic profile, and five step-wind profiles with various characteristics (figures 2.3 and 2.4). In all cases, the vehicle has an initial airspeed of 20m/s and an initial height of 1.5m.

Table 5.1 summarizes the main characteristics of the closed, energy-neutral trajectories that minimise the required wind strength, obtained for the different wind profiles. It also presents the respective values for the metrics previously presented.

Table 5.1: Comparison between dynamic soaring trajectories for different wind profiles, for a initial airspeed of 20m/s and an initial height of 1.5m.

Wind Profile	t_s [s]	h_{max} [m]	l [m]	ΔW_r [m/s]	η_h	η_l
Linear	8.16	17.85	119.26	4.88	0.45	2.99
Logarithmic	11.57	14.82	167.29	5.16	0.25	2.81
Step 1 (k=0.5 and b=5)	7.64	16.26	119.29	3.40	0.63	4.59
Step 2 (k=0.5 and b=10)	7.85	16.00	117.36	3.86	0.53	3.87
Step 3 (k=0.5 and b=15)	9.05	18.28	119.00	6.46	0.31	2.03
Step 4 (k=0.7 and b=5)	7.59	16.31	118.62	3.31	0.65	4.73
Step 5 (k=1.1 and b=5)	7.56	16.27	118.28	3.23	0.67	4.85

Looking at table 5.1, it is possible to conclude that the wind profiles that require the least amount of wind strength, for the given initial conditions, are the step wind profiles with transition height (b of equation (2.18)) equal to 5 and 10 meters. In contrast, the least efficient wind profile is the step wind profile with transition height equal to 15 meters, which requires almost double the wind strength when compared with the other step wind profiles. From table 5.1, it is also possible to conclude that by increasing the steepness k of the step-profile, there is a slight decrease in the required wind strength.

For the initial conditions considered, the linear and logarithmic wind profiles require a higher wind strength than the best step wind profiles, but lower than step 3. The trajectory obtained for the logarithmic wind profile requires the second-largest wind strength for the cases presented and results in a trajectory larger than for any other case.

From table 5.1 it is also possible to verify that, in general, as the required wind strength increases, the time and length of the trajectory also increase.

From the present analysis, emerge some points worth exploring deeper. Firstly, it is necessary to understand why there is such a discrepancy between step-wind profiles with b=5 and b=10 and the b=15 case. The second point worth exploring is the reason behind the increase in efficiency with the increase of steepness of the step-wind profiles. Finally, it is important to explain why the logarithmic wind profile requires high wind strengths to perform dynamic soaring since it is the wind profile expected to find over

the ocean surface, where surveillance missions are likely to occur.

5.3.1 Step-Wind Profiles

Effects of Changing the Transition Height

In order to understand how the transition height affects the efficiency of dynamic soaring trajectories, a comparison between the obtained trajectories for different step-profiles is required. Figure 5.1 presents the evolution of the height, airspeed and wind speed for three step-wind profiles all with k equal to 0.5 and b equal to 5, 10 and 15. Figure 5.2 presents the evolution of the lift and drag power contributions for the same wind profiles.

Since all the three trajectories depart from the same initial point and are all energy-neutral, the initial and final energies are equal for the three cases. Figure 5.2 shows that the main difference between the energy gains for each trajectory is not in the overall quantity of the gains,the case for b=15 extracts only 10% less energy than the b=5 case, but what factor is responsible for the energy extraction.

The trajectory for the step-wind profile with b=15 requires more wind speed than the other two because the vehicle is forced to climb during much more time without the presence of wind, or in other words, without being capable of extracting energy. When it reaches the 15-meter altitude, its airspeed is very small and, consequently, there is a reduction in the quantity of lift available to provide energy, when compared with the other two cases. The result is that to extract the same amount of energy, the only possibility is to have stronger winds (see figure 5.1).

The difference between the b=5 and b=10 is not as significant because the lift depends on the square of the airspeed. So as the airspeed decreases, the energy-extraction decreases with the square of the airspeed difference, which needs to be compensated with increasing wind strength. Since the trajectory for b=15 implies flying with lower airspeeds than for the other two cases, the impact of the transition height becomes more noturious.

Effects of Changing the Step Steepness on Efficiency

Looking at table 5.1, it is possible to verify that the difference between the trajectories obtained for b=0.5 and k=0.5, 0.7 and 1.1, is slender and the required wind strength only decreases by 0.2m/s with the increase of the steepness. Figure 5.3 also confirms the similarity between trajectories. Nevertheless, the reason behind the reduction in wind strength required is worth exploring, since any reduction in the minimum wind strength required is welcomed.

Figure 5.4 presents the lift and drag contributions for the three cases. The graph shows that the drag contribution is similar for the three cases; this is due to the fact that the airspeed and lift coefficient evolve similarly in the three cases. In what concerns the lift contributions, it is possible to verify that for the case in which k=0.5, there are higher losses during the lower turn than for the other cases. These losses will need to be compensated during the remaining phases of the flight, which can only be obtained through the presence of a stronger wind.

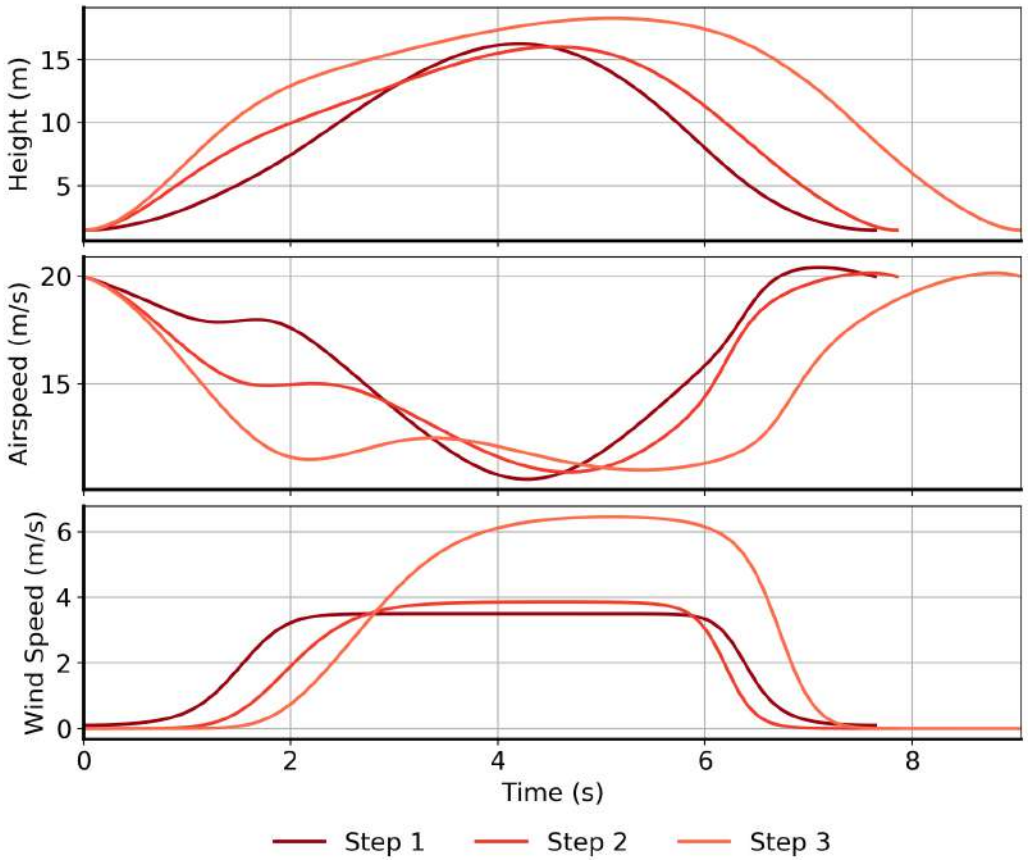

Figure 5.1: Comparison between energy-neutral trajectories for step-wind conditions with different transition heights.

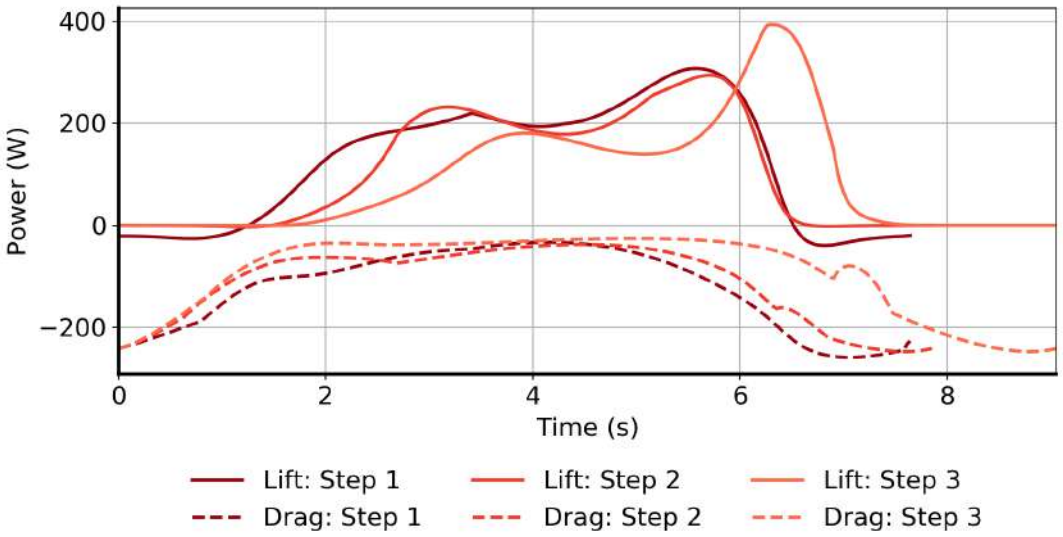

Figure 5.2: Evolution of energy gains and losses, for step-wind conditions with different transition heights.

In the lower turn, the increasing negative lift contribution with decreasing wind steepness is the result of the presence of wind that, as the steepness decreases, increases in intensity. Figure 5.3 shows just that. It is then possible to conclude that the presence of wind speed in the lower turn reduces the efficiency of the trajectory.

Since all trajectories only vary slightly, in the remainder of the present discussion, step-wind profiles 4 and 5 will not be considered.

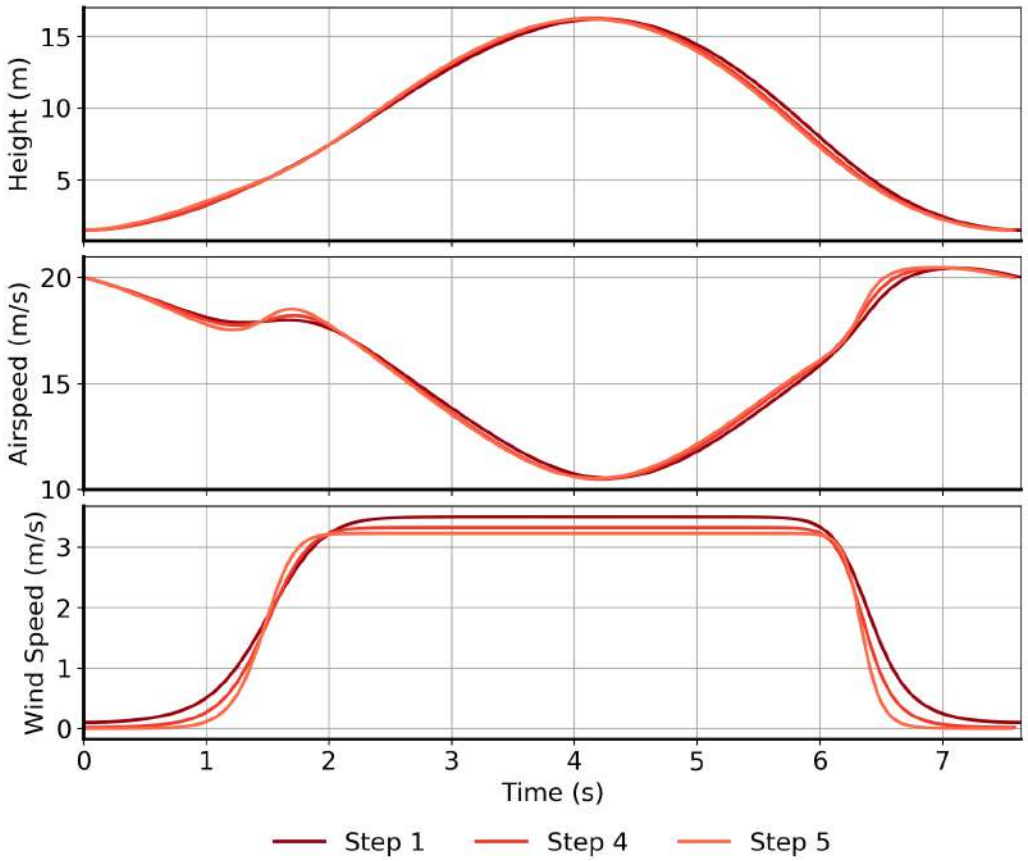

Figure 5.3: Comparison between energy-neutral trajectories for step-wind conditions with different steepness. Notice how in the step 1 case the wind in the lower turn is slightly larger than in the other two cases.

5.3.2 Logarithmic Wind Profile

To understand why the logarithmic wind profile is one of the worst-performing wind profiles for dynamic soaring it is necessary to analyse how the rate of change of energy of the system evolves in time, and how it compares with the other cases.

Figure 5.5 presents the evolution of the main variables associated with the optimal dynamic soaring trajectory for the logarithmic wind profile. Looking at figure 5.5, it is possible to see that in the lower turn the rate of energy loss is four times higher than for the linear case presented in chapter 4 and much higher than in the case of the step wind profiles, just presented. Such difference is due to the fact that

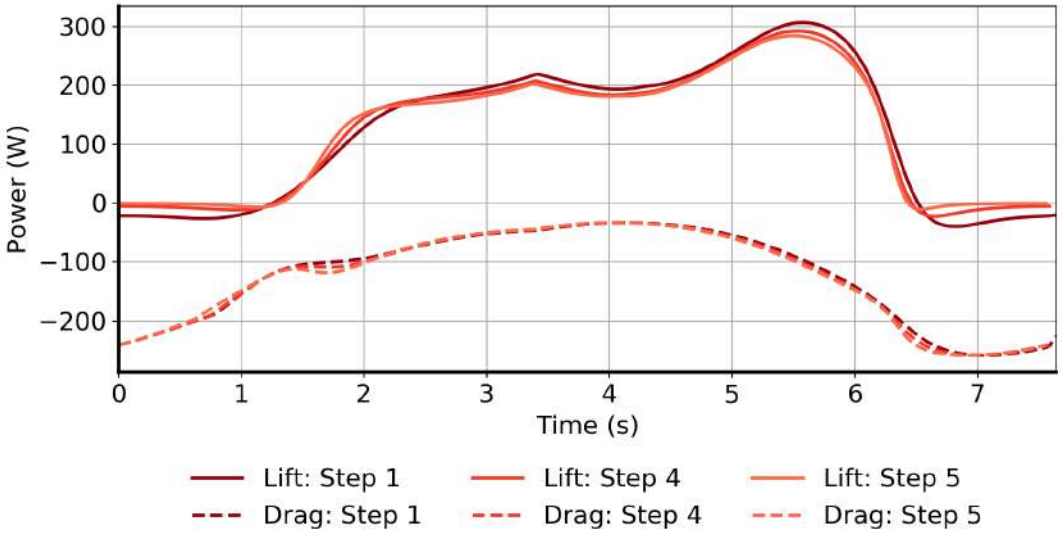

Figure 5.4: Evolution of energy gains and losses, for step-wind conditions with different steepness. Notice how in the step 1 case the lift contribution in the lower turn is slightly larger than in the other two cases.

in the case of the logarithmic wind profile, there is considerably stronger wind during the lower turn, approximately 4.5 m/s, compared with the near 0m/s found in step-wind profiles.

Just has it happened for the decrease in steepness in step-wind profiles, the larger wind present in the lower turn increases the losses due to the lift. The higher energy loss in the lower turn must be compensated during the other phases of the flight. Since the initial conditions remain the same, the only solution is to increase the wind strength present at higher altitudes substantially. The result is one of the highest wind deltas for the set of wind profiles being considered.

Notice how the lower turn occurs at the minimum height possible to ensure the least amount of wind possible during the lower turn, in order to minimise the losses during this phase.

It seems that, from the analysis made, two aspects affect the value of the minimum wind strength required to perform the trajectories. Firstly, it became apparent that the initial conditions of the vehicle impact its ability to extract energy from the present wind profile, as it had also happen in the case of the step profiles with different transition heights. Secondly, it seems that the existence of wind in the lower turn substantially increases the necessary wind strength, since it increases the losses of the vehicle. With these two aspects in mind, the next section will be interested in studying how the initial conditions of the vehicle influence the efficiency of the trajectories for the various wind profiles.

5.4 Effect of Different Initial Conditions

All the results presented until now considered the same set of initial conditions (Initial airspeed of 20m/s and initial height of 1.5m). From the previous discussion, it seems reasonable to assume that, by changing the initial conditions of the vehicle, the efficiency attributed to each wind profile may change. If the conditions are not the most suitable, then the vehicle cannot extract the highest amount of energy

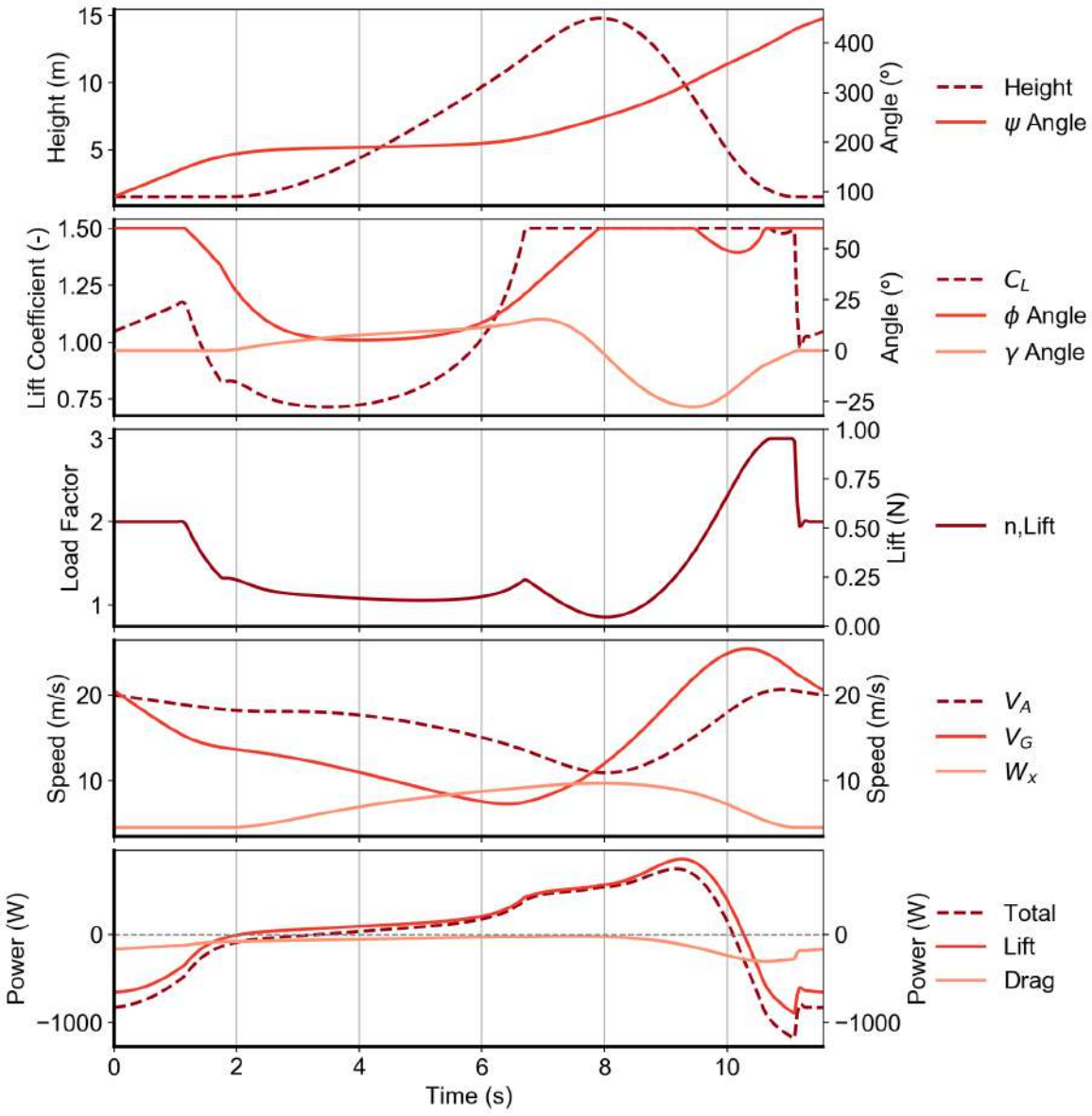

Figure 5.5: Detailed evolution of the principal parameters of the optimal trajectory that minimises the wind strength required for a logarithmic wind profile. The first panel presents the evolution of the altitude and heading angle with time. The second panel presents the evolution of the control variables and the flight path angle. The third panel presents the evolution of the lift and load factor with time (the lines are coincident). The fourth panel presents the evolution of the ground speed, airspeed and wind speed throughout the trajectory. Finally, the last panel presents the evolution of the lift and drag contributions for the variation of the mechanical energy, as well as the overall variation of the power.

from the profile and the feasibility of the trajectory may be compromised.

When analysing the initial conditions of the UAV (table 3.2), its the altitude and airspeed of the UAV

that seem to be the two variables which possibly most impact the performance of the trajectory.

5.4.1 Initial Altitude

Starting by analysing the effect of changing the initial heigh of the vehicle, table 5.2 summarises the results obtained for different wind profiles for a new initial height of 6.5 meters.

Table 5.2: Comparison between dynamic soaring trajectories for different wind profiles. For an initial airspeed of 20m/s and initial height of 6.5m.

Wind Profile	t_s[s]	h_{max}[m]	l[m]	ΔW_r[m/s]	η_h	η_l
Linear	8.78	21.04	126.00	5.06	0.47	2.84
Logarithmic	-	-	-	-	-	-
Step 1 (k=0.5 and b=5)	10.77	18.71	177.70	4.67	0.37	3.54
Step 2 (k=0.5 and b=10)	7.56	19.39	117.24	3.43	0.75	4.53
Step 3 (k=0.5 and b=15)	8.14	19.87	118.77	4.32	0.56	3.37

From the obtained results and comparing with the results of table 5.1, it is possible to conclude that increasing the initial height increased the wind strength required for the cases of the linear and step 1 wind profiles. For the cases of steps 2 and 3, there is a decrease in the required wind strength. Table 5.2 also indicates that for this set of initial conditions, there is not a feasible single-loop, energy-neutral trajectory for the logarithmic wind profile.

The reduction of efficiency (increase of the required wind strength) associated with the linear and step 1 wind profiles, is due to the fact that the new initial height does not correspond to the height of least wind strength. The result is the lower turn being performed in less efficient conditions, with higher losses occurring.

The trajectories for step-wind profiles 2 and 3 have their efficiencies increased, since, in these new conditions, the vehicle has to climb less to reach the altitude where the wind is present. In fact, the increase of the initial height by 5 meters is equivalent to decreasing the transition height in the same amount. Comparing the results of table 5.2 with the ones of the previous case (table 5.1), it is possible to verify that the trajectory for step 2 for the new initial height is similar to the one of step 1 for the previous initial altitude, the only difference the maximum height attained.

The particular case of the logarithmic profile can be explained from the fact that there is not a way of ensuring a wind speed delta high enough to perform dynamic soaring, given the overall shape of the wind profile. The variation of the initial height increases the wind speed the vehicle is subjected to in the lower turn and, given the shape of the profile, it is not possible to offset this increase with a larger wind strength at higher altitudes.

From the analysis presented until now, it seems that, for each wind profile, there is an ideal initial height that minimises the wind strength required for dynamic soaring. Figure 5.6 presents the evolution of the required wind strength as a function of the initial height for the case of the step 2 wind profile (transition height at 10 meters).

Looking at figure 5.6, it is possible to verify that there is an initial height that minimises the wind

Figure 5.6: Evolution of the required wind strength as a function of the initial height for a step-wind profile with b=10 and k=0.5.

strength required. The optimal altitude is around 6.5 meters. This behaviour is the result of two phenomena. Firstly, when the initial height is lower than the optimal value, the vehicle is forced to climb and descend without extracting energy during most of the time. Secondly, if the initial height is increased beyond the optimal value, it means that the lower turn will occur in the presence of higher wind speeds, which increases the losses of the vehicle. From the graph, it is also possible to conclude that, from the two phenomena, it is the presence of wind speed in the lower turn that most negatively contributes to thee loss of efficiency and, consequently to the loss of viability.

5.4.2 Initial Airspeed

Analysed the influence of the initial height, the attention will be now turned to the effect of the initial airspeed. Table 5.3 presents the summary of the trajectories obtained by varying the initial airspeed of the vehicle for the case of the linear wind profile.

Table 5.3: Comparison between dynamic soaring trajectories for different initial airspeeds for the case of a linear wind profile.

V_{A_0} [m/s]	t_s[s]	h_{max}[m]	l[m]	ΔW_r[m/s]	η_h	η_l
15,00	11,38	10,66	135,13	7,05	0,13	1,68
17,50	9,19	13,47	126,23	5,24	0,28	2,62
20,00	8,16	17,85	119,26	4,88	0,45	2,99
22,50	8,89	23,09	138,31	5,31	0,49	2,93
25,00	10,26	28,75	170,22	6,10	0,46	2,72
30,00	13,42	42,15	244,60	8,66	0,36	2,11

Looking at table 5.3, it is possible to verify that, there is an initial airspeed that minimises the real wind speed delta necessary to perform the trajectory. For the present case, the optimal initial airspeed is around 20m/s. It is also possible to verify that, as the initial airspeed increases, the maximum height attained by the vehicle also increases. Since the vehicle has more airspeed to exchange for altitude, it will climb more, in order to extract the maximum amount of energy possible. Nevertheless, this alone does not explain the existence of a minimum initial airspeed or the reason for a decrease or increase in

the initial airspeed to cause a loss of efficiency.

The behaviour of the step-wind profiles is similar to the one presented for the linear case. Figure 5.7 presents the evolution of the real wind speed delta as a function of the initial airspeed for the case of step 1, 2 and 3, all with k = 0.5 and for each of the transition heights.

Analysing figure 5.7, it is possible to see that there is an initial airspeed that minimises the required wind strength. In addition, it is possible to see that depending on the initial airspeed, the most efficient step-wind profile changes. As expected, the step with the lowest transition height is the most efficient profile for low airspeeds, while the profiles with higher transitions heights are better for higher initial airspeeds.

A couple of factors can explain the behaviour verified for the four cases presented. At lower than optimal initial airspeeds, the increase of the required wind strength is the result of a decrease in the capacity of the vehicle to extract energy. The lift depends on the square of the airspeed so at lower airspeeds the contribution of the lift to the energy reduced. In addition, for step-wind profiles with high transition heights, there are not feasible trajectories for low initial airspeeds since the vehicle does not have sufficient initial airspeed to trade in order to reach the transition height.

In contrast, at higher than optimal initial airspeeds, the increase of the minimum wind strength can be explained based on two factors. On the one hand, although the energy extraction increases with the airspeed, so does the drag, resulting in need of higher wind speeds. On the other hand, the limitation imposed by the maximum load factor admissible, limits the maximum airspeed and turn rate of the vehicle can reach, resulting in less efficient trajectories.

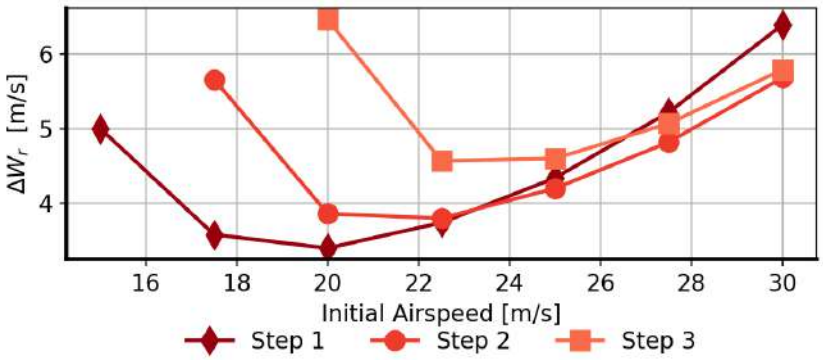

Figure 5.7: Evolution of the required wind strength as a function of the initial airspeed for three different step-wind profiles with b=5,10 and 15, and k=0.5.

Figures 5.6 and 5.7 can be interpreted as the boundary between the infeasible region of energy-neutral dynamic soaring trajectories and the region where there is excess wind when compared with the minimum case.

Looking at figure 5.7, it is possible to see that when in the presence of a step-wind profile with transition height at 10 meters and wind strength of 4.5m/s, and for an initial height of 1.5 meters, there are a couple options from the trajectory point of view: it is possible to obtain a energy-neutral trajectory with initial airspeeds of 19m/s or 27m/s; have a initial airspeed between this two values, and be in the

excess wind region, utilizing the excess energy to accelerate the vehicle, climb or perform energy-neutral trajectories with different characteristics.

5.5 Effect of Vehicle Constraints

From the previous discussion regarding the variation of the performance with the initial airspeed, it was possible to verify that the maximum lift coefficient and maximum load factor influence the feasibility of dynamic soaring manoeuvres for cases of low and high initial airspeed, respectively. This section is concerned with finding how these two constraints associated with the intrinsic characteristics of the UAV influence the dynamic soaring capabilities of the vehicle.

In order to understand how these constraints affect the obtained trajectories, two different trajectories will be compared. In both cases, the vehicle is subjected to a linear wind profile and the trajectories obtained are closed, energy-neutral and minimise the wind strength required. The only difference is that in one the maximum lift coefficient allowed is 1.5 (trajectory of chapter 4), and in the other is 2.0.

Figure 5.8 presents a comparison of the two trajectories being considered. Looking at the results, it is possible to verify that the two trajectories are similar. The case for which the maximum lift coefficient is 2.0 can attain a higher altitude and can fly at lower airspeeds, which are direct consequences of the higher lift coefficient. Besides that, the higher lift coefficient case requires a marginally gentler slope wind slope 0.28, compared with 0.30 of the other case. So it is possible to conclude that for the case of the linear wind profile, with the considered initial conditions, the change in maximum lift coefficient does not change the overall dynamic soaring trajectory significantly.

Nevertheless, in what concerns the lift coefficient control, it is possible to verify very different behaviour between the two cases. For the case of $C_{L_{Max}} = 1.5$, the vehicle spends most of the time in the limit, decreasing only in the climb in order to maintain a constant flight path angle. On the contrary, it is possible to verify for the case of $C_{L_{Max}} = 2$ that lift coefficient varies more during the trajectory. In the lower turn, the lift coefficient decreases as a response to having reached maximum value for the load factor allowed, which does not happen in the other case. Since the velocity is still increasing the lift coefficient is forced to decrease in other to not exceed the load factor limit. It is also possible to verify that in the upper-turn and start of the descent, the C_L is in maximum value allowed, in order to maximize the energy extraction.

From this analysis, it is possible to verify that when the $C_{L_{Max}}$ is low, it is the C_L that limits the feasibility and performance of the trajectories. On the contrary, when $C_{L_{Max}}$ is high, then it is the load factor that limits the feasibility and performance that can be extracted. Moreover, depending on the initial airspeed one factor maybe of higher importance than the other. Figure 5.9 help illustrate this point, it presents the evolution of the required wind strength as a function of the initial airspeed, for different vehicle constraints, and for the case of the step 2 wind profile.

Looking at figure 5.9 it is possible to verify that, on the one hand, at lower initial airspeeds, it is possible to obtain more efficient trajectories (trajectories that require less wind strength), by having a larger value of the maximum lift coefficient, while at higher airspeeds the maximum lift coefficient does

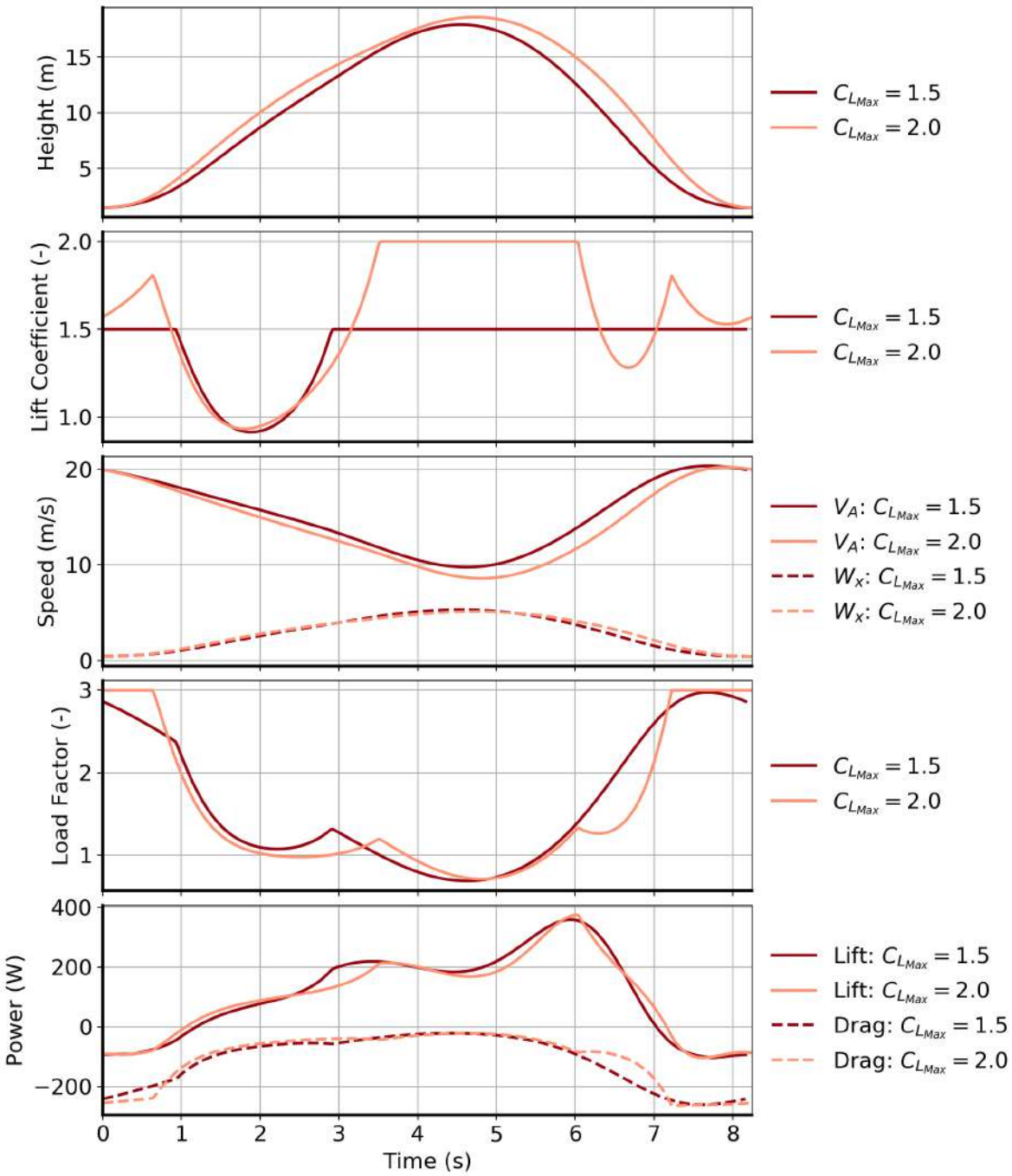

Figure 5.8: Comparison between trajectories obtained, for a linear wind profile, by varying the maximum lift coefficient available. The red lines are for the case $C_{L_{Max}} = 1.5$ and the orange lines for $C_{L_{Max}} = 2.0$.

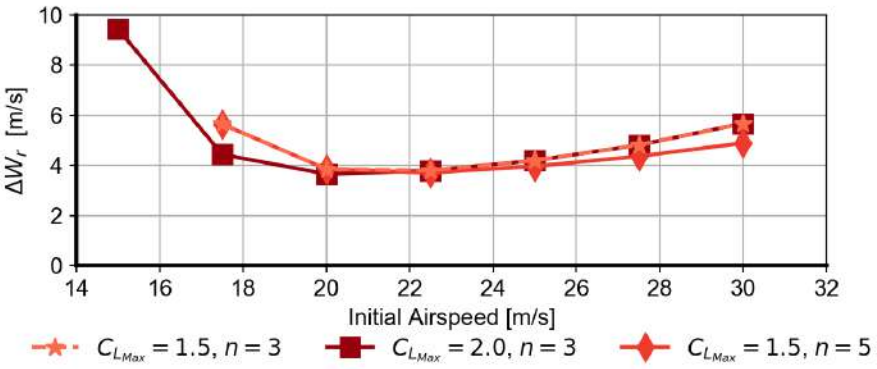

Figure 5.9: Evolution of the required wind strength as a function of the initial airspeed, for different vehicle constraints, and for the case of the step 2 wind profile.

not contribute to any changes. On the other hand, by having a larger maximum load factor, at higher initial airspeeds it is possible to obtain more efficient trajectories, while at lower airspeeds it does not change the performance. The reason behind this phenomenon is due to the fact that at higher airspeeds the load factor is the main constraint, while at lower airspeeds it is the lift coefficient.

In addition, it is possible to verify that the maximum lift coefficient and the maximum load factor change the feasibility region. For instance, for an initial airspeed of 15m/s and a step-wind profile with transition height at 10 meters, there is not a feasible trajectory when the maximum lift coefficient is 1.5. On the contrary, if the maximum lift coefficient is 2.0, then it is possible to find a feasible trajectory. Table 5.4 summarizes the characteristics of this new trajectory.

Table 5.4: Summary of characteristics of the new feasible trajectory obtained by increasing the maximum lift coefficient.

t_s[s]	h_{max}[m]	l[m]	ΔW_r[m/s]	η_h	η_l
12.16	11.67	98.77	5.61	0,17	1.45

The new trajectory does not have the best performance, since the vehicle still has to climb most of the time without being able to extract energy but, if the wind conditions allow and desired, it is possible to execute the manoeuvre. The increase of the maximum lift coefficient has this added advantage, it increases the number of manoeuvres the vehicle can perform.

Chapter 6

Trajectories for Surveillance Applications

In the previous chapter, the focus was on the various aspects that affect the feasibility of dynamic soaring trajectories. In this chapter, the focus will be turned to the study of trajectories that can be used in surveillance applications when the wind conditions are favourable.

This chapter starts by presenting the new objective functions that will be used to obtain the surveillance trajectories. Afterwards, the obtained trajectories are analysed. At the end of the chapter, an overview of other possible approaches is made.

6.1 Problem Description

Until now, all trajectories considered were obtained with the objective of minimising the necessary wind strength required, meaning that they represent an application limit case. The question that this chapter tries to answer is what can be done when the wind strength is higher than the minimum case.

The aim is to find trajectories that can be used for surveillance missions. Thus, the obtained trajectories must be closed, single-loop and energy-neutral, in order to have trajectories with simple control schemes (the UAV can only bank to one side), and that are endlessly repeatable in constant wind conditions. For ease of analysis, all trajectories obtained will be for a step wind profile with transition height at 5m and steepness of 0.5.

6.2 Objective Functions

The objective functions utilized until now tried to minimise the wind strength required to perform dynamic soaring trajectories. To obtain surveillance trajectories in excess wind conditions, the objective function used must change.

Since the interest is on developing trajectories for surveillance missions, there are two characteristics of the trajectory that should be optimized: the trajectory time and length. By maximizing the flight time

of the single-loop trajectory, more time is spent observing the target of interest, while by maximizing the length the surveillance area is increased.

Based on these considerations, two objective functions were developed, the first is to maximize the final time of the trajectory,

$$\max\ t_f, \tag{6.1}$$

by maximizing this parameter, the overall trajectory time is maximized. The other objective function is

$$\max \int_{t_0}^{t_f} \sqrt{(x_0 - x(t))^2 + (y_0 - y(t))^2} dt, \tag{6.2}$$

meaning that at each instant, the distance between the starting point and the vehicle position is maximized. By maximizing this objective function, the length of the trajectory is also maximized.

To ensure that the obtained trajectories are single-loop, the vehicle is only allowed to bank to the right.

6.3 Surveillance Trajectories

Figures 6.1 and 6.2 present the trajectory that maximizes the flight time of the closed, single-loop, energy-neutral trajectory for a step-wind profile with b=5 and k=0.5, and with a maximum wind strength (A of eq. (2.18)) equal to 5m/s.

From figures 6.1 and 6.2, it is possible to verify that the behaviour of the vehicle during the manoeuvre has changed when compared with the previous cases studied. The trajectory obtained is still a simple single-loop closed trajectory, but after the initial climb, there is a small descent into the wind, that generates a loss of energy. Afterwards, the upper turn occurs at almost constant height, followed by the descent and the lower turn.

The new behaviour for the trajectory can be explained by the fact that for having an energy-neutral trajectory in excess wind conditions, it is necessary to waste the additional energy gained due to the stronger wind speed. Since the objective is to increase the flight time, the solution is to waste the excess energy in a way that the trajectory time increases. The small descent into the wind, combined with the longer upper turn, allows for such an overall increase of the trajectory time.

A similar reasoning can be made for trajectories in which the objective is to increase the overall trajectory length. Figures 6.3 and 6.4 present the overall evolution of the maximum flight time and trajectory length possible as a function of the available wind strength, for the cases in which the objective is to maximize trajectory time and trajectory length.

Starting with an overall look at both graphs, it is possible to verify that both objective functions are correlated since there is not a significant departure between the results obtained using them. Nonetheless, as the available wind strength increases, the results start to diverge. The reason behind this tendency is the fact that, with more energy-extraction available, the time and length trajectories start to diverge since different solution can be applied.

Looking now at figure 6.3, it is possible to verify that doubling the existent wind speed results in a

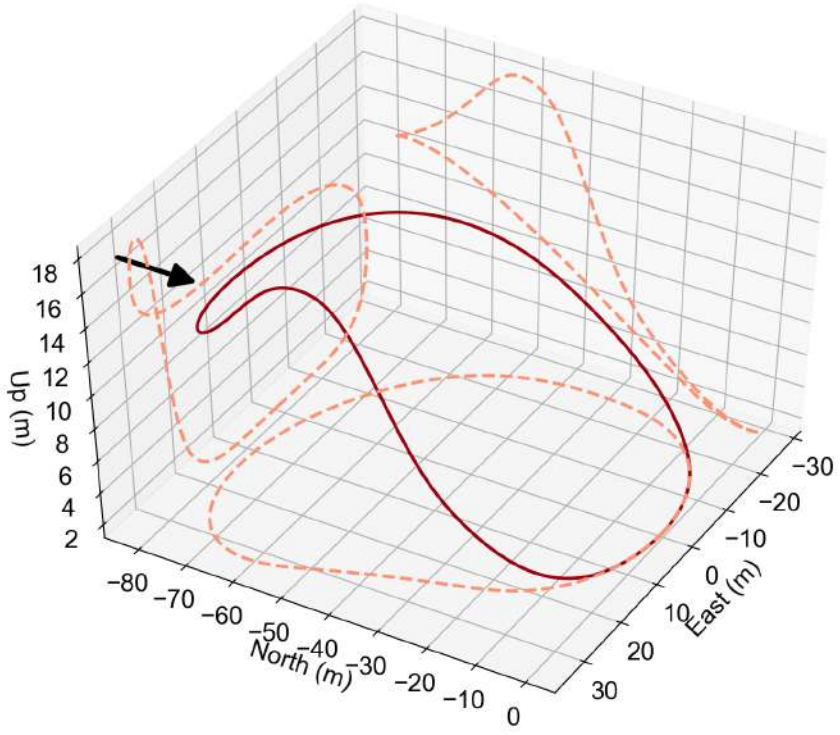

Figure 6.1: Optimal single-loop, energy-neutral trajectory that maximizes the time aloft. Arrow indicates the wind direction. The dashed lines represent the trajectory projections, on each of the three planes. The vehicle travels in the clock-wise direction.

doubling of the maximum trajectory length. Similarly, looking at figure 6.4, a doubling of the existent wind speed also doubles the time spent aloft.

6.4 Other Trajectories

All the trajectories considered until now have been closed, single-loop and energy-neutral. These trajectories are promising from the surveillance application point of view, since they are infinitely repeatable and have a simpler control scheme than other dynamic soaring trajectories.

There are other alternatives to use excess wind conditions beyond those considered in this chapter, that result in non-energy-neutral trajectories. For instance, it is possible to use the increased energy-extraction to increase the final airspeed or height of the vehicle (figure 6.5), in each loop. In other words, in excess wind conditions, it is possible to climb or accelerate without expenditure of energy.

It is also possible to use open dynamic soaring trajectories for surveillance missions; the only requirement is that the excess energy-gained in comparison with the energy-neutral case, is enough to perform the turn that closes the trajectory.

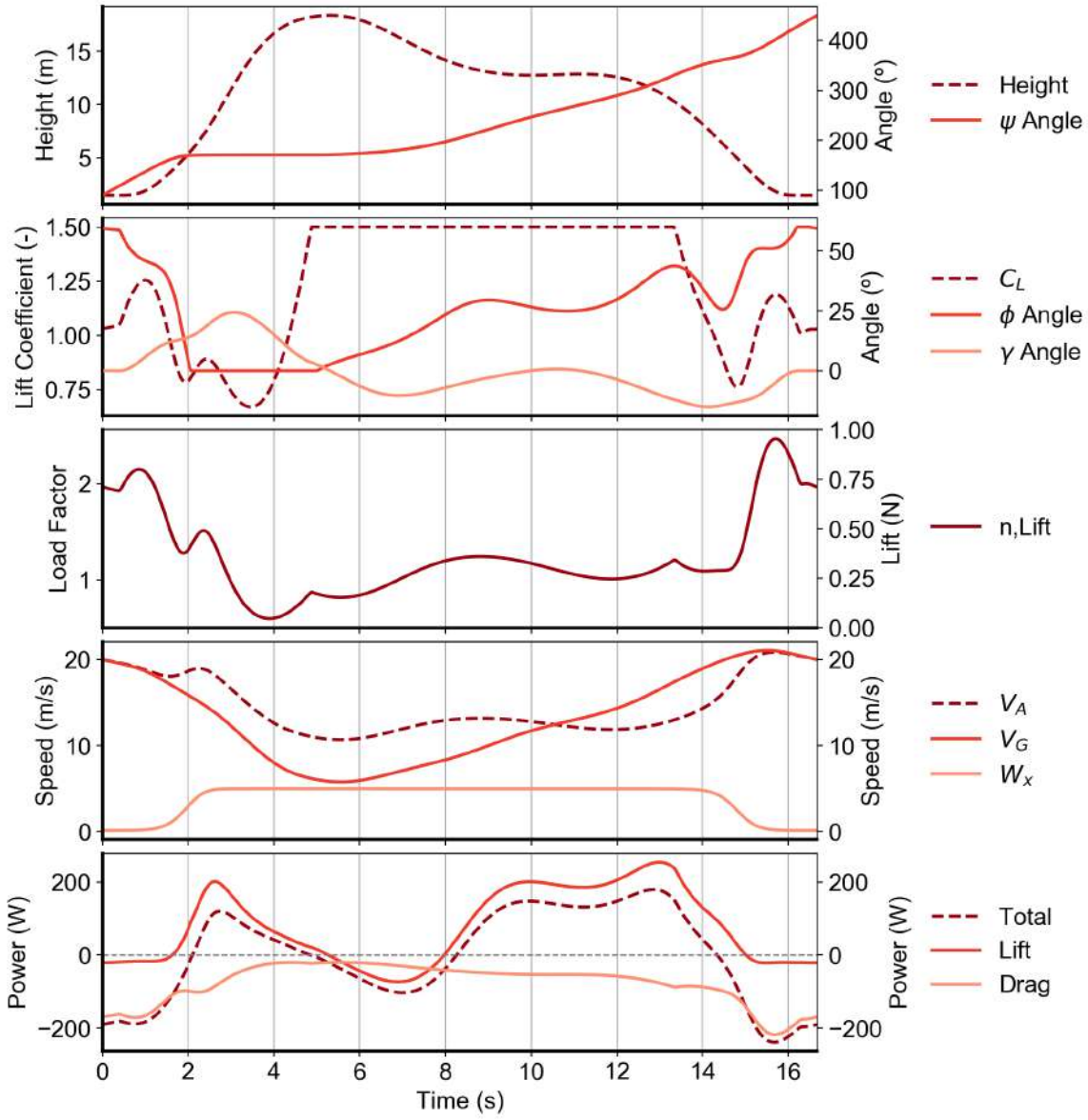

Figure 6.2: Detailed evolution of the principal parameters of the optimal trajectory Evolution of the trajectory that maximizes flight time for a surveillance mission. The first panel presents the evolution of the altitude and heading angle with time. The second panel presents the evolution of the control variables and of the flight path angle. The third panel presents the evolution of the lift and load factor with time (the lines are coincident). The fourth panel presents the evolution of the ground speed, airspeed and wind speed throughout the trajectory. Finally, the last panel presents the evolution of the lift and drag contributions for the variation of the mechanical energy, as well as the overall variation of the power.

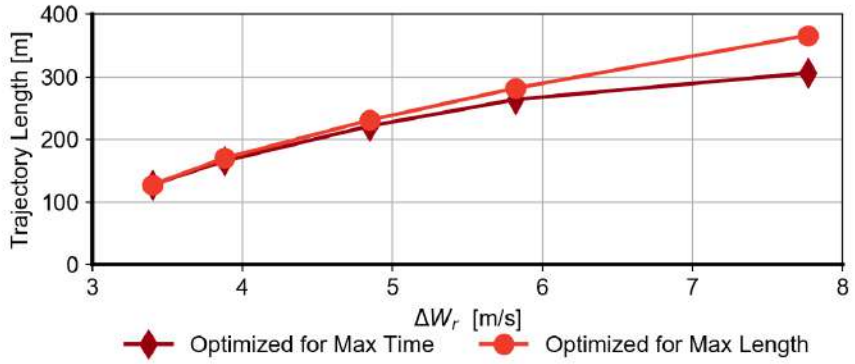

Figure 6.3: Evolution of the maximum trajectory length possible as a function of the available wind strength.

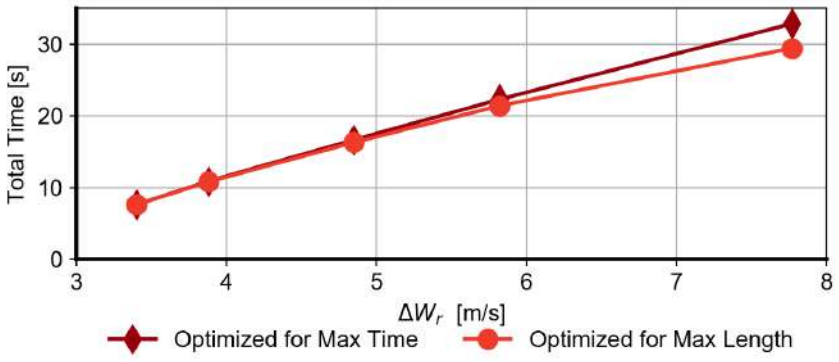

Figure 6.4: Evolution of the maximum trajectory flight time possible as a function of the available wind strength.

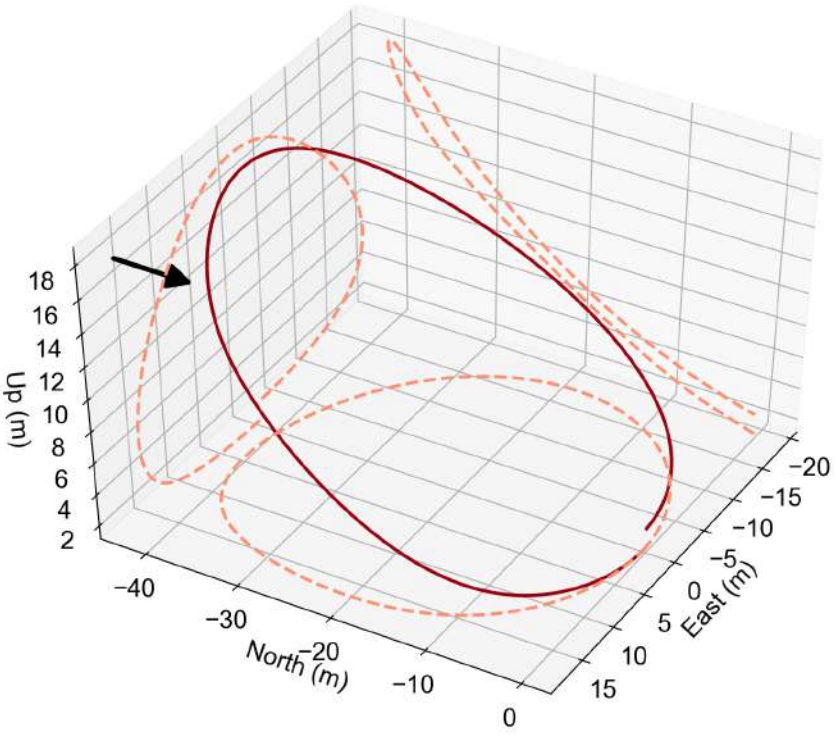

Figure 6.5: Example of dynamic soaring trajectory with altitude gain of 1 meter at the end of one loop and without loss of kinetic energy.

Chapter 7

Conclusions

This chapter starts by summarising the main conclusions that have been progressively presented throughout the text. Afterwards, the main achievements of the performed research are presented, as well as some proposals for possible future research paths linked to dynamic soaring and its real-world application.

At the beginning of the research and with the development of the UAV model, it was possible to fully understand how the Equations of motion typically used in dynamic soaring research are derived. The advantages and disadvantages of the two main reference frames utilised were discussed, from the motion and energy point of views. It was possible to verify that the flight path frame is more intuitive from a motion point of view, while the earth frame is more natural for the energy considerations.

Afterwards, a complete analysis of the optimisation methods that can be used for trajectory optimisation was performed, discussing the various possible approaches. In the end, the interior-point method using a trapezoidal-rule transcription was selected due to its robustness and high compatibility with the desired study and smaller computational load.

With the groundwork completed, it was possible to analyse the dynamic soaring phenomenon. Since one of the main objectives was to obtain trajectories for surveillance missions, all the trajectories considered were closed, single-loop, and energy-neutral. From the study of the energy-harvesting mechanism of dynamic soaring, it was possible to conclude that two variables condition the energy-harvesting: the lift-drag ratio and the existent wind speed. In addition, it was also possible to conclude that the need for a wind profile with a positive gradient in the height direction is due to the fact that, to perform dynamic soaring manoeuvres it is necessary to have a maximisation of the energy extractions on the top of the trajectory and a minimisation of the losses on the lower part.

The feasibility of dynamic soaring trajectories was also studied. It was seen that factors such as the initial airspeed and height change the required minimum wind strength for dynamic soaring, in different wind models. It was possible to conclude that there are optimal values for the initial conditions of the vehicle that minimise the required wind strength. In addition, it was possible to establish, curves that establish the frontier between the infeasibility region and the excess wind energy region were also obtained. Finally, it was also possible to conclude that the aerodynamic and structural limits of the vehicle,

in the form of the maximum lift coefficient and load factor, influence the feasibility region of dynamic soaring, and that, in general, one of this two factors will limit the performance of the dynamic soaring trajectory.

Finally, the present research was able to develop trajectories specially designed for surveillance missions, utilising the lessons learned with the previous work. When excess wind conditions exist, it is possible to utilise the excess energy to extend the time aloft or the length of the trajectory. It was seen that doubling the wind speed delta lead to doubling the trajectories length or time aloft. In addition, it was also possible to see that the trajectories optimised for maximum time and maximum length do not vary significantly between each other; the differences only become accentuated with the increase in available wind speed.

To the best knowledge of the author, the last two points constitute a new approach to the study of the feasibility of dynamic soaring and of its application and hopes it will enhance the discussion of this phenomenon.

7.1 Achievements

The present thesis achieved all the proposed objectives:

- Delivered an understanding of the UAV model, complementing the work done by previous authors;
- Developed a robust computational method for obtaining dynamic soaring trajectories, utilising existent software;
- Enhanced the comprehension of the dynamic soaring phenomenon through a detailed study of each flight phase;
- Proposed ways to increase the feasibility for real applications, through the study of how different factors influence the required wind to perform the trajectories;
- Obtained and described specially designed trajectories for surveillance missions.

7.2 Future Work

The application of dynamic soaring manoeuvres to aerial vehicles has still a long path to take before it can be reliably implemented as a form of increasing endurance time of UAVs.

It is still necessary to develop controllers that, taking into account the wind conditions and the flight conditions, can determine the viability of dynamic soaring manoeuvres, and compute the optimal trajectory to be used. The development of these controllers in the future may use as a starting point the results of the present research.

Another area that must be further explored is the determination of the conditions in which dynamic soaring may be used to minimise energy losses, or in other words, in what situations can dynamic

soaring be used in sub-optimal conditions (when energy-neutral trajectories are not possible), in order to reduce the thrust required to travel.

The study of how to decrease even-further the minimum wind-strength required for dynamic soaring is also an area that should be further researched, in pair with the research of how to maximise the energy extraction when excess wind conditions are present. The last part closely related to the study of non-neutral trajectories briefly mentioned in chapter 6, and that should be further studied.

Finally, it may also be of interest to make a similar study to the one performed in this thesis, but using a more detailed UAV model, in which the inertia terms and side forces acting on the vehicle are considered.

Bibliography

[1] R. Austin. *Unmanned air vehicles UAV design, development, and deployment*. Wiley, 2010. ISBN:0470058196.

[2] J. Wilson. Worldwide UAV roundup 2013. *Aerosapce America*, pages 26–36, July/August 2013.

[3] Boeing. Boeing: Phantom eye. URL `https://www.boeing.com/defense/phantom-eye/`. [Online. Accessed 21st August 2019].

[4] E. Systems. Hermes-900, 2016. URL `https://elbitsystems.com/product/hermes-900-5/`. [Online. Accessed 21st August 2019].

[5] Leonardo. Falco. URL `https://www.leonardocompany.com/en/products/falco`. [Online. Accessed 21st August 2019].

[6] Tekever. Tekever AR3, . URL `http://airray.tekever.com/ar3/`. [Online. Accessed 21st August 2019].

[7] Tekever. Tekever AR4, . URL `http://uas.tekever.com/ar4-evo/`. [Online. Accessed 21st August 2019].

[8] J. M. Grasmeyer and M. T. Keennon. Development of the black widow micro air vehicle. *Fixed and Flapping Wing Aerodynamics for Micro Air Vehicle Applications*, page 519–535, 2001. doi: 10.2514/5.9781600866654.0519.0535.

[9] K. Anderson and K. J. Gaston. Lightweight unmanned aerial vehicles will revolutionize spatial ecology. *Frontiers in Ecology and the Environment*, 11(3):138–146, 2013. doi: 10.1890/120150.

[10] R. Szabolcsi. UAV operator training – beyond minimum standards. *Scientific Research And Education In The Air Force*, 18(1):193–198, 2016. doi: 10.19062/2247-3173.2016.18.1.25.

[11] P. Oettershagen, A. Melzer, T. Mantel, K. Rudin, R. Lotz, D. Siebenmann, S. Leutenegger, K. Alexis, and R. Siegwart. A solar-powered hand-launchable UAV for low-altitude multi-day continuous flight. *2015 IEEE International Conference on Robotics and Automation (ICRA)*, 2015. doi: 10.1109/icra.2015.7139756.

[12] M. Bronz, J. M. Moschetta, P. Brisset, and M. Gorraz. Towards a long endurance MAV. *International Journal of Micro Air Vehicles*, 1(4):241–254, 2009. doi: 10.1260/175682909790291483.

[13] K. Kim, T. Kim, K. Lee, and S. Kwon. Fuel cell system with sodium borohydride as hydrogen source for unmanned aerial vehicles. *Journal of Power Sources*, 196(21):9069–9075, 2011. doi: 10.1016/j.jpowsour.2011.01.038.

[14] T. Chang and H. Yu. Improving electric powered UAVs' endurance by incorporating battery dumping concept. *Procedia Engineering*, 99:168–179, 2015. doi: 10.1016/j.proeng.2014.12.522.

[15] C. Gao. *Autonomous soaring and surveillance in wind fields with an unmanned aerial vehicle*. PhD thesis, University of Toronto, Canada, 2015.

[16] G. P. Sachs. Minimum shear wind strength required for dynamic soaring of albatrosses. *Ibis*, 147 (1):1–10, Dec 2004. doi: 10.1111/j.1474-919x.2004.00295.x.

[17] J. H. Koessler. Towards the unification of static and dynamic soaring. *AIAA Scitech 2019 Forum, San Diego, USA*, Jan 2019. doi: 10.2514/6.2019-0266.

[18] G. P. Sachs. Dynamic soaring at 600 mph. *AIAA Scitech 2019 Forum, San Diego, USA*, Jan 2019. doi: 10.2514/6.2019-0107.

[19] Rayleigh. The soaring of birds. *Nature*, 27(701):534–535, 1883. doi: 10.1038/027534a0.

[20] P. Idrac. Experimental study of the "soaring" of albatrosses. *Nature*, 115(2893):532–532, 1925. doi: 10.1038/115532a0.

[21] S. L. Walkden. Experimental study of the "soaring" of albatrosses. *Nature*, 116(2908):132–134, 1925. doi: 10.1038/116132b0.

[22] C. J. Pennycuick. Soaring behaviour and performance of some east african birds, observed from a motor-glider. *Ibis*, 114(2):178–218, 1971. doi: 10.1111/j.1474-919x.1972.tb02603.x.

[23] C. J. Pennycuick. The flight of petrels and albatrosses (procellariiformes), observed in south georgia and its vicinity. *Philosophical Transactions of the Royal Society B: Biological Sciences*, 300(1098): 75–106, 1982. doi: 10.1098/rstb.1982.0158.

[24] V. A. Tucker and G. C. Parrot. Aerodynamics of gliding flight in a falcon and other birds. *Journal of Experimental Biology*, 52:345–367, 1970.

[25] C. D. Cone. *A mathematical analysis of the dynamic soaring flight of the albatross with ecological interpretations*. Virginia Institute of Marine Science, 1964.

[26] C. J. Wood. The flight of albatrosses (a computer simulation). *Ibis*, 115(2):244–256, 1973. doi: 10.1111/j.1474-919x.1973.tb02640.x.

[27] J. A. Wilson. Sweeping flight and soaring by albatrosses. *Nature*, 257(5524):307–308, 1975. doi: 10.1038/257307a0.

[28] G. P. Sachs. Optimal wind energy extraction for dynamic soaring. *Applied Mathematics in Aerospace Science and Engineering*, page 221–237, 1994. doi: 10.1007/978-1-4757-9259-1_10.

[29] Y. J. Zhao. Optimal patterns of glider dynamic soaring. *Optimal Control Applications and Methods*, 25(2):67–89, 2004. doi: 10.1002/oca.739.

[30] Y. J. Zhao and Y. C. Qi. Minimum fuel powered dynamic soaring of unmanned aerial vehicles utilizing wind gradients. *Optimal Control Applications and Methods*, 25(5):211–233, 2004. doi: 10.1002/oca.744.

[31] P. Lissaman. Wind energy extraction by birds and flight vehicles. *43rd AIAA Aerospace Sciences Meeting and Exhibit, Reno, USA*, 2005. doi: 10.2514/6.2005-241.

[32] G. P. Sachs, J. Lenz, and F. Holzapfel. Dynamic soaring of albatrosses over land. *AIAA Atmospheric Flight Mechanics (AFM) Conference*, 2013. doi: 10.2514/6.2013-4842.

[33] G. P. Sachs, J. Traugott, A. P. Nesterova, and F. Bonadonna. Experimental verification of dynamic soaring in albatrosses. *Journal of Experimental Biology*, 216(22):4222–4232, 2013. doi: 10.1242/jeb.085209.

[34] G. C. Bower. *Boundary Layer Dynamic Soaring for Autonomous Aircraft: Design and Validation*. PhD thesis, Stanford University, USA, 2012.

[35] V. Bonnin, C. Toomer, J.-M. Moschetta, and E. Benard. Energy harvesting mechanisms for UAV flight by dynamic soaring. *International Journal of Micro Air Vehicles*, 7(3):213–230, 2015. doi: 10.2514/6.2013-4841.

[36] G. P. Sachs and B. Grüter. Maximum travel speed performance of albatrosses and UAVs using dynamic soaring. *AIAA Scitech 2019 Forum, San Diego, USA*, Jan 2019. doi: 10.2514/6.2019-0568.

[37] G. P. Sachs. Kinetic energy in dynamic soaring - inertial speed and airspeed. *Journal of Guidance, and Dynamics*, 42(8):1812–1821, Jun 2019. doi: 10.2514/1.G003407.

[38] J.-M. Kai, T. Hamel, and C. Samson. Novel approach to dynamic soaring modeling and simulation. *Journal of Guidance, Control, and Dynamics*, 42(6):1250–1260, 2019. doi: 10.2514/1.g003866.

[39] I. Mir, A. Maqsood, H. E. Taha, and S. A. Eisa. Soaring energetics for a nature inspired unmanned aerial vehicle. *AIAA Scitech 2019 Forum, San Diego, USA*, Jun 2019. doi: 10.2514/6.2019-1622.

[40] N. Long, S. Watkins, J.-M. Moschetta, and V. Bonnin. Regenerative dynamic soaring trajectory augmentation over flat terrains. *AIAA Scitech 2019 Forum, San Diego, USA*, Jun 2019. doi: 10.2514/6.2019-0569.

[41] I. Mir, S. A. Eisa, and A. Maqsood. Review of dynamic soaring: technical aspects, nonlinear modeling perspectives and future directions. *Nonlinear Dynamics*, 94(4):3117–3144, 2018. doi: 10.1007/s11071-018-4540-3.

[42] M. Deittert, A. Richards, C. A. Toomer, and A. Pipe. Engineless unmanned aerial vehicle propulsion by dynamic soaring. *Journal of Guidance, Control, and Dynamics*, 32(5):1446–1457, 2009. doi: 10.2514/1.43270.

[43] A. C. Marta. Aircraft optimal design. MSc Course Notes, 2019, Insituto Superior Técnico, Lisboa, Portugal.

[44] S. Russel and P. Norvig. *Artificial Intelligence: A Modern Approach*. Pearson, 2018. ISBN:0136042597.

[45] X.-S. Yang. *Nature-inspired metaheuristic algorithms*. Luniver Press, 2010. ISBN:1905986106.

[46] M. Kelly. An introduction to trajectory optimization: How to do your own direct collocation. *SIAM Review*, 59(4):849–904, 2017. doi: 10.1137/16m1062569.

[47] D. Garg, M. Patterson, W. Hager, and A. Rao. An overview of three pseudospectral methods for the numerical solution of optimal control problems. 2017.

[48] Y. Nie, O. Faqir, and E. Kerrigan. ICLOCS2: A MATLAB toolbox for optimization based control. URL `http://www.ee.ic.ac.uk/ICLOCS/default.htm`. [Online. Accessed 5th October 2019].

[49] A. Wächter and L. T. Biegler. On the implementation of an interior-point filter line-search algorithm for large-scale nonlinear programming. *Mathematical Programming*, 106(1):25–57, 2005. doi: 10.1007/s10107-004-0559-y.

[50] B. Etkin and L. D. Reid. *Dynamics of flight: stability and control*. John Wiley and Sons, 1996. ISBN:0471034185.

Appendix A

List of UAVs

Table A.1 presents the list of UAVs considered to establish the relation between UAV weight and endurance time. All information was extracted from the manufacturers websites.

Name	Maker	Country	Type	Endurance [h]	Mass [Kg]
Phantom Eye	Phantom Works/Boeing	United States	HALE	96	4445
RQ-4 Global Hawk	Northrop Grumman	United States	HALE	32	14628
Hermes 900	Elbit Systems	Israel	MALE	36	1180
MQ-9 Reaper	General Atomics	United States	MALE	14	4760
Harfang	Airbus	France	MALE	24	1250
Hermes 450	Elbit Systems	Israel	TAUV	20	450
Aerostar	Aeronautics	Israel	TUAV	12	230
Falco	Leonardo	Italy	TUAV	13	490
AR5	Tekever	Portugal	TUAV	20	180
Hermes-90	Elbit Systems	Israel	SUAV	15	115
Scaneagle	Insitu	United States	SUAV	24	16
AR3	Tekever	Portugal	SUAV	10	22
Lipam M3	Argentine AF	Argentine	SUAV	5	60
MANTIS	Indra	Spain	MAUV	1,5	6,3
CREX-B	Leonardo	Italy	MAUV	1,2	2,1
AR4	Tekever	Portugal	MUAV	2	5
MASS MAV	Patria Aviation	Finland	MUAV	1,2	3,5
RQ-14 Dragon Eye	AeroViroment	United States	MUAV	1	2,7
Orbiter 2	Aeronautics	Israel	MUAV	3	10,3
PUMA3 AE	AeroViroment	United States	MUAV	2,5	6,8
Aliaca	Airbus	France	MUAV	3	12
Black Widow	AeroViroment	United States	μUAV	0,5	0,08
Mosquito I	IAI	Israel	μUAV	0,6	0,25

Table A.1: Complete list of UAVs considered for establishing the relationship between overall weight and endurance time.

Appendix B

Complete Deduction of Equations

B.1 Newton's Second Law in the Flight Path Frame

Starting from Newton's second law of motion in the Earth frame [50],

$$m\boldsymbol{a}^E = \sum \boldsymbol{F}^E \Leftrightarrow \tag{B.1a}$$

$$\Leftrightarrow m\dot{\boldsymbol{V_G}}^E = \sum \boldsymbol{F}^E \Leftrightarrow \tag{B.1b}$$

$$\Leftrightarrow m(\dot{\boldsymbol{V_A}}^E + \dot{\boldsymbol{W}}^E) = \sum \boldsymbol{F}^E \Leftrightarrow \tag{B.1c}$$

$$\Leftrightarrow m\frac{d}{dt}(\boldsymbol{T_{EF}}\boldsymbol{V_A}^F) + m\frac{d}{dt}(\boldsymbol{W}^E) = \boldsymbol{T_{EF}}\sum \boldsymbol{F}^F \Leftrightarrow \tag{B.1d}$$

$$\Leftrightarrow m(\dot{\boldsymbol{T_{EF}}}\boldsymbol{V_A}^F + \boldsymbol{T_{EF}}\dot{\boldsymbol{V_A}}^F) + m\dot{\boldsymbol{W}}^E = \boldsymbol{T_{EF}}\sum \boldsymbol{F}^F \Leftrightarrow \tag{B.1e}$$

$$\Leftrightarrow m(\tilde{\boldsymbol{\omega}}^E\boldsymbol{T_{EF}}\boldsymbol{V_A}^F + \boldsymbol{T_{EF}}\dot{\boldsymbol{V_A}}^F) + m\dot{\boldsymbol{W}}^E = \boldsymbol{T_{EF}}\sum \boldsymbol{F}^F \Leftrightarrow \tag{B.1f}$$

$$\Leftrightarrow m(\boldsymbol{T_{FE}}\tilde{\boldsymbol{\omega}}^E\boldsymbol{T_{EF}}\boldsymbol{V_A}^F + \boldsymbol{T_{FE}}\boldsymbol{T_{EF}}\dot{\boldsymbol{V_A}}^F) + \boldsymbol{T_{FE}}m\dot{\boldsymbol{W}}^E = \boldsymbol{T_{FE}}\boldsymbol{T_{EF}}\sum \boldsymbol{F}^F \Leftrightarrow \tag{B.1g}$$

$$\Leftrightarrow m(\dot{\boldsymbol{V_A}}^F + \tilde{\boldsymbol{\omega}}^F\boldsymbol{V_A}^F) + m\boldsymbol{T_{FE}}\dot{\boldsymbol{W}}^E = \sum \boldsymbol{F}^F \Leftrightarrow \tag{B.1h}$$

$$\Leftrightarrow m(\dot{\boldsymbol{V_A}}^F + \boldsymbol{\omega}^F \times \boldsymbol{V_A}^F) + m\dot{\boldsymbol{W}}^F = \sum \boldsymbol{F}^F, \tag{B.1i}$$

where $\boldsymbol{\omega}^F$ is the angular velocity vector of the flight path frame in respect to the earth frame and the terms $\tilde{\boldsymbol{\omega}}^E$ and $\tilde{\boldsymbol{\omega}}^F$ correspond, respectively, to the matrices of the angular velocities of the earth in respect to the flight path frame vice-versa, such that

$$\tilde{\boldsymbol{\omega}}^E = \begin{bmatrix} 0 & \dot{\psi} & -\dot{\gamma}\cos\psi \\ -\dot{\psi} & 0 & -\dot{\gamma}\sin\psi \\ \dot{\gamma}\cos\psi & \dot{\gamma}\sin\psi & 0 \end{bmatrix}, \tag{B.2}$$

$$\tilde{\boldsymbol{\omega}}^F = \begin{bmatrix} 0 & -\dot{\psi}\cos\gamma & \dot{\gamma} \\ \dot{\psi}\cos\gamma & 0 & \dot{\psi}\sin\gamma \\ -\dot{\gamma} & -\dot{\psi}\sin\gamma & 0, \end{bmatrix} \tag{B.3}$$

related through

$$\tilde{\boldsymbol{\omega}}^E = \boldsymbol{T_{EF}}\tilde{\boldsymbol{\omega}}^F\boldsymbol{T_{FE}}. \tag{B.4}$$

The vector ω^F is obtained from the definition of the cross product. Given two vectors $\boldsymbol{a} = (a_1, a_2, a_3)$ and $\boldsymbol{b} = (b_1, b_2, b_3)$, the cross product can be computed as

$$\boldsymbol{c} = \boldsymbol{a} \times \boldsymbol{b} = \tilde{\boldsymbol{a}}\boldsymbol{b}, \tag{B.5}$$

where,

$$\tilde{\boldsymbol{a}} = \begin{bmatrix} 0 & -a_3 & a_2 \\ a_3 & 0 & -a_1 \\ -a_2 & a_1 & 0, \end{bmatrix}. \tag{B.6}$$

So given $\tilde{\omega}^F$ the components of ω^F can be obtained.

B.2 Lift and Drag Contributions to Mechanical Energy Rate

Since the variation of mechanical energy is equal to the power of non-conservative forces, it is possible to write [35]

$$\frac{dE_m}{dt} = \sum(\boldsymbol{F_{NCF}}^E \cdot \boldsymbol{V_G}^E) = F_{NCF_x}V_x + F_{NCF_y}V_y + F_{NCF_z}V_z, \tag{B.7}$$

for the UAV model being considered, the only non-conservative forces are the lift and drag, meaning that

$$\frac{dE_m}{dt} = \boldsymbol{L}^E \cdot \boldsymbol{V_G}^E + \boldsymbol{D}^E \cdot \boldsymbol{V_G}^E, \tag{B.8}$$

which can be re-written using the air relative velocity vector,

$$\frac{dE_m}{dt} = \boldsymbol{L}^E \cdot (\boldsymbol{V_A}^E + \boldsymbol{W}^E) + \boldsymbol{D}^E \cdot (\boldsymbol{V_A}^E + \boldsymbol{W}^E). \tag{B.9}$$

This equation can be further simplified knowing that, by definition, the lift and the airspeed vector are always orthogonal and the drag and the airspeed vector are always opposed, resulting in

$$\frac{dE_m}{dt} = \boldsymbol{L}^E \cdot \boldsymbol{W}^E - DV_A + \boldsymbol{D}^E \cdot \boldsymbol{W}^E. \tag{B.10}$$

Finally since the wind has only component in the x direction of the Earth frame, it is only necessary to consider the component of the lift and drag on that direction, from equation 2.21,

$$\sum F_x^E = -D\cos\gamma\cos\psi - L(\cos\phi\sin\gamma\cos\psi + \sin\phi\sin\psi). \tag{B.11}$$

At the end, the final result is obtained,

$$\frac{dE_m}{dt} = -LW_x^E(\cos\phi\sin\gamma\cos\psi + \sin\phi\sin\psi) - DV_A - DW_x^E\cos\gamma\cos\psi. \tag{B.12}$$

Appendix C

Output Vector of Solution of Chapter 4

N	Time [s]	X [m]	Y[m]	Z[m]	V_A [m/s]	Ψ[rad]	γ[rad]	C_L[-]	φ[rad]
1	0	0	0	1,500	20	1,571	0	1,500	1,047
2	0,027	0,003	0,545	1,502	19,961	1,604	0,006	1,500	1,047
3	0,055	-0,012	1,089	1,506	19,920	1,637	0,011	1,500	1,047
4	0,082	-0,044	1,631	1,514	19,878	1,670	0,017	1,500	1,047
5	0,109	-0,095	2,169	1,525	19,835	1,704	0,023	1,500	1,047
6	0,137	-0,163	2,704	1,539	19,790	1,737	0,028	1,500	1,047
7	0,164	-0,248	3,234	1,555	19,745	1,770	0,034	1,500	1,047
8	0,191	-0,350	3,760	1,575	19,699	1,803	0,039	1,500	1,047
9	0,218	-0,470	4,280	1,597	19,652	1,836	0,044	1,500	1,047
10	0,246	-0,605	4,794	1,622	19,604	1,869	0,049	1,500	1,047
11	0,273	-0,757	5,302	1,650	19,556	1,902	0,054	1,500	1,047
12	0,300	-0,925	5,803	1,680	19,507	1,935	0,059	1,500	1,047
13	0,328	-1,108	6,295	1,713	19,457	1,968	0,064	1,500	1,047
14	0,355	-1,307	6,780	1,749	19,407	2,001	0,069	1,500	1,047
15	0,382	-1,520	7,256	1,786	19,356	2,034	0,074	1,500	1,047
16	0,410	-1,748	7,723	1,827	19,305	2,066	0,079	1,500	1,038
17	0,437	-1,990	8,181	1,870	19,253	2,099	0,084	1,500	1,018
18	0,464	-2,245	8,628	1,915	19,201	2,131	0,090	1,500	1,000
19	0,492	-2,513	9,066	1,964	19,149	2,162	0,096	1,500	0,983
20	0,519	-2,793	9,492	2,016	19,096	2,193	0,103	1,500	0,968
21	0,546	-3,085	9,908	2,071	19,042	2,224	0,110	1,500	0,954
22	0,573	-3,387	10,313	2,130	18,987	2,255	0,117	1,500	0,941
23	0,601	-3,701	10,706	2,192	18,932	2,285	0,124	1,500	0,929
24	0,628	-4,023	11,088	2,258	18,876	2,315	0,132	1,500	0,918
25	0,655	-4,356	11,458	2,328	18,820	2,345	0,140	1,500	0,908
26	0,683	-4,697	11,816	2,402	18,762	2,374	0,148	1,500	0,898
27	0,710	-5,046	12,162	2,479	18,704	2,403	0,156	1,500	0,889
28	0,737	-5,402	12,495	2,561	18,646	2,432	0,165	1,500	0,881
29	0,765	-5,766	12,816	2,646	18,587	2,461	0,173	1,500	0,873
30	0,792	-6,136	13,124	2,736	18,527	2,490	0,182	1,500	0,866
31	0,819	-6,512	13,420	2,829	18,466	2,518	0,190	1,500	0,859
32	0,847	-6,893	13,702	2,926	18,405	2,546	0,199	1,500	0,852
33	0,874	-7,280	13,972	3,028	18,343	2,574	0,208	1,500	0,846
34	0,901	-7,670	14,229	3,133	18,280	2,602	0,217	1,500	0,839
35	0,928	-8,065	14,473	3,242	18,216	2,629	0,225	1,499	0,833
36	0,956	-8,462	14,705	3,355	18,153	2,656	0,234	1,470	0,827
37	0,983	-8,863	14,923	3,472	18,089	2,683	0,242	1,437	0,820
38	1,010	-9,265	15,130	3,592	18,025	2,708	0,250	1,404	0,813
39	1,038	-9,669	15,324	3,715	17,962	2,733	0,257	1,372	0,806
40	1,065	-10,075	15,507	3,841	17,898	2,757	0,264	1,341	0,799
41	1,092	-10,481	15,678	3,970	17,835	2,780	0,270	1,311	0,792
42	1,120	-10,888	15,839	4,101	17,772	2,803	0,276	1,282	0,784
43	1,147	-11,295	15,989	4,234	17,709	2,825	0,281	1,253	0,776
44	1,174	-11,702	16,128	4,369	17,646	2,846	0,286	1,226	0,767
45	1,202	-12,108	16,258	4,506	17,583	2,866	0,290	1,200	0,758
46	1,229	-12,514	16,379	4,644	17,521	2,886	0,295	1,175	0,749
47	1,256	-12,918	16,490	4,783	17,458	2,905	0,298	1,152	0,739
48	1,283	-13,321	16,593	4,924	17,396	2,923	0,302	1,130	0,730
49	1,311	-13,723	16,687	5,066	17,333	2,941	0,305	1,108	0,720
50	1,338	-14,124	16,773	5,208	17,271	2,958	0,308	1,089	0,709
51	1,365	-14,522	16,851	5,352	17,208	2,975	0,311	1,070	0,699
52	1,393	-14,919	16,921	5,496	17,146	2,991	0,313	1,053	0,688
53	1,420	-15,313	16,985	5,640	17,084	3,007	0,315	1,036	0,677
54	1,447	-15,706	17,041	5,785	17,022	3,022	0,317	1,021	0,666
55	1,475	-16,096	17,091	5,930	16,959	3,036	0,318	1,007	0,655
56	1,502	-16,484	17,134	6,075	16,897	3,050	0,320	0,994	0,644
57	1,529	-16,869	17,171	6,220	16,835	3,064	0,321	0,983	0,633
58	1,557	-17,252	17,202	6,365	16,773	3,077	0,322	0,972	0,622
59	1,584	-17,632	17,227	6,510	16,711	3,090	0,323	0,962	0,611
60	1,611	-18,010	17,246	6,654	16,649	3,102	0,324	0,954	0,600
61	1,638	-18,385	17,261	6,799	16,586	3,114	0,324	0,946	0,590
62	1,666	-18,757	17,270	6,943	16,524	3,126	0,325	0,939	0,579
63	1,693	-19,127	17,274	7,087	16,462	3,137	0,325	0,933	0,569
64	1,720	-19,494	17,274	7,231	16,400	3,148	0,326	0,928	0,559
65	1,748	-19,857	17,268	7,374	16,338	3,159	0,326	0,924	0,550
66	1,775	-20,218	17,259	7,516	16,276	3,170	0,326	0,921	0,540
67	1,802	-20,577	17,245	7,658	16,214	3,180	0,326	0,918	0,531
68	1,830	-20,932	17,227	7,799	16,152	3,190	0,326	0,917	0,523
69	1,857	-21,284	17,205	7,940	16,089	3,200	0,325	0,916	0,514
70	1,884	-21,633	17,179	8,080	16,027	3,209	0,325	0,915	0,507
71	1,912	-21,980	17,149	8,220	15,965	3,219	0,325	0,916	0,499

N	Time [s]	X [m]	Y[m]	Z[m]	V_A [m/s]	Ψ[rad]	γ[rad]	C_L[-]	φ[rad]
72	1,939	-22,323	17,115	8,359	15,903	3,228	0,325	0,917	0,492
73	1,966	-22,664	17,078	8,497	15,841	3,237	0,324	0,918	0,485
74	1,993	-23,001	17,037	8,634	15,778	3,245	0,324	0,921	0,479
75	2,021	-23,335	16,993	8,771	15,716	3,254	0,323	0,924	0,474
76	2,048	-23,667	16,946	8,907	15,654	3,263	0,323	0,927	0,468
77	2,075	-23,995	16,896	9,042	15,591	3,271	0,322	0,932	0,463
78	2,103	-24,320	16,842	9,177	15,529	3,280	0,322	0,937	0,459
79	2,130	-24,642	16,785	9,311	15,467	3,288	0,321	0,942	0,455
80	2,157	-24,961	16,725	9,444	15,404	3,296	0,321	0,948	0,451
81	2,185	-25,277	16,662	9,576	15,341	3,304	0,320	0,955	0,448
82	2,212	-25,589	16,596	9,708	15,279	3,312	0,320	0,963	0,445
83	2,239	-25,899	16,528	9,839	15,216	3,320	0,320	0,971	0,443
84	2,267	-26,205	16,456	9,969	15,153	3,328	0,319	0,979	0,441
85	2,294	-26,508	16,382	10,098	15,090	3,337	0,319	0,989	0,440
86	2,321	-26,808	16,304	10,227	15,027	3,345	0,318	0,999	0,439
87	2,348	-27,105	16,225	10,355	14,964	3,353	0,318	1,010	0,438
88	2,376	-27,398	16,142	10,483	14,900	3,361	0,318	1,022	0,438
89	2,403	-27,688	16,057	10,609	14,837	3,369	0,318	1,034	0,438
90	2,430	-27,975	15,968	10,736	14,773	3,377	0,318	1,048	0,438
91	2,458	-28,259	15,878	10,861	14,709	3,385	0,318	1,062	0,439
92	2,485	-28,539	15,784	10,986	14,645	3,394	0,318	1,077	0,440
93	2,512	-28,815	15,688	11,111	14,580	3,402	0,318	1,094	0,442
94	2,540	-29,088	15,589	11,235	14,515	3,411	0,318	1,111	0,444
95	2,567	-29,358	15,488	11,359	14,450	3,419	0,318	1,130	0,446
96	2,594	-29,624	15,384	11,482	14,384	3,428	0,319	1,149	0,448
97	2,622	-29,886	15,277	11,605	14,318	3,437	0,320	1,170	0,451
98	2,649	-30,145	15,168	11,728	14,252	3,446	0,320	1,193	0,454
99	2,676	-30,399	15,056	11,850	14,185	3,456	0,321	1,217	0,457
100	2,703	-30,650	14,941	11,973	14,117	3,465	0,323	1,242	0,460
101	2,731	-30,897	14,823	12,095	14,049	3,475	0,324	1,269	0,464
102	2,758	-31,140	14,703	12,217	13,979	3,485	0,326	1,298	0,468
103	2,785	-31,379	14,580	12,339	13,910	3,495	0,328	1,329	0,472
104	2,813	-31,614	14,454	12,462	13,839	3,506	0,330	1,362	0,476
105	2,840	-31,844	14,325	12,584	13,767	3,517	0,332	1,398	0,480
106	2,867	-32,070	14,193	12,707	13,695	3,528	0,335	1,435	0,485
107	2,895	-32,291	14,059	12,830	13,621	3,539	0,338	1,476	0,490
108	2,922	-32,507	13,922	12,954	13,546	3,551	0,342	1,500	0,495
109	2,949	-32,719	13,781	13,078	13,470	3,563	0,345	1,500	0,499
110	2,976	-32,926	13,638	13,203	13,393	3,575	0,348	1,500	0,504
111	3,004	-33,128	13,493	13,327	13,316	3,587	0,351	1,500	0,509
112	3,031	-33,325	13,344	13,452	13,238	3,599	0,353	1,500	0,514
113	3,058	-33,517	13,193	13,577	13,160	3,611	0,355	1,500	0,519
114	3,086	-33,704	13,039	13,702	13,081	3,623	0,357	1,500	0,524
115	3,113	-33,887	12,883	13,827	13,001	3,635	0,358	1,500	0,529
116	3,140	-34,064	12,724	13,951	12,921	3,647	0,360	1,500	0,534
117	3,168	-34,237	12,563	14,075	12,841	3,659	0,360	1,500	0,538
118	3,195	-34,405	12,400	14,198	12,761	3,671	0,361	1,500	0,543
119	3,222	-34,568	12,234	14,321	12,680	3,683	0,361	1,500	0,548
120	3,250	-34,726	12,066	14,443	12,599	3,695	0,361	1,500	0,552
121	3,277	-34,880	11,896	14,564	12,518	3,707	0,361	1,500	0,557
122	3,304	-35,029	11,723	14,684	12,436	3,719	0,360	1,500	0,562
123	3,331	-35,173	11,549	14,804	12,355	3,731	0,359	1,500	0,566
124	3,359	-35,313	11,373	14,922	12,273	3,743	0,358	1,500	0,570
125	3,386	-35,448	11,194	15,038	12,192	3,754	0,356	1,500	0,575
126	3,413	-35,578	11,014	15,154	12,111	3,766	0,354	1,500	0,579
127	3,441	-35,704	10,831	15,268	12,030	3,778	0,352	1,500	0,583
128	3,468	-35,825	10,647	15,381	11,949	3,790	0,350	1,500	0,588
129	3,495	-35,941	10,461	15,491	11,869	3,802	0,347	1,500	0,592
130	3,523	-36,054	10,273	15,601	11,789	3,813	0,344	1,500	0,596
131	3,550	-36,162	10,084	15,708	11,709	3,825	0,340	1,500	0,600
132	3,577	-36,265	9,893	15,814	11,630	3,836	0,336	1,500	0,604
133	3,605	-36,364	9,700	15,918	11,552	3,848	0,332	1,500	0,608
134	3,632	-36,459	9,506	16,019	11,474	3,860	0,327	1,500	0,612
135	3,659	-36,550	9,310	16,119	11,397	3,871	0,322	1,500	0,615
136	3,686	-36,636	9,112	16,217	11,321	3,883	0,317	1,500	0,619
137	3,714	-36,719	8,913	16,312	11,245	3,894	0,312	1,500	0,623
138	3,741	-36,797	8,713	16,405	11,171	3,906	0,306	1,500	0,627
139	3,768	-36,871	8,511	16,495	11,098	3,917	0,300	1,500	0,630
140	3,796	-36,942	8,307	16,584	11,026	3,928	0,293	1,500	0,634
141	3,823	-37,008	8,103	16,669	10,955	3,940	0,286	1,500	0,638
142	3,850	-37,070	7,897	16,753	10,885	3,951	0,279	1,500	0,641

N	Time [s]	X [m]	Y[m]	Z[m]	V_A [m/s]	Ψ[rad]	γ[rad]	C_L[-]	φ[rad]
143	3,878	-37,129	7,689	16,833	10,817	3,962	0,271	1,500	0,645
144	3,905	-37,184	7,480	16,911	10,750	3,974	0,264	1,500	0,649
145	3,932	-37,235	7,270	16,986	10,684	3,985	0,255	1,500	0,652
146	3,960	-37,282	7,059	17,058	10,621	3,996	0,247	1,500	0,656
147	3,987	-37,326	6,846	17,128	10,559	4,007	0,238	1,500	0,660
148	4,014	-37,366	6,632	17,194	10,498	4,019	0,229	1,500	0,663
149	4,041	-37,402	6,417	17,258	10,440	4,030	0,220	1,500	0,667
150	4,069	-37,435	6,200	17,319	10,383	4,041	0,210	1,500	0,671
151	4,096	-37,465	5,982	17,376	10,329	4,053	0,200	1,500	0,675
152	4,123	-37,491	5,763	17,431	10,276	4,064	0,190	1,500	0,678
153	4,151	-37,513	5,543	17,482	10,226	4,075	0,179	1,500	0,682
154	4,178	-37,533	5,322	17,530	10,178	4,087	0,168	1,500	0,686
155	4,205	-37,548	5,099	17,575	10,132	4,098	0,157	1,500	0,690
156	4,233	-37,561	4,875	17,617	10,089	4,110	0,146	1,500	0,694
157	4,260	-37,570	4,650	17,655	10,048	4,121	0,134	1,500	0,699
158	4,287	-37,576	4,423	17,690	10,010	4,133	0,122	1,500	0,703
159	4,315	-37,579	4,196	17,722	9,974	4,145	0,110	1,500	0,707
160	4,342	-37,578	3,967	17,750	9,941	4,156	0,098	1,500	0,711
161	4,369	-37,574	3,737	17,775	9,911	4,168	0,085	1,500	0,716
162	4,396	-37,567	3,505	17,796	9,884	4,180	0,073	1,500	0,721
163	4,424	-37,557	3,273	17,814	9,859	4,192	0,060	1,500	0,725
164	4,451	-37,544	3,039	17,828	9,838	4,205	0,047	1,500	0,730
165	4,478	-37,527	2,804	17,839	9,819	4,217	0,034	1,500	0,735
166	4,506	-37,508	2,567	17,846	9,804	4,229	0,020	1,500	0,740
167	4,533	-37,485	2,330	17,850	9,791	4,242	0,007	1,500	0,745
168	4,560	-37,459	2,091	17,850	9,782	4,255	-0,007	1,500	0,751
169	4,588	-37,430	1,851	17,846	9,776	4,268	-0,021	1,500	0,756
170	4,615	-37,397	1,609	17,839	9,773	4,281	-0,034	1,500	0,761
171	4,642	-37,362	1,366	17,828	9,774	4,294	-0,048	1,500	0,767
172	4,670	-37,323	1,122	17,813	9,777	4,308	-0,062	1,500	0,773
173	4,697	-37,281	0,876	17,795	9,784	4,321	-0,076	1,500	0,779
174	4,724	-37,236	0,629	17,773	9,795	4,335	-0,090	1,500	0,785
175	4,751	-37,187	0,381	17,747	9,809	4,349	-0,104	1,500	0,791
176	4,779	-37,135	0,131	17,717	9,826	4,364	-0,118	1,500	0,797
177	4,806	-37,080	-0,120	17,683	9,847	4,378	-0,132	1,500	0,803
178	4,833	-37,022	-0,373	17,646	9,871	4,393	-0,146	1,500	0,809
179	4,861	-36,960	-0,627	17,605	9,898	4,408	-0,160	1,500	0,816
180	4,888	-36,894	-0,882	17,560	9,929	4,424	-0,173	1,500	0,822
181	4,915	-36,825	-1,139	17,512	9,964	4,440	-0,187	1,500	0,829
182	4,943	-36,753	-1,397	17,459	10,002	4,456	-0,200	1,500	0,835
183	4,970	-36,676	-1,656	17,403	10,043	4,472	-0,214	1,500	0,842
184	4,997	-36,596	-1,917	17,343	10,088	4,488	-0,227	1,500	0,848
185	5,025	-36,513	-2,180	17,279	10,136	4,505	-0,240	1,500	0,855
186	5,052	-36,425	-2,444	17,211	10,187	4,523	-0,253	1,500	0,862
187	5,079	-36,333	-2,709	17,140	10,242	4,540	-0,266	1,500	0,868
188	5,106	-36,238	-2,975	17,064	10,300	4,558	-0,278	1,500	0,875
189	5,134	-36,138	-3,243	16,985	10,362	4,576	-0,291	1,500	0,881
190	5,161	-36,034	-3,512	16,902	10,427	4,595	-0,303	1,500	0,888
191	5,188	-35,926	-3,783	16,815	10,495	4,614	-0,315	1,500	0,894
192	5,216	-35,814	-4,055	16,725	10,566	4,633	-0,326	1,500	0,900
193	5,243	-35,696	-4,328	16,630	10,641	4,653	-0,338	1,500	0,906
194	5,270	-35,575	-4,602	16,532	10,719	4,673	-0,349	1,500	0,912
195	5,298	-35,448	-4,878	16,430	10,799	4,694	-0,359	1,500	0,918
196	5,325	-35,317	-5,154	16,325	10,883	4,714	-0,370	1,500	0,924
197	5,352	-35,181	-5,432	16,216	10,970	4,736	-0,380	1,500	0,930
198	5,380	-35,040	-5,710	16,103	11,060	4,757	-0,390	1,500	0,935
199	5,407	-34,893	-5,990	15,986	11,153	4,779	-0,400	1,500	0,940
200	5,434	-34,741	-6,270	15,866	11,249	4,802	-0,409	1,500	0,945
201	5,461	-34,584	-6,551	15,742	11,348	4,824	-0,418	1,500	0,950
202	5,489	-34,421	-6,833	15,614	11,449	4,848	-0,426	1,500	0,955
203	5,516	-34,253	-7,115	15,483	11,553	4,871	-0,435	1,500	0,959
204	5,543	-34,078	-7,398	15,348	11,660	4,895	-0,443	1,500	0,963
205	5,571	-33,898	-7,681	15,210	11,770	4,919	-0,450	1,500	0,967
206	5,598	-33,711	-7,964	15,069	11,882	4,944	-0,457	1,500	0,971
207	5,625	-33,518	-8,248	14,924	11,996	4,969	-0,464	1,500	0,975
208	5,653	-33,319	-8,531	14,776	12,114	4,995	-0,471	1,500	0,978
209	5,680	-33,113	-8,814	14,624	12,233	5,020	-0,477	1,500	0,981
210	5,707	-32,900	-9,097	14,469	12,355	5,047	-0,482	1,500	0,984
211	5,734	-32,680	-9,379	14,311	12,479	5,073	-0,488	1,500	0,987
212	5,762	-32,454	-9,660	14,150	12,606	5,100	-0,493	1,500	0,989
213	5,789	-32,220	-9,940	13,985	12,734	5,127	-0,497	1,500	0,992

N	Time [s]	X [m]	Y[m]	Z[m]	V_A [m/s]	Ψ[rad]	γ[rad]	C_L[-]	φ[rad]
214	5,816	-31,979	-10,219	13,818	12,865	5,155	-0,501	1,500	0,994
215	5,844	-31,731	-10,497	13,648	12,997	5,182	-0,505	1,500	0,996
216	5,871	-31,475	-10,773	13,475	13,132	5,211	-0,509	1,500	0,998
217	5,898	-31,212	-11,047	13,299	13,268	5,239	-0,512	1,500	1,000
218	5,926	-30,941	-11,319	13,120	13,407	5,268	-0,514	1,500	1,001
219	5,953	-30,662	-11,589	12,938	13,546	5,297	-0,517	1,500	1,003
220	5,980	-30,375	-11,855	12,754	13,688	5,326	-0,519	1,500	1,004
221	6,008	-30,080	-12,119	12,568	13,831	5,355	-0,520	1,500	1,005
222	6,035	-29,777	-12,380	12,379	13,975	5,385	-0,521	1,500	1,006
223	6,062	-29,466	-12,637	12,188	14,121	5,415	-0,522	1,500	1,007
224	6,089	-29,147	-12,890	11,995	14,268	5,445	-0,523	1,500	1,008
225	6,117	-28,819	-13,139	11,799	14,416	5,475	-0,523	1,500	1,009
226	6,144	-28,483	-13,383	11,601	14,566	5,506	-0,523	1,500	1,010
227	6,171	-28,138	-13,622	11,402	14,716	5,536	-0,522	1,500	1,010
228	6,199	-27,786	-13,856	11,201	14,867	5,567	-0,521	1,500	1,011
229	6,226	-27,424	-14,084	10,998	15,019	5,598	-0,520	1,500	1,011
230	6,253	-27,055	-14,306	10,793	15,171	5,629	-0,518	1,500	1,011
231	6,281	-26,677	-14,522	10,587	15,324	5,661	-0,517	1,500	1,011
232	6,308	-26,291	-14,730	10,380	15,477	5,692	-0,514	1,500	1,011
233	6,335	-25,897	-14,932	10,172	15,631	5,724	-0,512	1,500	1,011
234	6,363	-25,494	-15,125	9,962	15,785	5,755	-0,509	1,500	1,010
235	6,390	-25,084	-15,311	9,752	15,938	5,787	-0,506	1,500	1,010
236	6,417	-24,666	-15,488	9,540	16,092	5,819	-0,503	1,500	1,009
237	6,444	-24,240	-15,655	9,328	16,245	5,851	-0,499	1,500	1,008
238	6,472	-23,806	-15,814	9,116	16,398	5,883	-0,495	1,500	1,006
239	6,499	-23,365	-15,963	8,903	16,550	5,915	-0,491	1,500	1,005
240	6,526	-22,917	-16,101	8,690	16,702	5,947	-0,486	1,500	1,003
241	6,554	-22,463	-16,229	8,477	16,853	5,978	-0,481	1,500	1,000
242	6,581	-22,001	-16,346	8,265	17,002	6,010	-0,476	1,500	0,998
243	6,608	-21,533	-16,451	8,052	17,151	6,042	-0,470	1,500	0,995
244	6,636	-21,059	-16,545	7,840	17,298	6,074	-0,465	1,500	0,992
245	6,663	-20,579	-16,626	7,629	17,443	6,106	-0,459	1,500	0,989
246	6,690	-20,094	-16,695	7,418	17,587	6,138	-0,452	1,500	0,986
247	6,718	-19,603	-16,751	7,209	17,729	6,170	-0,446	1,500	0,982
248	6,745	-19,108	-16,793	7,001	17,869	6,202	-0,439	1,500	0,978
249	6,772	-18,609	-16,822	6,795	18,006	6,234	-0,432	1,500	0,974
250	6,799	-18,105	-16,838	6,590	18,142	6,265	-0,424	1,500	0,970
251	6,827	-17,599	-16,839	6,387	18,274	6,297	-0,416	1,500	0,966
252	6,854	-17,089	-16,825	6,186	18,404	6,328	-0,408	1,500	0,962
253	6,881	-16,577	-16,797	5,988	18,530	6,359	-0,400	1,500	0,958
254	6,909	-16,062	-16,754	5,792	18,654	6,391	-0,392	1,500	0,954
255	6,936	-15,546	-16,696	5,599	18,774	6,422	-0,383	1,500	0,949
256	6,963	-15,029	-16,622	5,409	18,891	6,453	-0,374	1,500	0,945
257	6,991	-14,512	-16,534	5,222	19,004	6,484	-0,365	1,500	0,941
258	7,018	-13,994	-16,429	5,039	19,113	6,515	-0,355	1,500	0,938
259	7,045	-13,477	-16,309	4,859	19,218	6,546	-0,346	1,500	0,934
260	7,073	-12,961	-16,173	4,684	19,320	6,576	-0,336	1,500	0,931
261	7,100	-12,447	-16,021	4,512	19,417	6,607	-0,326	1,500	0,928
262	7,127	-11,936	-15,853	4,344	19,509	6,638	-0,316	1,500	0,925
263	7,154	-11,427	-15,669	4,181	19,597	6,668	-0,306	1,500	0,923
264	7,182	-10,922	-15,470	4,022	19,681	6,699	-0,295	1,500	0,921
265	7,209	-10,421	-15,255	3,868	19,760	6,729	-0,285	1,500	0,920
266	7,236	-9,925	-15,023	3,719	19,834	6,759	-0,274	1,500	0,919
267	7,264	-9,434	-14,777	3,575	19,904	6,790	-0,263	1,500	0,919
268	7,291	-8,949	-14,514	3,436	19,968	6,820	-0,253	1,500	0,919
269	7,318	-8,471	-14,237	3,302	20,028	6,851	-0,242	1,500	0,919
270	7,346	-8,000	-13,944	3,174	20,083	6,881	-0,231	1,500	0,921
271	7,373	-7,537	-13,636	3,051	20,133	6,911	-0,221	1,500	0,923
272	7,400	-7,082	-13,313	2,933	20,179	6,942	-0,210	1,500	0,926
273	7,428	-6,637	-12,976	2,821	20,219	6,973	-0,200	1,500	0,929
274	7,455	-6,201	-12,625	2,714	20,255	7,003	-0,189	1,500	0,934
275	7,482	-5,776	-12,260	2,613	20,286	7,034	-0,179	1,500	0,939
276	7,509	-5,362	-11,881	2,517	20,313	7,065	-0,169	1,500	0,945
277	7,537	-4,960	-11,489	2,427	20,335	7,096	-0,159	1,500	0,952
278	7,564	-4,569	-11,085	2,341	20,353	7,128	-0,149	1,500	0,961
279	7,591	-4,192	-10,668	2,261	20,367	7,159	-0,140	1,500	0,970
280	7,619	-3,827	-10,239	2,186	20,377	7,191	-0,131	1,500	0,981
281	7,646	-3,477	-9,799	2,116	20,384	7,223	-0,122	1,500	0,992
282	7,673	-3,142	-9,347	2,050	20,386	7,255	-0,114	1,500	1,006
283	7,701	-2,821	-8,885	1,989	20,385	7,288	-0,107	1,500	1,021
284	7,728	-2,516	-8,413	1,931	20,382	7,321	-0,099	1,500	1,037

N	Time [s]	X [m]	Y[m]	Z[m]	V_A [m/s]	Ψ[rad]	γ[rad]	C_L[-]	φ[rad]
285	7,755	-2,227	-7,931	1,878	20,375	7,354	-0,093	1,500	1,047
286	7,783	-1,954	-7,441	1,828	20,366	7,388	-0,086	1,500	1,047
287	7,810	-1,699	-6,942	1,782	20,354	7,421	-0,080	1,500	1,047
288	7,837	-1,461	-6,435	1,740	20,339	7,454	-0,073	1,500	1,047
289	7,864	-1,240	-5,922	1,701	20,322	7,488	-0,067	1,500	1,047
290	7,892	-1,036	-5,402	1,665	20,303	7,521	-0,061	1,500	1,047
291	7,919	-0,851	-4,876	1,633	20,281	7,554	-0,054	1,500	1,047
292	7,946	-0,683	-4,345	1,605	20,258	7,588	-0,048	1,500	1,047
293	7,974	-0,534	-3,810	1,580	20,232	7,621	-0,042	1,500	1,047
294	8,001	-0,403	-3,271	1,559	20,204	7,654	-0,036	1,500	1,047
295	8,028	-0,290	-2,730	1,541	20,174	7,688	-0,030	1,500	1,047
296	8,056	-0,195	-2,186	1,526	20,143	7,721	-0,024	1,500	1,047
297	8,083	-0,119	-1,640	1,514	20,110	7,754	-0,018	1,500	1,047
298	8,110	-0,061	-1,093	1,506	20,075	7,788	-0,012	1,500	1,047
299	8,137	-0,021	-0,547	1,502	20,038	7,821	-0,006	1,500	1,047
300	8,165	0	0	1,500	20	7,854	0	1,500	1,047